

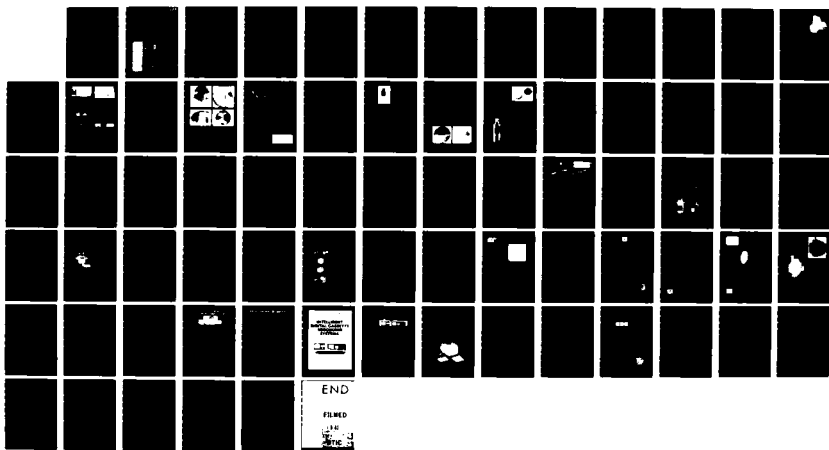
AD-A126 758

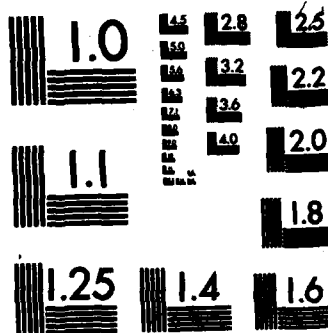
AN EXPERIMENTAL DEVICE FOR REAL TIME DETERMINATION OF
SLANT PATH ATMOSPHE. (U) SCRIPPS INSTITUTION OF
OCEANOGRAPHY LA JOLLA CA VISIBILITY LA. R W JOHNSON
MAR 82 SIO-REF-82-27 AFGL-TR-82-0125 . F/G 14/2

1/1

UNCLASSIFIED

NL





MICROCOPY RESOLUTION TEST CHART
NATIONAL BUREAU OF STANDARDS-1963-A

15

AFGL-TR-82-0125

SIO Ref. 82-27

AD A 126758

AN EXPERIMENTAL DEVICE FOR REAL TIME DETERMINATION OF SLANT PATH ATMOSPHERIC CONTRAST TRANSMITTANCE

Richard W. Johnson

Approved for public release; distribution unlimited.

Scientific Report No. 1
March 1982

Contract No. F19628-81-K-0023
Project No. ILIR
Task No. ILIR-1B
Work Unit No. ILIR-1BAA

Contract Monitor, Major John D. Mill, USAF
Optical Physics Division

Prepared for
Air Force Geophysics Laboratory, Air Force Systems Command

This research was supported by the Air Force In-House
Laboratory Independent Research Fund
United States Air Force, Hanscom AFB, Massachusetts 01731

DTIC
ELECTE
APR 12 1983
S D D

UNIVERSITY
OF
CALIFORNIA
SAN DIEGO



SCRIPPS
INSTITUTION
OF
OCEANOGRAPHY

DTIC FILE COPY

VISIBILITY LABORATORY La Jolla, California 92093

83 04 11 066

**Qualified requestors may obtain additional copies from the
Defense Technical Information Center. All others should apply
to the National Technical Information Service.**

UNCLASSIFIED

SECURITY CLASSIFICATION OF THIS PAGE (When Data Entered)

REPORT DOCUMENTATION PAGE		READ INSTRUCTIONS BEFORE COMPLETING FORM
1. REPORT NUMBER AFGL-TR-82-0125	2. GOVT ACCESSION NO. AD-A126 758	3. RECIPIENT'S CATALOG NUMBER
4. TITLE (and Subtitle) AN EXPERIMENTAL DEVICE FOR REAL TIME DETERMINATION OF SLANT PATH ATMOSPHERIC CONTRAST TRANSMITTANCE		5. TYPE OF REPORT & PERIOD COVERED Scientific Report No. 1
7. AUTHOR(s) Richard W. Johnson		6. PERFORMING ORG. REPORT NUMBER SIO Ref. 82-27
9. PERFORMING ORGANIZATION NAME AND ADDRESS University of California, San Diego Visibility Laboratory La Jolla, California 92093		8. CONTRACT OR GRANT NUMBER(s) F19628-81-K-0023
11. CONTROLLING OFFICE NAME AND ADDRESS Air Force Geophysics Laboratory Hanscom AFB, Massachusetts 01731 Contract Monitor: Major John D. Mill/OPA		10. PROGRAM ELEMENT, PROJECT, TASK AREA & WORK UNIT NUMBERS 61101F ILIR-1BAA
14. MONITORING AGENCY NAME & ADDRESS (if different from Controlling Office)		12. REPORT DATE March 1982
		13. NUMBER OF PAGES 71
		15. SECURITY CLASS. (of this report) UNCLASSIFIED
		15a. DECLASSIFICATION/DOWNGRADING SCHEDULE
16. DISTRIBUTION STATEMENT (of this Report) Approved for public release; distribution unlimited.		
17. DISTRIBUTION STATEMENT (of the abstract entered in Block 20, if different from Report)		
18. SUPPLEMENTARY NOTES		
19. KEY WORDS (Continue on reverse side if necessary and identify by block number) Visible Image Transmission Multi-channel Nephelometer Atmospheric Optical Properties Sky and Terrain Radiances Tropospheric Contrast Transmittance		
20. ABSTRACT (Continue on reverse side if necessary and identify by block number) A simple, yet relatively smart electro-optical system has been devised to do real-time monitoring of the optical state of the atmosphere. The system concept has been built around three solid state, no moving parts, transducer assemblies interfaced with a small dedicated microprocessor that can control the system in either a semi-automatic, or an operator interactive mode.		

DD FORM 1 JAN 73 1473

EDITION OF 1 NOV 65 IS OBSOLETE
S/N 0102-014-6601

UNCLASSIFIED

SECURITY CLASSIFICATION OF THIS PAGE (When Data Entered)

UNCLASSIFIED

SECURITY CLASSIFICATION OF THIS PAGE (When Data Entered)

20. ABSTRACT continued:

The development status is such that each of the system sub-assemblies has been evaluated in an operational mock-up configuration, and has performed adequately to indicate technical feasibility.

A new compact, multi-channel nephelometer has been developed which retains many of the features of the larger C-130 mounted version reported by Johnson (1981), but which requires only a few hundred watts of input power, and is less than one meter in length overall. The nephelometer mock-up, operating in pulsed mode has measured the scattering characteristics of clear day room air, with adequate sensitivity to suggest the capability of measurements approaching $10^{-5} m^{-1}$ i.e. sea level molecular.

A staring fisheye scanner using solid state detection has also performed well in its mock-up configuration. The sky and sun zone average radiances as measured under several different meteorological conditions are well placed on the system's flux-voltage curve. Thus, the use of this discrete detector system should proceed to full brass board configuration with little difficulty. As discussed in sections four and five however, the influence of the direct solar component upon equilibrium radiance is strong under clear or light haze conditions, and thus continuing analytic studies are recommended to optimize the selection of the sun zone diffuser pattern.

The in-flight computer system requirements have been evaluated and circuit mock-ups are in progress. Sub-assembly selections have been made based upon the demonstrated transducer performances in concert with the computational requirements which are illustrated. The pulse integration and multiplexing circuitry has been used in the evaluation of the nephelometer performance, and found to be satisfactory. Breadboarding of these circuits is underway with the immediate goal of adequate completion to illustrate full system mock-up performances.

Accession For	
NTIS GRA&I	<input checked="" type="checkbox"/>
DTIC TAB	<input type="checkbox"/>
Unannounced	<input type="checkbox"/>
Justification	
By	
Distribution/	
Availability Codes	
Dist	Avail and/or Special
A	

DTIC
COPY
HARDWARE
2

UNCLASSIFIED


SECURITY CLASSIFICATION OF THIS PAGE (When Data Entered)

**AN EXPERIMENTAL DEVICE FOR REAL TIME DETERMINATION
OF SLANT PATH ATMOSPHERIC CONTRAST TRANSMITTANCE**

Richard W. Johnson

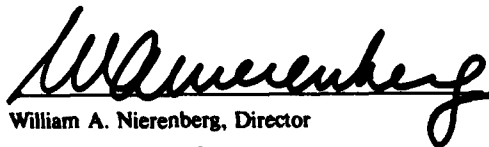
Visibility Laboratory
University of California, San Diego
Scripps Institution of Oceanography
La Jolla, California 92093

Approved:



Roswell W. Austin, Director
Visibility Laboratory

Approved:



William A. Nierenberg, Director
Scripps Institution of Oceanography

CONTRACT NO. F19628-81-K-0023

Project No. ILIR

Task No. ILIR-1B

Work Unit No. ILIR-1BAA

Scientific Report No. 1

March 1982

Contract Monitor

Major John D. Mill, Atmospheric Optics Branch, Optical Physics Division

This research was supported by the Air Force In-House
Laboratory Independent Research Fund.

Approved for public release; distribution unlimited.

Prepared for

**AIR FORCE GEOPHYSICS LABORATORY
AIR FORCE SYSTEMS COMMAND
UNITED STATES AIR FORCE
HANSCOM AFB, MASSACHUSETTS 01731**

SUMMARY

A simple, yet relatively smart electro-optical system has been devised to do real-time monitoring of the optical state of the atmosphere. The system concept has been built around three solid state, no moving parts, transducer assemblies interfaced with a small dedicated microprocessor that can control the system in either a semi-automatic, or an operator interactive mode.

The development status is such that each of the system sub-assemblies has been evaluated in an operational mock-up configuration, and has performed adequately, indicating technical feasibility of the overall design concept.

A new compact, multi-channel nephelometer has been developed which retains many of the features of the larger C-130 mounted version reported by Johnson (1981a), but which requires only a few hundred watts of input power, and is less than one meter in length overall. The nephelometer mock-up, operating in pulsed mode, has measured the scattering characteristics of clear day room air, with adequate sensitivity to suggest the capability of measurements approaching $10^{-5}m^{-1}$ i.e. sea level molecular.

A staring fisheye scanner using solid state detection has also performed well in its mock-up configuration. The sky and sun zone average radiances as measured under several different meteorological conditions are well placed on the system's flux-voltage curve. Thus, the use of this discrete detector system should proceed to full brass board configuration with little difficulty. As discussed in sections four and five however, the influence of the direct solar component upon equilibrium radiance is strong under clear or light haze conditions, and thus continuing analytic studies are recommended to optimize the selection of the sun zone diffuser pattern.

The in-flight computer system requirements have been evaluated and circuit mock-ups are in progress. Sub-assembly selections have been made based upon the demonstrated transducer performances in concert with the computational requirements which are illustrated. The pulse integration and multiplexing circuitry has been used in the evaluation of the nephelometer performance, and found to be satisfactory. Breadboarding of these circuits is underway with the immediate goal of demonstrating full system mock-up performances.

TABLE OF CONTENTS

SUMMARY	v
LIST OF ILLUSTRATIONS	ix
1. INTRODUCTION	1
2. BASIC CONCEPTS	1
3. MULTI-CHANNEL NEPHELOMETER ASSEMBLY	3
3.1 Projector-Receiver Design	5
3.2 Detector Selection	6
3.3 Optical Configuration	7
3.4 Mock-up Operational Test	10
4. FISHEYE SCANNER ASSEMBLY	10
4.1 Design Concept	11
4.2 Fisheye Lens Selection	12
4.3 Mock-up Operational Test	13
5. ON-BOARD COMPUTER SYSTEM	14
5.1 Hardware Layout	14
5.2 Computational Procedure	17
6. SYSTEM REVIEW	22
7. ACKNOWLEDGEMENTS	26
8. REFERENCES	26
APPENDIX A: Sub-Assembly Spec Sheets	27
APPENDIX B: Simplified Sky Calculations	58
APPENDIX C: Glossary & Notation	62
APPENDIX D: VisLab Contracts & Related Publications	64

LIST OF ILLUSTRATIONS

Fig. No.		Page
2-1	Artist Conception of Contrast Transmittance Monitor	2
2-2	General Program Plan	3
3-1	Airborne Folded Path Integrating Nephelometer, Shroud Open	4
3-2	Airborne Folded Path Integrating Nephelometer, Shroud Closed	4
3-3	Artist's Rendition of Modified Integrating Nephelometer	4
3-4	Compact Nephelometer, Design #15, Optical Layout	5
3-5	Modulated Xenon Illuminator	6
3-6	Pulsed Xenon Illuminator	6
3-7	Compact Projector, with FX132 Lamp	6
3-8	Compact Receiver, with In-Line Sun Shade	6
3-9	Fisheye Lens Performance	8
3-10	Typical Volume Scattering Function Shapes	9
3-11	Compact Nephelometer, Basic Geometry	9
3-12	Compact Nephelometer Mock-up	9
3-13	Compact Nephelometer, Mock-up Performance Test	10
4-1	Automatic 2π Scanner, Active Scan System	11
4-2	Conceptual Outline, Fisheye Scanner	11
4-3	Fisheye Adapter Performance	12
4-4	Fisheye Scanner Mock-up	13
4-5	Image Plane Diffuser Mock-up	13
4-6	Fisheye Scanner, Mock-up Performance Test	14
5-1	On-Board Computer, Preliminary Layout	15
5-2	In-Flight Control Panel, Functional Layout	16
5-3	Basic Data Flow Chart	18
5-4	Ratio Method Flow Chart	20
5-5a	Summation Method Flow Chart	23
5-5b	Summation Method Flow Chart (con't)	24
5-5c	Summation Method Flow Chart (con't)	25

AN EXPERIMENTAL DEVICE FOR REAL TIME DETERMINATION OF SLANT PATH ATMOSPHERIC CONTRAST TRANSMITTANCE

Richard W. Johnson

1. INTRODUCTION

As the deployment of tactically oriented electro-optical systems becomes increasingly commonplace, there is a continuing and concomitant requirement for understanding those environmental factors most influencing their performance. Since in many cases, it is the influence of poor weather conditions upon the transmittance of visible and infrared transmittance that is the primary culprit in degrading EO performances, it behooves us to fully understand, and hopefully to accurately model the characterization of these operational environments. It is in support of this general context that the Visibility Laboratory in cooperation with, and under the sponsorship of the Air Force Geophysics Laboratory conducted an extensive program of airborne optical and meteorological measurements. Many of these previously collected data, all of which were directed toward enhancing our understanding the fundamental elements of contrast transmittance through the troposphere, have been presented in a series of earlier technical reports, among them being Duntley *et al.* (1976), Johnson and Gordon (1980) and Johnson and Hering (1981). The application of these data to the modelling of visible spectrum atmospheric optical properties also has been reported previously in Gordon (1969) and more recently by Hering (1981).

The primary data base upon which both of these visible spectrum atmospheric models have been built consists mainly of profile measurements of volume scattering coefficients and constant but multiple altitude measurements of the 4π radiance distribution surrounding the aircraft (Johnson and Fitch, 1981). Whereas this extensive data base has provided a substantial quantity of highly appropriate and directly useable data for both general modelling and specific slant path contrast transmittance determinations, its acquisition and manipulation have been expensive and time consuming operations. This report discusses a simplified computational procedure and supporting airborne instrument system which is intended to provide near real-time outputs of directional contrast transmittance values, while simultaneously collecting experimental data suitable for addressing the extension of these modelling efforts into both turbid and non-conservative tropospheric environments.

2. BASIC CONCEPTS

There exists a strong and long-standing need for a small, power efficient device for the measurement of key atmospheric optical properties in a broad variety of activities supporting scenarios in military tactical operations, meteorological reporting and forecasting procedures, and fundamental research into atmospheric influences on image propagation.

The airborne instrument system whose development is described in the following paragraphs is intended to fulfill this need. It will accomplish this goal by providing measurements and computations similar to those first described in Duntley *et al.* (1970), but in a simplified form suitable for on-board microprocessor control and display. The desired output from the system is the slant path contrast transmittance along any pre-selected path of sight within the sampled environment (*i.e.* the lower troposphere).

In order to calculate visual spectrum contrast transmittance along any path of sight, one needs a reasonably complete specification of the 4π radiance distribution which surrounds the path of sight, and a specification of the volume scattering function that is representative of the aerosol along the path of sight. When these data are available, then the computational chain yielding directional path reflectance or its equivalent can be structured to match the particular measurement characteristics of the electro optical system being supported. The key computation is that for equilibrium radiance, which is defined by Eq. (2.1) (Duntley *et al.* 1976)

$$L_q(z, \theta, \phi) = \epsilon(z) \left(\frac{\sigma(z, \beta)}{s(z)} \right) + \int_{4\pi} L(z, \theta', \phi') \left(\frac{\sigma(z, \beta')}{s(z)} \right) d\Omega \quad (2.1)$$

where $\epsilon(z)$ is the scalar irradiance of the sun (or full moon), β is the angle between the sun and the path of sight, and $L(z, \theta', \phi')$ is the apparent radiance of the sky or ground for direction θ' and ϕ' . When the sky is fully over-

cast, the first term in Eq. (2.1) is essentially zero. The ratio $\sigma(z, \beta')/s(z)$ is the proportional directional volume scattering function at angle β' and altitude z . The β' is the angle between the path of sight at θ, ϕ , and the sky or terrain radiance at θ', ϕ' . It is found by

$$\sin\theta\sin\theta'\cos(\phi-\phi') + \cos\theta\cos\theta' \quad (2.2)$$

It is the scalar irradiance which designates the flux that enters into the computations of equilibrium radiance and path function when the directional radiances are not known or used. It is the directionality of that flux combined with the directionality of the proportional directional volume scattering function which produces the unique equilibrium radiance associated with each path of sight.

The proportional directional scattering function $\sigma(z, \beta)/s(z)$, that is required for use within Eq. (2.1) has traditionally come from measurements made by an airborne integrating nephelometer, and selections from Barteneva's (1960) catalog. It has been clearly illustrated within our data base that a specification of total volume scattering coefficient is sufficient to specify an appropriate volume scattering function from Barteneva or a set of parameterized equivalents, thus defining the necessary directionalities of any sample aerosol. Whereas the C-130 class nephelometer measured both the total volume scattering coefficient, and the directional scattering function at $\beta 30$ and $\beta 150$ degrees, current modelling activities have indicated that for experimental redundancy an additional measurement of $\beta 55$ degrees would be an attractive option to have available. A simple electro-optical device that would provide these directional scattering data is then essential to the new instrument concept.

If one assumes that there is a device which will provide both the 4π radiance distributions and the directional scattering functions required by Eq. (2.1), then the computational chain illustrated below will yield the additional desired atmospheric properties, following the notation of Duntley *et al.* (1976) as modified in Johnson and Gordon (1980), and Appendix C.

First calculate the point function Equilibrium Radiance $L_e(z, \theta, \phi)$ from Eq. (2.1), then calculate Path Function from

$$L_e(z, \theta, \phi) = L_q(z, \theta, \phi) s(z) \quad (2.3)$$

then calculate Path Radiance from

$$L_p^*(z, \theta, \phi) = \sum_i L_e(z, \theta, \phi) T_{pi} \Delta r \quad (2.4)$$

and finally calculate Directional Reflectance from

$$R_p^*(z, \theta, \phi) = \frac{\pi L_p^*(z, \theta, \phi)}{E(z, d) T_p(z, \theta, \phi)} \quad (2.5)$$

whence Contrast Transmittance

$$C T_p(z, \theta, \phi) = [1 + R_p^*(z, \theta, \phi)/R_o(z, \theta, \phi)]^{-1} \quad (2.6)$$

It should be noted that at each stage of the computation, each of the inputs required by Eqs. (2.1) through (2.6) can be provided by the output from either the 4π radiance measurement or the scattering function measurement. If the airborne system's repetition rate is adequate, measurements and calculations can be made at sufficiently short altitude increments to preclude the need for interpolation.

The goals of this experimental effort are therefore to determine the optimum specification of the radiance measurements needed to adequately define the inputs to Eqs. (2.1) through (2.6), develop the multi-channel radiometer system required to provide these measurements; and develop the processor required to convert the radiance analogs into readily interpretable values of slant path atmospheric contrast transmittance.

The device being developed for the determination of these contrast transmittances is a three part electro-optical transducer system interfaced with a built-in microprocessor. Each of the three transducer assemblies consists of an optical collector feeding a specialized image plane detector array. The detector outputs are operated upon by on-board computer circuits to provide real-time computations for pre-selected slant path optical properties.

A simplified conceptual pictorial illustrating the essential system components is sketched in Fig. 2-1. The airborne system is being developed under a design concept pursuing a low power, solid state, no moving parts philosophy.

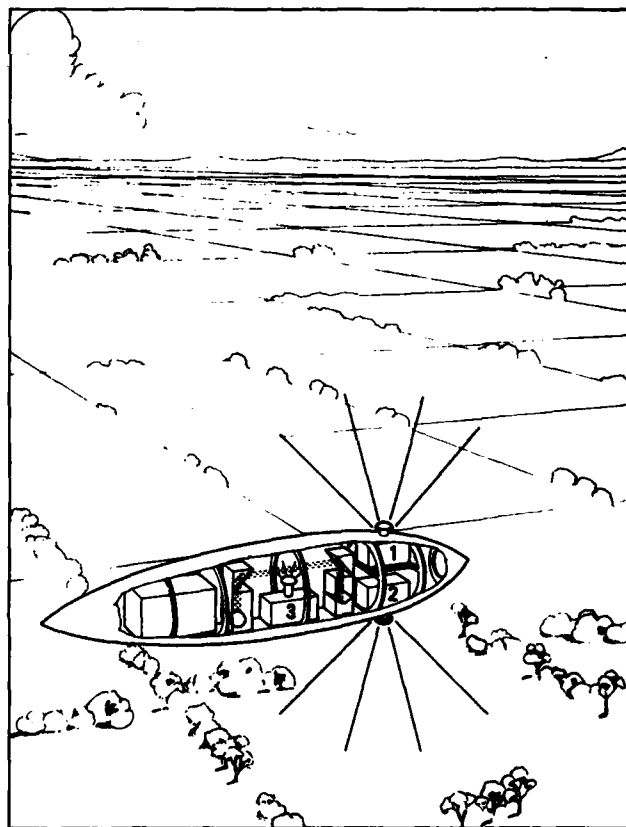


Fig. 2-1. Artist's conception of contrast transmittance monitor.

Assemblies one and two provide upper and lower hemisphere radiance distributions in a form similar to but simplified from those originally provided by the C-130 automatic scanner systems. Assembly three provides directional volume scattering function measurements in a form similar to, but more extensive than, those originally provided by the C-130 integrating nephelometer system. The entire system is conceived as an airborne unit, adequately miniaturized to be packaged in a small aircraft tip tank, an RPV, or general purpose munitions pod. The general program plan for accomplishing this developmental task is outlined in Fig. 2-2.

3. MULTI-CHANNEL NEPHELOMETER ASSEMBLY

There are a variety of electro-optical devices designed to measure the energy scattered from an illuminated volume of aerosol that are calibrated in terms of *visibility*. The EG&G Forward Scatter Visibility Meter described in Hering *et al.* (1971) is one example. Integrating nephelometers similar to those discussed in Charlson *et al.* (1967) are additional examples of devices based upon one or the other of the two techniques described by Beuttell and Brewer (1949). In all cases, these scattering meters utilize the relationship

$$s(z) = \int_{4\pi} \sigma(z, \beta) d\Omega \quad (3.1)$$

where $\sigma(z, \beta)$ is the volume scattering function at scattering angle β and z is an altitude parameter.

Both of the procedures described by Beuttell and Brewer (1949) perform the integration of Eq. (3.1) optically over various fractions of the 4π solid angle so as to include measurements over as broad a range of scattering angles as possible. Fundamentally the two instrumental procedures are optical inverses of one another.

Diffuse Emitter. The first instrumental scheme utilizes a diffuse, *i.e.* cosine corrected light source to illuminate the sample volume of aerosol. The optical collector is normally a small field telescope assembly whose optical axis is perpendicular to the normal from the light source's emitting surface. Instruments of this type have been used by many working in the field of atmospheric sciences from Crosby and Koerber (1963) through Charlson *et al.* (1967) and Horvath and Noll (1969).

Cosine Collector. The second scheme reverses the collector-emitter relationship by utilizing a well collimated projector as a light source to illuminate the sample volume. The optical collector is a cosine corrected flat plate irradiometer whose surface is oriented parallel to the optical axis of the projector beam. This second scheme, which is illustrated in Fig. 3-1, 3-2 and 3-3 has been utilized by Duntley *et al.* (1970 & 1978).

This nephelometer is rather unique in several design aspects which make it a particularly attractive experimental tool. First, the optical system uses a cylindrically limited projector beam, stopped to provide a rectangular beam cross section which provides good geometrical definition of the illuminated volume. Second, the detector assembly's primary optical channel uses a cosine corrected and

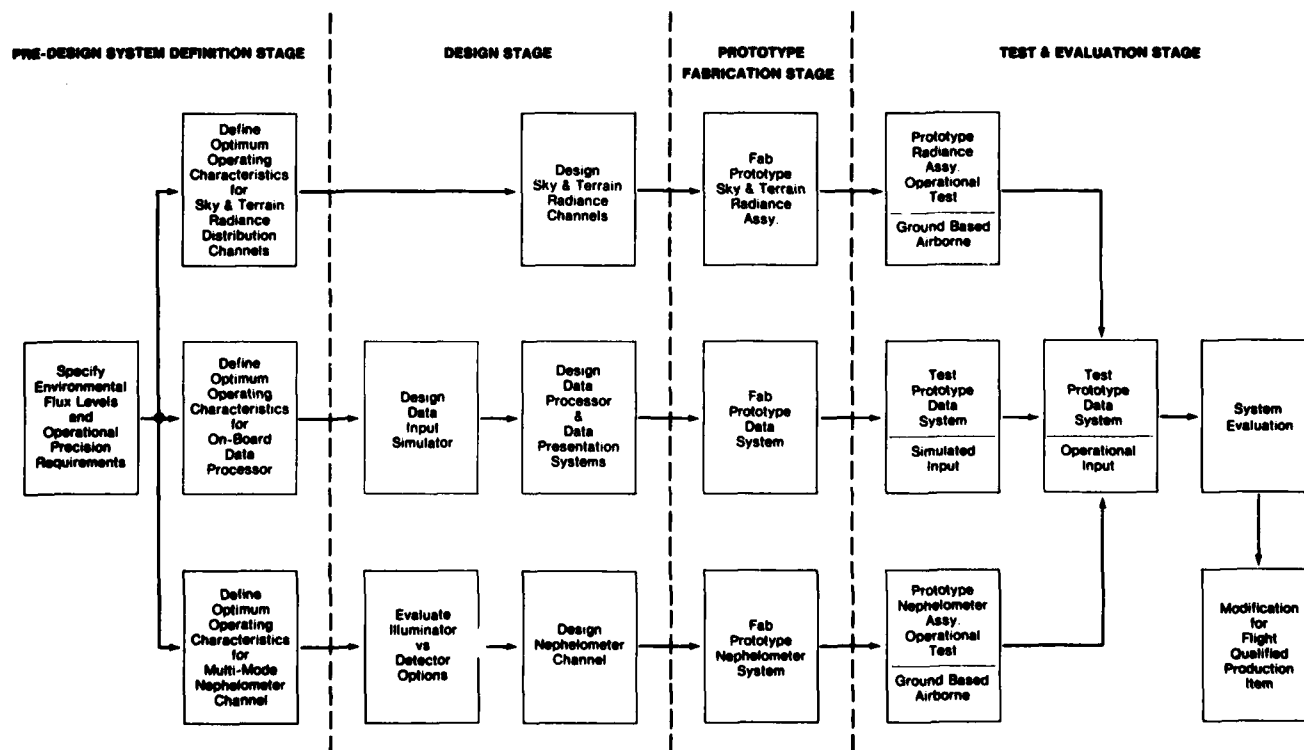


Fig. 2-2. General program plan for prototype contrast transmittance monitor.

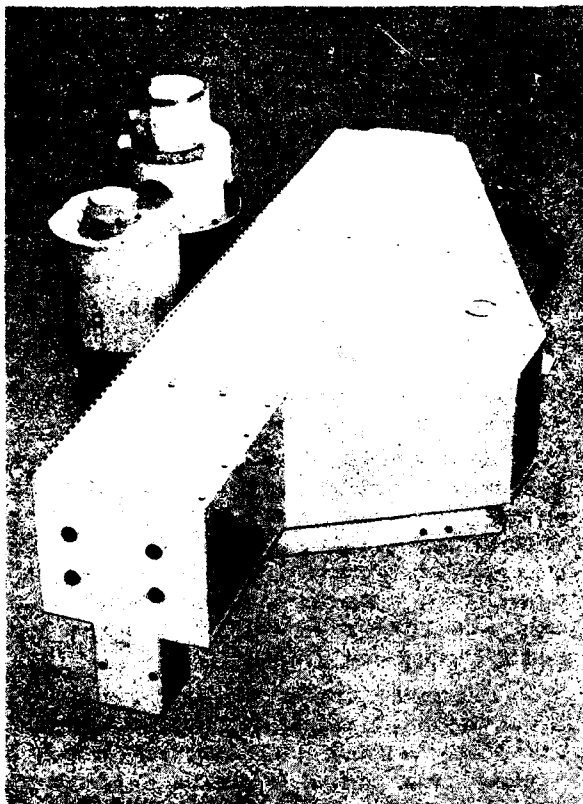


Fig. 3-1. Airborne folded path integrating nephelometer assembly, shroud closed.

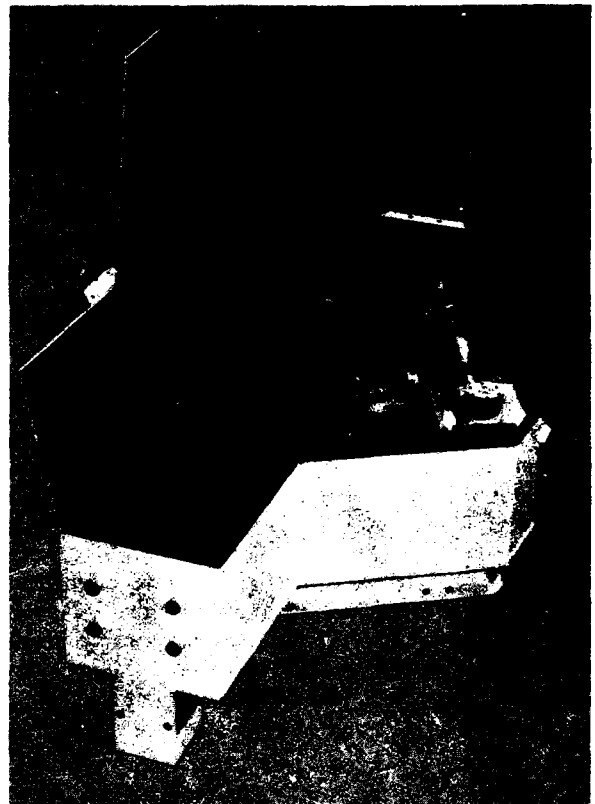


Fig. 3-2. Airborne folded path integrating nephelometer assembly, shroud open.

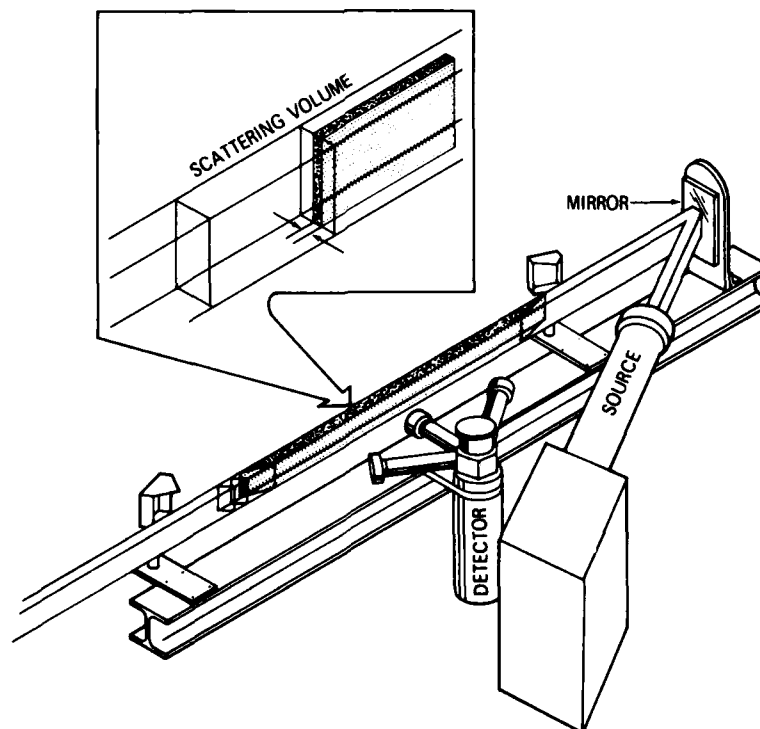


Fig. 3-3. Artist's rendition of modified integrating nephelometer.

mechanically shielded irradiometer head which performs the integration of Eq. (3.1) over all scattering angles between 5° and 172° , minimizing truncation losses of the sort discussed in Fitzgerald (1977), Rabinoff and Herman (1973) and Ensor and Waggoner (1970). Third, the detector assembly's secondary optical channels measure relatively narrow angle, i.e. 2° field of view, directional scattering at both 30° and 150° which allows the determination of a forward to backward scattering ratio that can be used to more thoroughly characterize the sample aerosol. Fourth, the entire device is designed to operate as a ratio measuring system which tends to minimize calibration errors and stability problems.

The operation of this nephelometer is discussed in several recent references, Johnson (1981a) and Johnson and Fitch (1981), with the general consensus being that it performs reliably and consistently when it is properly aspirated. Thus, its design features as enumerated above, were retained for inclusion in the new miniaturized design currently under development.

There were two technical problems that were immediately apparent in the concept of a miniaturized, solid state version of the C-130 system. First, the C-130 class nephelometer utilized photomultiplier detection. By attempting to substitute photodiode detectors, one must give away several decades of radiant sensitivity which must be compensated for elsewhere in the design. Second, the C-130 system, which was designed to operate within several moderately narrow spectral bands within the visible spectrum and over an altitude range of zero to 6 km, employed a 500 watt Xenon short arc projection system as a flux source. This class of projector requires large amounts of electrical power supplied on a continuous basis, and thus is inappropriate for the low power design concept considered here.

A reasonable approach to overcoming the detector/illuminator problems discussed above, is to increase the momentary energy in the projector beam, and also simultaneously increase the collection efficiency in the detector collection optics. Thus, a preliminary plan was established to accomplish both of these increases.

3.1 Projector - Receiver Design

The initial step in the redesign of the nephelometer system was to improve the collection efficiency of the optical system collecting the directionally scattered flux. Whereas the original design shown in Fig. 3-3 generated an illuminated volume approximately 5 cm x 9 cm in cross section, and 107 cm in length for a total sample volume of 4815 cm^3 , the new design was targeted at an illuminated volume 0.7 cm x 2.8 cm in cross section, and 21.5 cm in length for a total sample volume of only 42 cm^3 . With this reduction in illuminated volume, it was essential that other system elements be specified to compensate for this loss if the new system was to operate in a manner similar to the original. Thus, the original cylinder-rectangle intercept between the receiver and projector optical paths was changed to a more efficient rectangle-rectangle intercept. In this mode the new receiver optics would capture the

entire projector beam rather than only about half of it as in the original design. Simultaneously, the field of view of the new collector optics was enlarged from the original 2° to 10° . The preliminary design for this new cylindrically limited receiver-projector configuration is illustrated in Fig. 3-4.

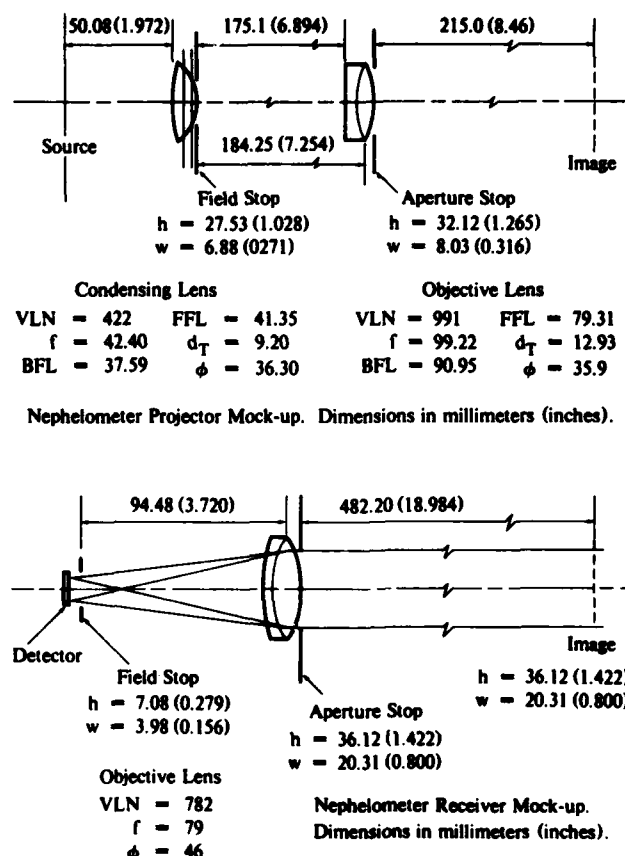


Fig. 3-4. Compact nephelometer design #15.

With the improved flux transfer efficiency anticipated from the optical design shown in Fig. 3-4, the next step was to increase the energy going into the projector beam while maintaining a reasonably low average power consumption. To accomplish this task, two separate illuminator systems were proposed as likely candidates.

The first illuminator candidate used a small, 75 watt xenon short arc lamp powered through a specially designed current modulator circuit. This current control circuit was designed to provide approximately 10:1 current modulation above the minimum simmer current required to keep the lamp ignited. The circuit parameters were established to drive the lamp at approximately 150 cycles per second, with an average duty cycle of ten percent. The bench test unit for the modulated Xenon illuminator is illustrated in Fig. 3-5. In this view the small lamp (Illumination Industries Inc., Type X75-2002, see Appendix A) is shown in the open housing to the left of the scene, and the current control circuit is shown in the open chassis to the right. The primary power supply is not shown in the illustration.



Fig. 3-5. Modulated xenon illuminator.

The second illuminator candidate used a small pulsed lamp system as the radiant flux source. Two different lamp sizes were tested. The first and smaller of the two was an EG&G model FX-201 bulb type Xenon flashtube, rated at a "maximum energy per flash" of 15 joules. This lamp and its test housing is shown in Fig. 3-6. The larger lamp was an EG&G model FX-132, also a bulb type Xenon flashtube, but rated at a "maximum energy per flash" of 200 joules. This larger lamp is illustrated in conjunction with a compact projector mock-up in Fig. 3-7.

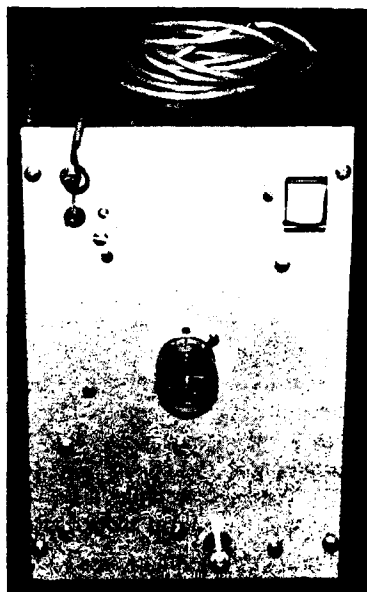


Fig. 3-6. Pulsed xenon illuminator.

Each of the illuminator configurations was evaluated initially using the original C-130 projector-collector optics with an EG&G HUV-4000B (See Appendix A) silicon detector substituted for the original photomultiplier. In each case, the system performance was marginal. Only the forward scattered flux in the β_{30} direction was reliably detected under normal room air test conditions. However, these test runs did provide adequate baseline performance characteristics to guide the follow-on development. These comparative measurements eliminated the use of the



Fig. 3-7. Compact projector with FX-132 lamp.

smaller FX-201 lamp in further competitions, leaving the larger FX-132 and the modulated X75-2002 as the remaining illuminator candidates.

For the final evaluations, the two optical systems illustrated in Fig. 3-4 were both mocked-up. The projector as illustrated in Fig. 3-7 and a single receiver assembly as illustrated in Fig. 3-8.

The receiver mock-up illustrated in Fig. 3-8 is a simple cylindrically limited system in which the vertical dimension of its rectangular field of view completely captures the vertical dimension of the projector beam, and attains maximum intercept efficiency when the midpoint of its field of view (approx. 241mm forward of the objective, see Fig. 3-4) falls at the center of the projector beam. In Fig. 3-8 the black rectangular tube to the right of the scene is an in-line sunshade, the objective lens for the system is housed in the ring mount just to the left of the sunshade, and the detector is shown mounted on the circuit board to the left, the field stop is not installed in this illustration.

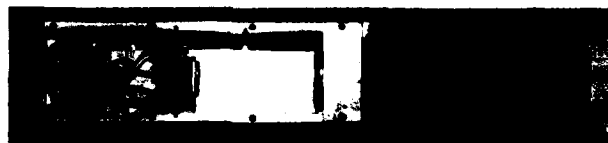


Fig. 3-8. Compact receiver with in-line sunshade.

3.2 Detector Selection

In keeping with the low power, solid state, no moving parts design philosophy guiding this system development, it was desirable to replace the multiplier phototube detector used in the original C-130 system with something simpler. Since the anticipated increase in both optical efficiency and projected beam energy from the new compact projector-receiver system was substantial, i.e. several decades beyond that of the original C-130 system, there was good reason to believe that this was a reasonably achievable goal. Sample calculations indicated that several commercially available photodiode detectors were adequate for the application. After a preliminary specification

check, the four detectors listed below were selected for final evaluation and test.

- 1) EG&G HUV-4000B
1 cm² active area
built-in pre-amp with internal 200 meg Ω feedback resistor
- 2) EG&G HUV-1000B
5.1 mm² active area
built-in pre-amp with external 95 meg Ω feedback resistor
- 3) Silicon Detector Corp. SCD-444-42-12-261
1 cm² active area
built-in pre-amp with external 100 meg Ω feedback resistor
- 4) United Detector Technology PIN 10AP
1 cm² active area
external pre-amp with 10meg Ω feedback resistor

Each of the detectors was calibrated for linearity and sensitivity using a three meter optical bench, calibrated incandescent sources of radiant intensity, and standard photometric practices. In addition to these validations of steady state photometric performance, the various detector assemblies were also checked for dynamic response and stability in reproducing pulse induced outputs for a variety of flash durations.

As one would expect, when the detector pre-amps are operated with the large values of feedback resistance required for developing maximum gain, one pays the price of relatively low frequency response. In determining an optimum operating point therefore, one is normally driven toward the operating region where the circuits reduced frequency response does not allow the detector to fully respond to a short duration pulse of radiant flux. Since this nephelometer design is predicated upon the illuminator operating in either a pulsed or modulated mode, a continuing effort in establishing these optimized time-constant relationships is essential. Thus, as the illuminator's pulse width is made shorter, in order to yield increased peak power output for a fixed power input, there is a point at which the detector is no longer able to fully respond to the pulse. At this point there is no further advantage to be gained by trading peak power for shorter pulse, and an operational threshold is established for the detector configuration being tested. For the configurations considered for this preliminary design (*i.e.* those listed above) this pulse length threshold occurred at pulse widths of approximately 200 microseconds.

Initial evaluation of the test procedures outlined above, coupled with a general review of the vendor provided specifications for each of various detector configurations considered, led to the selection of the EG&G HUV-4000B as the primary choice for use in the further development of the compact nephelometer.

This preliminary selection does not imply endorsement or recommendation of the tested products by the Visibility Laboratory or its sponsors to the exclusion of other products that may be suitable.

3.3 Optical Configuration

In the earliest stages of this system's development, it was proposed that the nephelometer scattering volume be observed through collection optics consisting of a single super wide angle (*i.e.* 180°) lens. This concept was an attractive option since it would provide the ultimate simplicity in optical packaging. The use of these so-called fisheye lenses is widespread, they are readily available in 35mm format although they are not particularly inexpensive. The documentation cameras used on the original C-130 program were adapted to use these lenses quite successfully. Examples of one lens's performance (Traid 735 Periphoto) is illustrated in Fig. 3-9. In Fig. 3-9a&b upper and lower hemisphere pictures of sky, terrain and mechanical features related to the aircraft system are all shown clearly in focus over a broad range of distances and with only moderate distortions. Only the flare associated with the sun's image in 3-9a is an evidence of any potential problem in adapting these lenses to radiometric applications. In Fig. 3-9c, the Visibility Laboratory Hemispherical Sky Simulator, which is used in a broad variety of system test, evaluation and experimental studies is illustrated. Figure 3-9d shows the inside of the sky simulator with a selection of panel intensities established, as seen by the fisheye lens. Angular acceptance relationships and geometrical distortions which characterize the lens system are readily determined via analysis of photographic records such as these.

Two specific disadvantages, from the nephelometer development point of view, which are characteristic of these lenses is their very short equivalent focal length (approx. 6.5mm) and their optical slowness (relative aperture of $f/6.3$). These characteristics were the antithesis of those desired for the compact nephelometer design. To use the 35mm format would imply the use of a self-scanning detector array in the image plane in a not readily available size and format. A CID device such as that used in the General Electric TN2500 solid state camera system, with appropriate optical modifications, is a highly desirable concept for this application, but development costs were deemed excessive. In the end, these considerations, coupled with the geometric constraints imposed by the desire for a very short scattering volume, *i.e.* approximately 20 cm, required the deferment of the fisheye concept within the nephelometer context, and a more classical design embodying discrete detectors was chosen for the next stage of development.

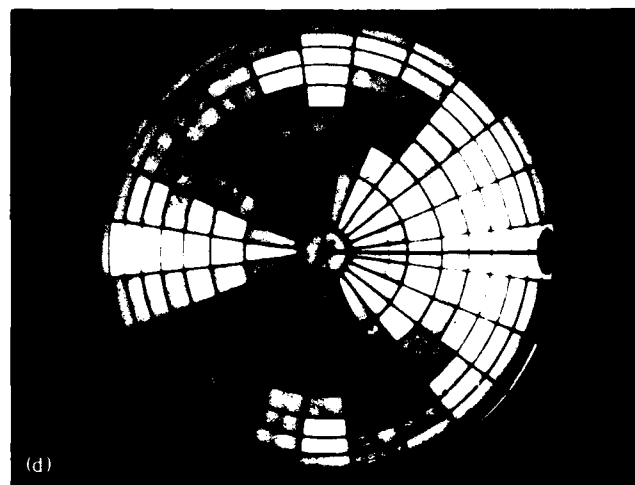
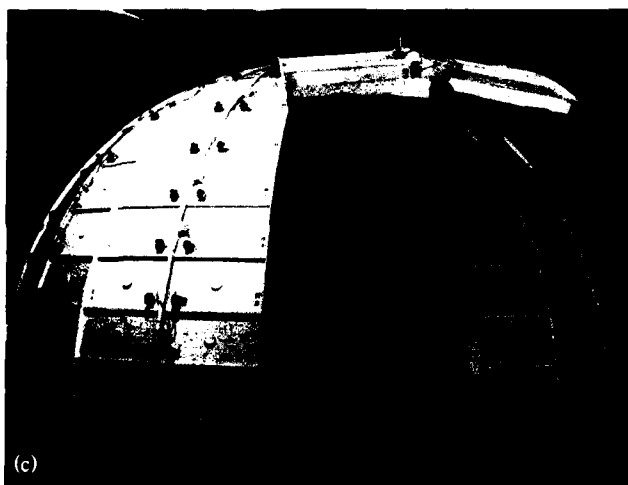


Fig. 3-9. Fisheye lens performance, (a & b) are upper and lower hemisphere photos for flight C-359, 444m AGL, 2342 GMT, (c) Visibility Laboratory Hemispherical Sky Simulator, (d) inside view of sky simulator as seen by the fisheye lens.

As discussed briefly in the opening paragraphs of this section, the function of the multi-channel nephelometer is to provide measurements identifying the magnitude of the volume scattering coefficient $s(z)$ and the shape of the volume scattering function $\sigma(z, \beta)$. The degree of informational redundancy that can be built into the device that makes these determinations will in the end determine its experimental reliability. Thus, whereas the original C-130 nephelometer measured $s(z)$ and $\sigma(z, \beta)$ at $\beta 30^\circ$ and 150° , it was decided to increase the measurements of $\sigma(z, \beta)$ to enhance the reliability of the characterization of the sample aerosol. Scattering functions, typical of the aerosol characteristics to be measured are illustrated in

Fig. 3-10. The functions illustrated in Fig. 3-10a are from Barteneva (1960) and represent directional scattering properties for visible wavelengths between Rayleigh (or molecular) scattering, curve 1a (Visual Range ~ 300 km), and heavy haze Mie (or aerosol) scattering, curve 10 (Visual Range ~ 3 km). The data in Fig. 3-10b, which has been abstracted from Deirmendjian (1969), represents the even more severe scattering conditions anticipated within the Deirmendjian C1 cloud model. With these functions in mind, it was decided to use four angles to specify the character of the aerosol being measured by the new compact nephelometer. The preliminary selection is to use 15° , 55° , 100° and 140° .

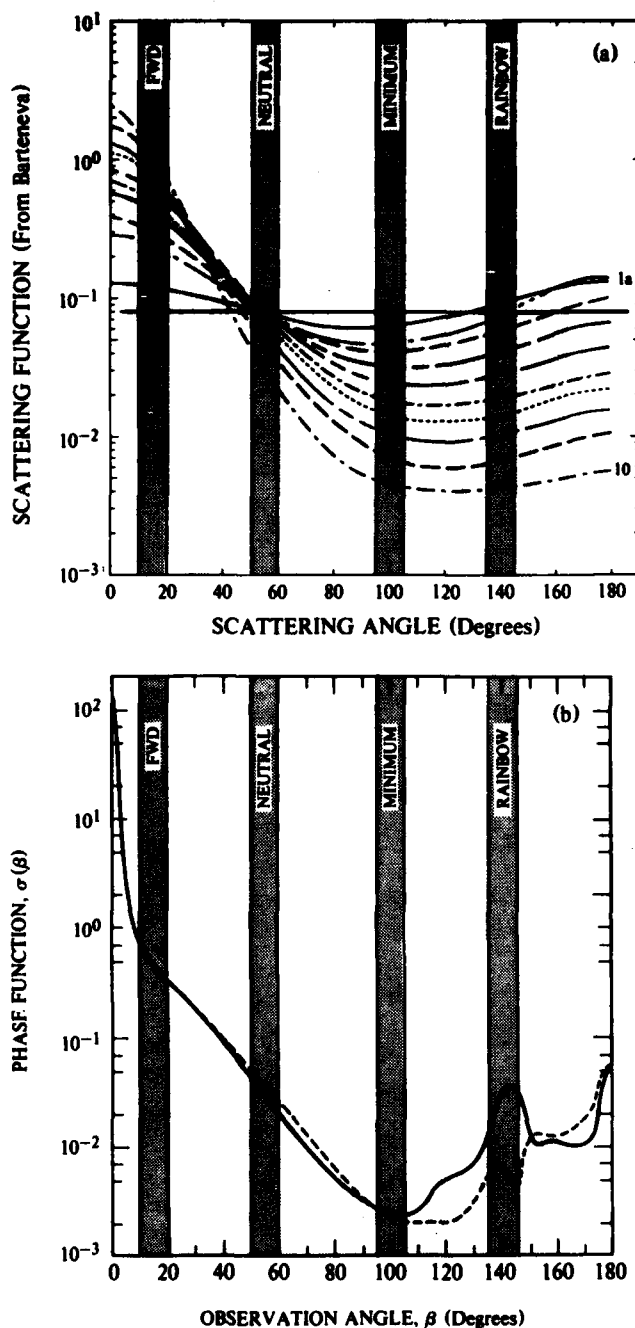


Fig. 3-10. Typical volume scattering function shapes.

Several informational redundancies are available from the four angular measurements selected above, particularly when combined with the fifth measurement, that of total volume scattering coefficient. As discussed in Johnson (1981a) and Hering (1981), the apparent ability for the prediction of $\sigma(z, \beta)$ from a knowledge of $s(z)$ alone presents a strong experimental diagnostic for the reliability of the measurements defining the two sides of Eq. (3.1). The relationship between the forward scatter at 15° and the minimum or backscatter at 100° or 140° is adequate to recreate a close approximation of the total

phase function (volume scattering function) and thus cross-check the simultaneous measurement of $s(z)$. The measurements of the directional scattering in the vicinity of 55° is relatively unaffected by the shape of the phase function, and driven for the most part then by the aerosol concentration alone, a feature that is taken advantage of in the design and calibration of forward scatter visibility meters such as that described by Hering *et al.* (1971). Thus the use of this directional channel as an alternate calibration vehicle is an attractive plus in the design. When the experimental measurements are conducted in increasingly heavy fog and cloud conditions, the transition from haze is markedly identified by the relationship between the directional scattering in the backscatter directions. The ratio between the 100° and 140° scattering should readily identify the regime inhabited by large spherical water drops from that of the drier, more irregular haze aerosols.

Based therefore, upon the considerations discussed in the preceding sections, a preliminary configuration for the new compact nephelometer was established similar to, but smaller and experimentally more powerful than, the original C-130 configuration. The line drawing layout illustrated in Fig. 3-11 shows the basic geometric relationships proposed. The figure is to scale but reduced, the full scale distance between the source and the trap is approximately 21 cm. Also note that, unlike the C-130 version, the integrator channel (Σ) for measuring total volume scattering coefficient is on the opposite side of the flux beam from the directional collection optics, a necessary configuration to enable overall compactness. A full scale mock-up of this general configuration is shown in Fig. 3-12.

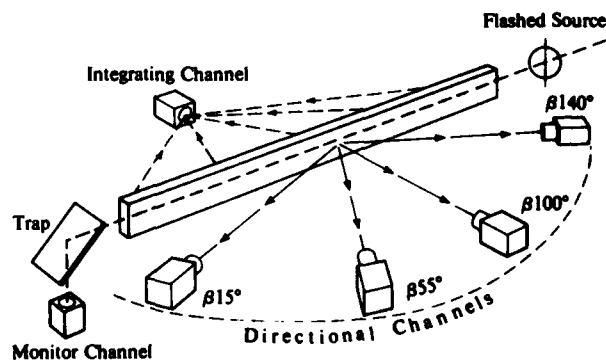


Fig. 3-11. Compact nephelometer - basic geometry.

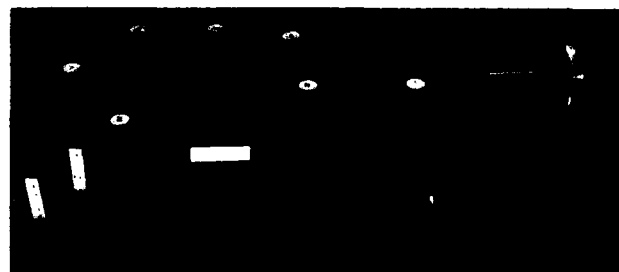


Fig. 3-12. Compact nephelometer mock-up (right angle sunshade).

The full scale mock-up shown in Fig. 3-12 contains a representation of each element proposed for the final design. At the far right, labeled A&B in the figure, is the pulsed Xenon illuminator and compact projector previously illustrated in Figs. 3-6 and 3-7. In the background, the four vertical assemblies with the right angled circular sunshades represent the four directional scattering telephotometers. These mock-up configurations are modeled after the compact receiver design illustrated in Fig. 3-8, but with a right angle prism attached between the objective lens and sunshade to effect additional system compactness. The light grey bar in the center of the photometer cluster represents the illuminated scattering volume produced by the projector system. It extends from the projector (B) into the beam trap on the left. The small assembly to the extreme left, and attached to the back of the beam trap, is the beam monitor assembly. This is the sixth detector circuit associated with the nephelometer design, and is used to monitor the output of the projector pulse as protection against pulse to pulse variations. In the left foreground, the receiver assembly marked (Σ) represents the integrator channel in the nephelometer which measures total volume scattering coefficient directly. Its entrance aperture is a small diffuser button, corrected for cosine collection, and is a scaled down version of irradiance assembly used on the original C-130 version nephelometer. The large light trap in the immediate foreground is conceptual only. In any final design each of the four directional channels will have a small individualized light trap, optimized for the particular viewing and mounting geometries. The necessary power supplies are shown both to the right of and below the projector assembly.

3.4 Mock-up Operational Test

The nephelometer system illustrated in Fig. 3-12 has been operationally mocked-up using the assemblies illustrated in Fig. 3-7 and Fig. 3-8, plus two irradiance channels (not individually illustrated). The electrical signals from the three detector circuits *i.e.* the beam monitor channel, the integrator channel (Σ), and the directional channel (which was used in two selected directional orientations, $\beta 30^\circ$ & $\beta 150^\circ$) were observed and recorded using auxiliary oscilloscope and pulse integration circuitry. The test runs were made in a darkened laboratory environment without external shrouding, and with unmonitored room air as the sample aerosol. Each test consisted of 100 lamp pulses with its associated 100 measurements by each of the three radiometric channels.

A sample plot illustrating the performance of this mock-up system is shown in Fig. 3-13. The linearity plot upon which the data points are superimposed is for the HUV-4000B detector calibrated in the d.c. mode as mentioned in Section 3.2. The data points marked " $\beta 30^\circ$ ", " Σ ", and " $\beta 150^\circ$ " indicate the voltage levels measured during the test sequence outlined above. It is clear that even though the mock-up device is not calibrated in scattering units, the operating points appear nominal. That is, if one assumes that the integrator output voltage (*i.e.* Σ)

represents a scattering coefficient of approximately $10^{-4} m^{-1}$, then the available dynamic range should cover most tropospheric conditions. Likewise the two directional values, marked " $\beta 30^\circ$ " and " $\beta 150^\circ$ " on the performance chart are oriented about the " Σ " measurement in a manner similar to the orientations measured by the original C-130 system. The $\beta 30^\circ$ to $\beta 150^\circ$ scattering ratio of 2.25 would indicate a mean Barteneva scattering lobe between 2 and 3 and a Q *i.e.* optical scattering ratio, s/r_s , Hering (1981), of about 2.5. These values indicate an approximate total volume scattering coefficient of about $3 \times 10^{-5} m^{-1}$ which may be too small. However, the nominal performance of the uncalibrated mock-up system seems reasonable, and certainly adequate to justify further development and refinement.

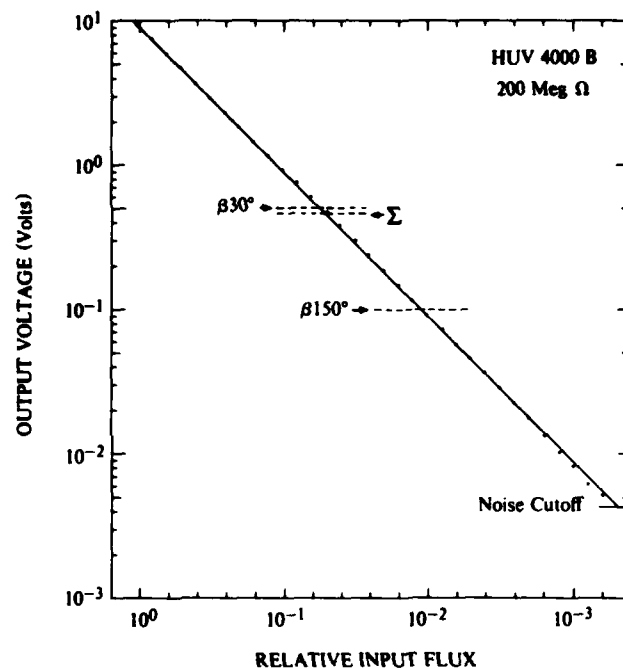


Fig. 3-13. Compact nephelometer - mock-up performance test.

4. FISHEYE SCANNER ASSEMBLY

The computational string discussed in Section 2, as well as many other of the more peripheral computations related to the optical state of the atmosphere, require a reasonable representation of the 4π radiance field into which the computation scenario is embedded. The generation of these radiance data was the function assigned to the automatic 2π scanners which were used with the original C-130 airborne system (Johnson, 1981b; and Johnson and Hering, 1981). This early system is illustrated in Fig. 4-1 which has been abstracted from Johnson (1981b). In this system's operating mode, the azimuth and elevation drive assemblies drove the rotating heads through an automatic search routine in which the 5° field of view of the internal telescope swept the entire 2π hemisphere above the scanner's base plane. The radiometer detector

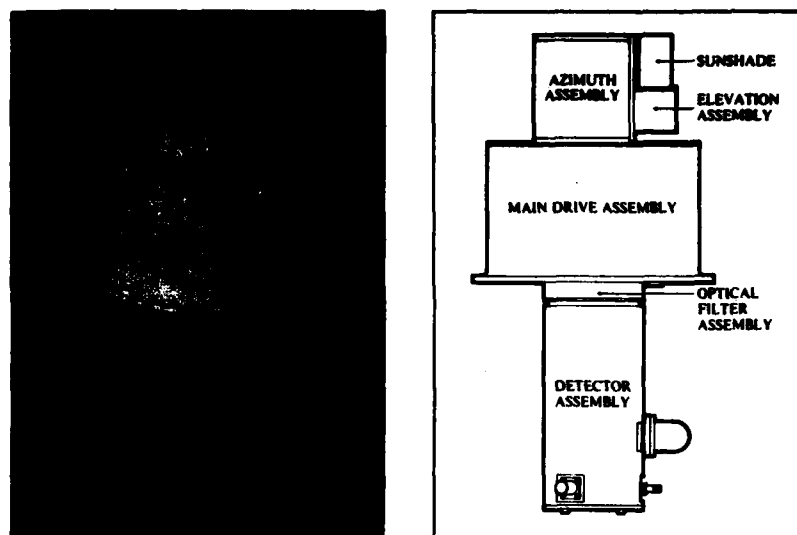


Fig. 4-1. Automatic 2π scanner - active scan system.

and circuitry provided measurements of sky and terrain radiances on a continuous basis, from which data arrays were developed which contained an average field radiance value every six degrees in azimuth and every five degrees in elevation.

As has been illustrated in a series of diagnostic calculations, which will be discussed in Appendix B, it is possible to simplify the integration shown in Eq. (2.1) rather severely without inducing significant error on the resulting values of equilibrium radiance. This computational artifact is a major element in establishing the concept of building a much simplified scanner system. Some preliminary calculations indicate that in lieu of the 800 or so data points used for the integration of Eq. (2.1), by the computer code AVIZC130, Duntley *et al.* (1978), one can divide each hemisphere into as few as eight specially selected zones whose average radiances, when properly substituted into the integral expression, will yield the same results to within $\pm 10\%$. It is upon the basis of these sample calculations that the concept of a simplified staring scanner system has been developed.

4.1 Design Concept

The design concept for the new compact scanner, as was the case for the new nephelometer, is slanted toward a low power, no moving parts system. Thus, the super wide angle lens, which was rejected for the nephelometer design, again becomes an attractive packaging option. The concept of a staring fisheye scanner using solid state detection embodies a variety of desirable attributes, with only minimal penalties, and thus was selected for mock-up and evaluation.

The proposed configuration for the new scanner is illustrated in Fig. 4-2. In this artist's conception of the device, the observed scene is illustrated as the "sample hemisphere" at the top of the figure. The scanner observes this hemisphere through its 180° field of view

"fisheye" lens and images the hemispheric radiance distribution at its image plane. Located in this optical system's image plane is a segmented, diffusely transmitting disc of the same diameter as the image of the observed hemisphere. It is this image plane diffuser that divides the observed scene into a selection of zones, and performs the optical integration that allows the detection of each zone's average radiance. The configuration illustrated in Fig. 4-2, implies an individual detector behind each zone in the diffuser *i.e.* behind each of the six numbered zones shown in the figure, plus four behind the smaller unnumbered zones. It is the radiometric measurement made by these detectors which provides the radiance values used in the solution of the Eqs. (2.1) through (2.6).

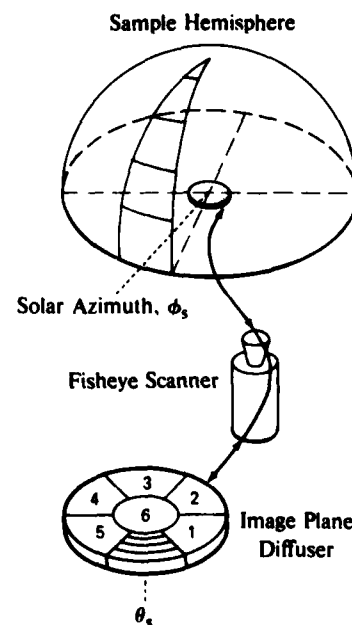


Fig. 4-2. Conceptual outline - fisheye scanner.

The zone arrangement illustrated in Fig. 4-2 is only one of many possible configurations, and is chosen in this initial layout for simplicity of illustration and mock-up. Since the zone pattern determines the solid angles of integration for Eq. (2.1) (or more accurately, the summation which approximates Eq. (2.1)), it is apparent that it must be designed to define and isolate each of those zones which most significantly contributes to the upper hemisphere's radiant directionality. In particular, the zones which will contain the image of the solar disc and aureole must be carefully specified.

4.2 Fisheye Lens Selection

In order to demonstrate the feasibility of a relatively compact, solid state staring scanner, one need only select an acceptable fisheye lens and detector, since any reasonable diffuser configuration is suitable for test purposes. Two lens configurations, and two detector configurations were considered for this initial mock-up, and in each case the simpler of the two was chosen for actual assembly and test.

The super wide angle lens is of course the key element in this compact scanner concept. It must be of adequate quality to provide the necessary imagery, but not so sophisticated as to command an exorbitant cost. The two lenses evaluated for this mock-up represent two different cost and quality options, both of which have specific advantages.

The first lens to be considered was the Traid 735 Periphoto (Appendix A). This 180° lens was designed for use with 35mm cameras, and was adapted for use with the G1 Automax cameras which were part of the original C-130 system. Several samples of this lens' performance are illustrated in Fig. 3-9a,b&d. The lens has excellent coverage and minimal distortion. For this staring scanner application however, it has two disadvantages. It was a relatively expensive lens when acquired, and lenses of its general quality are still priced at around \$1000 each. Secondly, it was designed specifically for use with 35mm

cameras and thus has its focal plane very near its exit pupil (*i.e.* ~6.5mm). This feature provides very little mechanical clearance which makes it difficult to insert additional optical elements in the flux path in order to adjust the image size and/or the spectral passband. In fact, the mechanical inflexibilities imposed by this short focal length, highly divergent design made it impractical to consider this class of lens for consideration in the discrete detector concept proposed for this mock-up.

The second lens considered was the Soligor fisheye conversion lens (Appendix A). This 180° Adapter lens is designed for use with a broad variety of prime lenses yielding, in each particular combination, a resultant focal length of 0.15X the prime focal length. Thus a standard 50mm focal length is, with the adapter, converted to 7.5mm. The essential feature is that the flux bundle emerging from the exit pupil of the adapter lens is highly collimated and about 10mm in diameter. Thus a broad variety of secondary lenses can be readily located within this flux bundle to alter the resultant image diameter, and also allow space for the insertion of additional optical elements. This Soligor adapter, priced at about \$150, has been used by the Visibility Laboratory ground truth team on a variety of SLR and range finder class 35mm cameras with good results. Several samples of this adapter system's performance are illustrated in Fig. 4-3, which can be compared with the Traid 735 performance as shown earlier in Fig. 3-9.

As can be noted in a comparison between Figs. 3-9d and 4-3a, the Soligor adapter, in this particular configuration, does not in fact produce a full 180° coverage. An approximate determination indicates coverage of 175°, thus in documenting upper hemisphere sky radiances, the system will miss the 5° nearest the horizon. In all other respects the adapter is quite acceptable, particularly in its adaptability to a variety of optical and packaging configurations. Based upon the characteristics just reviewed, the Soligor fisheye adapter was chosen as the primary optical element in the new staring scanner.

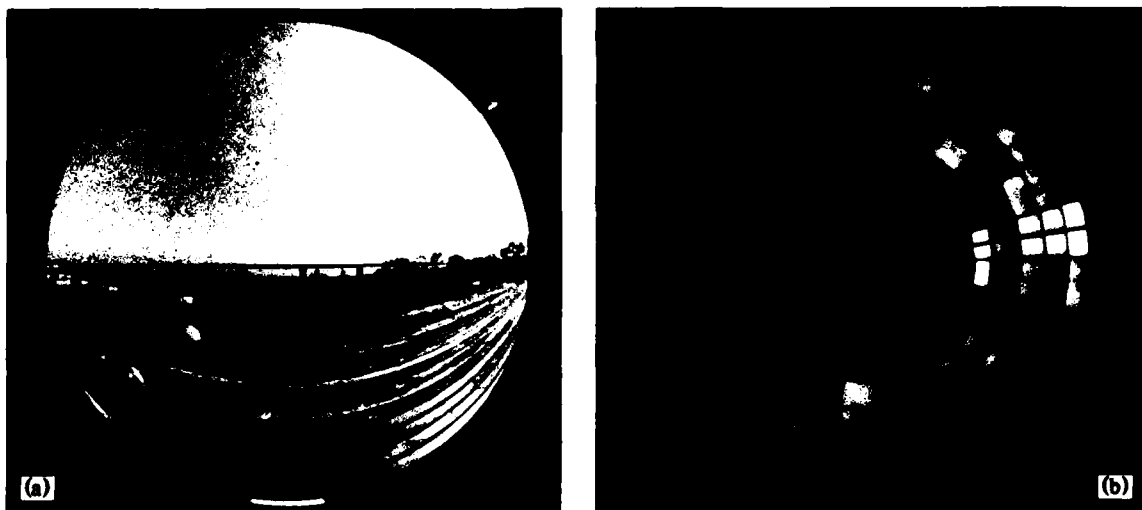


Fig. 4-3. Fisheye adapter performance.

4.3 Mock-up Operational Test

With the choice of the optical system concluded, the only additional mock-up decision was with regard to detector choice. Since the HUV-4000B had been chosen for the nephelometer, as discussed in Section 3.1, it was decided to stay with the same series in order to maintain a minimum number of component and sub-assembly design features, and subsequently minimize the complexity of the downstream spare parts inventory. Thus, the HUV-4000B was chosen as the detector to be used with each of the scanner's large zones, and the HUV-1000B was chosen for each of the smaller zones associated with the solar azimuth. (See Fig. 4-2, where $\phi_s \equiv$ solar azimuth). The detectors would both operate in the d.c. mode for the fisheye scanner application, rather than the pulsed mode used in the nephelometer.

The mock-up configuration for the fisheye scanner is illustrated in Figs. 4-4 and 4-5. In the full assembly view of Fig. 4-4, the compact, in-line design of the system is clearly apparent. In this configuration, the Soligor adapter is used in conjunction with a 210mm focal length auxiliary lens in order to expand the image into a relatively large diameter (*i.e.* 10cm). This degree of expansion is chosen as a convenience to facilitate the mock-up using the standard TO-5 configuration for the smaller HUV-1000B detector. The spectral filter is inserted into the optical path between the Soligor adapter and the auxiliary lens such that a single filter is used for all optical

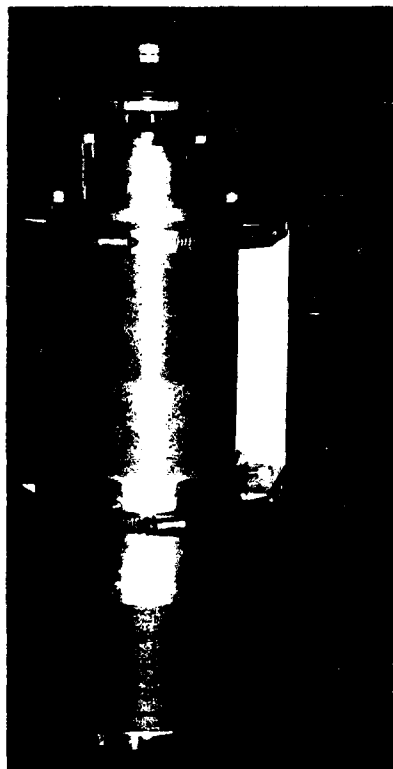


Fig. 4-4. Fisheye scanner mock-up.



Fig. 4-5. Image plane diffuser mock-up.

channels. Any moderate mismatches due to variations in individual detector sensitivities can be corrected at the data processing level. The overall size of the scanner in this particular arrangement is 12cm in outside diameter and 42cm in length.

Figure 4-5 illustrates the image plane diffuser used in the mock-up evaluation, and the discrete detector array. The diffuser plate illustrated on the right of the scene is similar to the pictorial representation shown in Fig. 4-2, and does not represent the optimum design, but rather one easy to fabricate and yet adequate for test and evaluation. The discrete detector array shown in the left of the scene contains both HUV-1000B and HUV-4000B detectors. The smaller TO-5 assemblies were evaluated in both the small sun zones (the linear set in the nine o'clock position) and the larger sky zones. The larger HUV-4000B detector was only used in the single sky zone shown in the twelve o'clock position.

Using the assembly shown in Fig. 4-4, several operational evaluations were conducted to demonstrate the practicality of this particular design concept. The device was used on both clear and overcast days, in orientations which measured the average radiance as detected in both the larger sky zones and the smaller sun zones. Several typical results are shown in Fig. 4-6. The unmodified operational span for each detector is illustrated by its linear voltage vs flux calibration. Superimposed upon each of these plots are several data points representing the system's response to the atmospheric conditions extant during each test. As anticipated, the observed flux levels are more than adequate for detection by the system. The operating span is adequate to accommodate a variety of modifications in the design of the image plane diffuser. Thus the optimization of the solid angle increments most efficient for use in Eq. (2.1) can proceed without fear of compromise due to instrumentation limitations. The nominal performance of this uncalibrated mock-up system seems reasonable, and as in the case of the nephelometer system discussed previously, more than adequate to justify further development and refinement.

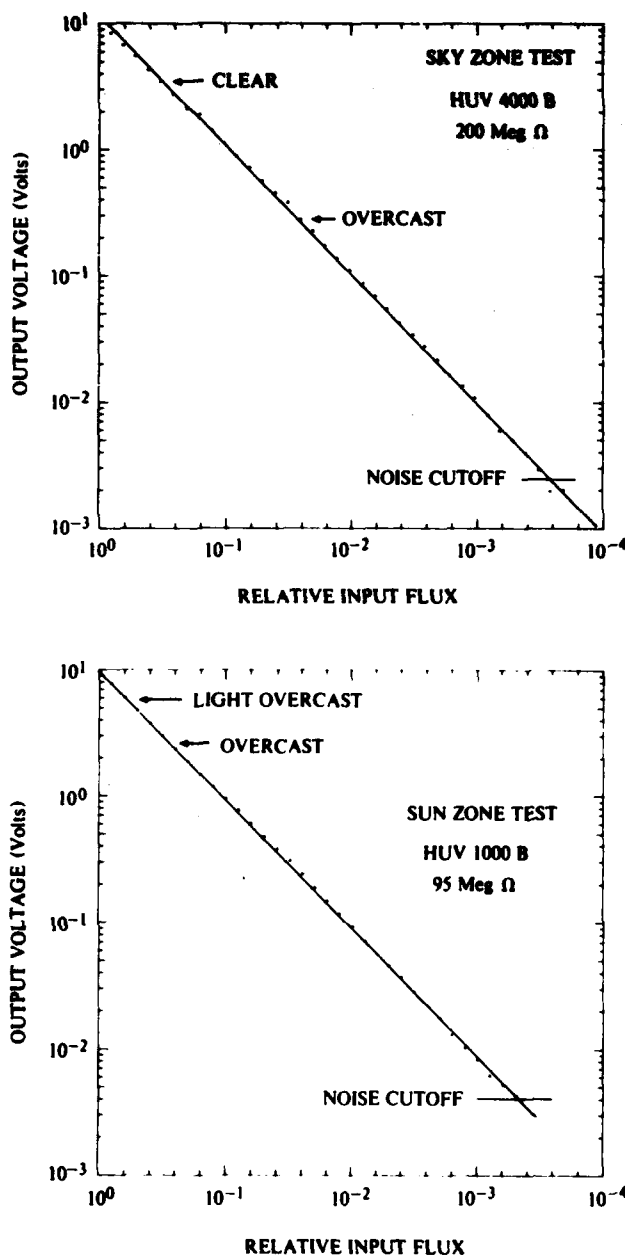


Fig. 4-6. Fisheye scanner - mock-up performance test.

5. ON-BOARD COMPUTER SYSTEM

The on-board computer system associated with this instrumentation package has several related but operationally independent responsibilities. They are summarized in the listing below.

1. Accept the raw data stream from each transducer.
2. Store raw data on tape for later retrieval.
3. Convert raw data into useable engineering units.
4. Perform pre-determined computations.
5. Store computed values for later retrieval.

6. Provide real-time display of selected raw and derived values.
7. Perform associated housekeeping to enable actions 1-6.

The design goal for this system is to be flexible enough to perform in semi-automatic mode under EPROM control and also, with only minimum modification, perform in operator inter-active mode. These two operational configurations are illustrated by the block diagrams shown in Fig. 5-1. In general it is assumed that most data collection flights will be accomplished in the semi-automatic mode, with only minimal control by the operator. The interactive mode is assumed to be primarily a pre or post flight operation used for troubleshooting, extended data analysis, and new EPROM program development.

5.1 Hardware Layout

The general system outline is diagrammed in Fig. 5-1, and is shown in both the airborne data collection configuration (semi-automatic), and the laboratory test and evaluation configuration (interactive). As is apparent in the diagram, both configurations are quite similar. The general function of each of the block diagram elements is outlined in the following paragraphs.

OPT & MET TRANSDUCERS

These transducers, as described in Sections 3 and 4, provide the experimental measurements for input to the computational scheme. The upper and lower hemisphere scanner (UHS & LHS) channels are from the two fisheye systems. The current design calls for about ten analog signals from the UHS and about six from the LHS. These dc signals represent the radiance of each of the upper and lower hemisphere segments that are observed by the two scanners. The current nephelometer uses six channels to provide its data, four directional radiances, one integrated irradiance, and one irradiance monitor. These pulsed signals must be conditioned differently than the simple dc signals provided by the scanners. The nephelometer illuminator provides no information flow to the computer, except indirectly through the irradiance monitor channel, but its firing rate and synchronization are controlled by the computer. The basic meteorological transducers for pressure (altitude) and temperature are also planned as simple dc analogs.

VIS LAB SIGNAL CONDITIONER, MPLX & TRANSFER

This is the first of the four basic building blocks from which the on-board computer system is being assembled. It forms the communications interface between the OPT/MET transducer systems, the computer CPU, and the in-flight fixed display panel. The custom built design is similar to that employed in a previously deployed underwater system, which also uses a pulsed illuminator to produce multiple irradiance analogs. The circuitry has proven

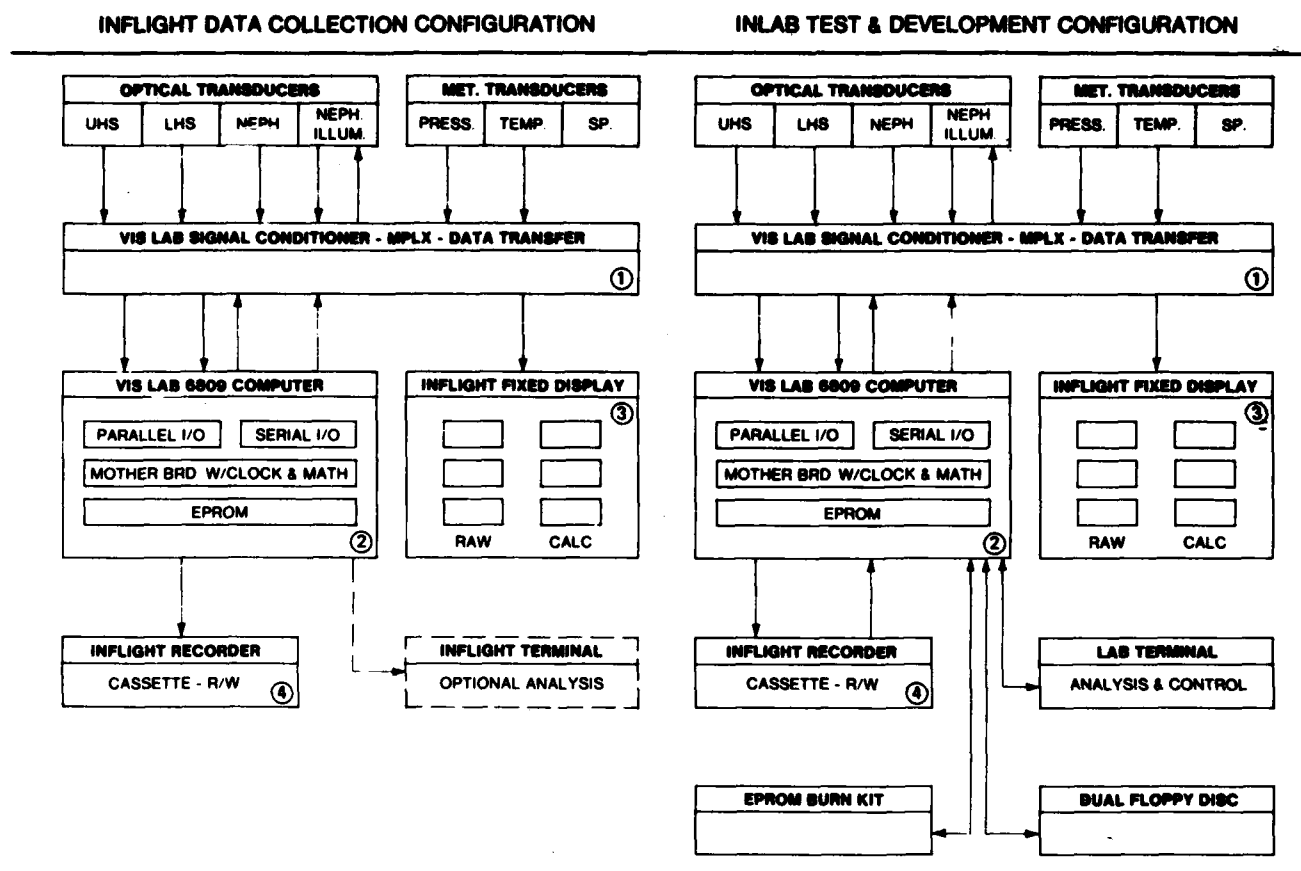


Fig. 5-1. On-board computer - preliminary layout.

to be reliable, and the panel from the earlier system was in fact used during the mock-up runs of the compact nephelometer. The pulse integration and channel multiplexing features are the most important, and should be carefully reviewed to insure their optimum configuration for this new application.

VIS LAB 6809 COMPUTER

This is the second of the four basic building blocks. The 6809 based system has been selected on the basis of several considerations, but primarily due to its expandable EPROM configuration, our in-house experience with this hardware, and the readily available OMEGA SOFT PASCAL software development tool. This microprocessor will provide an appropriate entry into the use of a PASCAL based design aid (OMEGA SOFT), and in conjunction with the background obtained at the recently attended ADA Seminar, should put this system in good shape for complying with any downstream DoD requirements. The availability of built-in real-time clock and mathematics chips was also a consideration, however not unique to this product line.

This single board computer system will provide multiple I/O ports for both parallel and serial communication with the recorder and display panel. The basic specifications for this microprocessor are illustrated in the

attached Chieftain flyers (Appendix A). The computational capabilities required of this micro-processor are described in Section 5.2.

IN-FLIGHT FIXED DISPLAY

This is the third of the four basic building blocks. The function of this display panel is to provide an in-flight operator or monitor with a selected set of measured and derived quantities for real-time assessment and/or troubleshooting. It is considered a passive display, in that it exerts no control over the transducer/computer operation, it only observes its performance. The panel is intended to provide a display of the nephelometer measurements of $\sigma(z, \beta)$ and $s(z)$ the directional and total scattering values, upwelling and downwelling irradiances, time, altitude and a pre-determined set of computed contrast transmittance values.

The only operator inputs are related to procedural control. e.g. altimeter calibration for QNH or QFE, tape control, etc. Physically, the in-flight display is the front panel on the signal conditioner and multiplexer chassis, it is not a completely separate black box. The display panel does however provide for a remote capability in its system control functions.

A functional block diagram of the in-flight display is illustrated in Fig. 5-2.

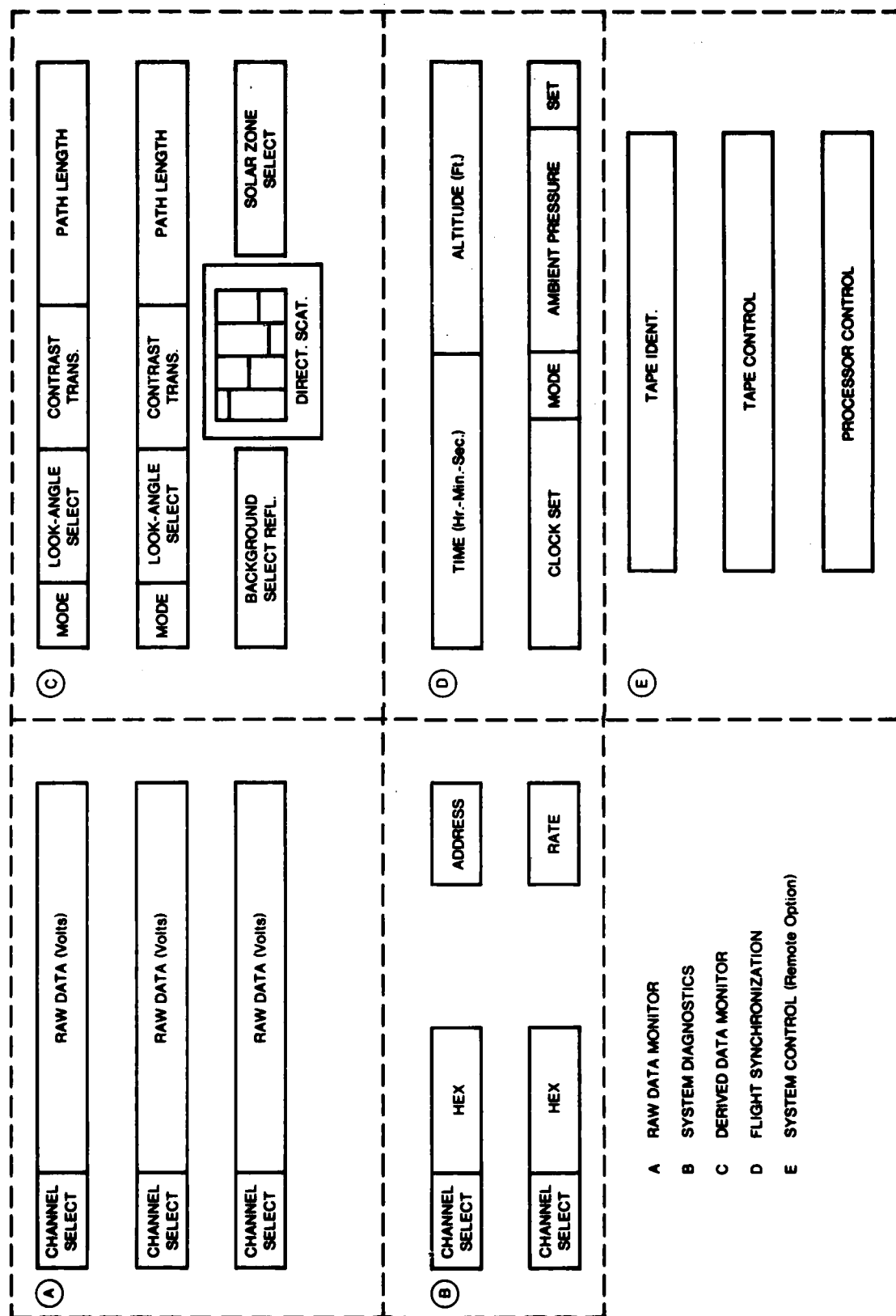


Fig. 5-2. Inflight control panel - functional layout.

IN-FLIGHT RECORDER

This is the fourth of the four basic building blocks. The function of this recorder is to retain the measured and derived quantities as determined during any flight episode for later recovery and analysis. No specific selection has been made at this time, however the basic performance requirements are being formulated. The initial proposal is for recording and playback in multiples of 15 minute segments (the estimated flight time for one 0 to 5000' profile) with one hour per cassette the target duration. Preliminary estimates of the required data flow indicate a need for approximately 50 kilobytes of storage capacity for each unit data package. Thus typical tape unit capacities of around 250 kilobytes seem adequate for the proposed multi profile missions. Based upon initial investigations, the Memodyne M-80 (see Appendix A) seems to be an attractive choice. It has performed well in a recent Navy sponsored aircraft program, and at an OEM price of about \$2400 is not prohibitively priced. It may, however be overly sophisticated for this system's requirements.

OPTIONAL IN-FLIGHT TERMINAL

This terminal is not part of the experimental system *per se*. It is an auxiliary piece of equipment which may be used for in-flight analysis and interpretation of the data beyond the level enabled by the fixed display. If the flight vehicle is of adequate size, then the project scientist with the aid of this smart terminal can address the real-time data base and perform in-flight analysis and evaluations beyond the scope of the canned EPROM procedures. In the event the vehicle cannot support this luxury, then the recorded data may be manipulated further subsequent to the retrieval of the cassette.

As an alternative flight procedure, the EPROM control of the computer can be removed prior to flight, and the optional smart terminal can be used to control the system up to the limitation imposed by its resident memory.

When the system is in the Laboratory, it can operate in either of two modes, under full EPROM control as when in semi-automatic flight mode, or with the EPROM board removed and the system running under the control of the keyboard and the in-house programs stored on the auxiliary disc system. In this in-house, interactive mode one has the option of normal operation, troubleshooting, new program development and new or replacement EPROM burning. The in-house terminal, disc system and EPROM burn kit are not part of the airborne system, but are auxiliary Laboratory equipments which are currently on-hand from previous contracts.

5.2 Computational Procedures

The following paragraphs outline the computational sequences that are anticipated from the on-board computer when operating in its canned EPROM mode. Basically, the calculations use input data from the NEPH, UHS, LHS and altitude channels to produce values of contrast transmittance along a pre-selected set of look angles. There are two computational routes to accomplish this

task, and they are referred to as the Ratio Method and the Summation Method. The Summation Method follows the classical computational route used by the C-130 group via the Gordon AVIZC130 code. Duntley *et al.* (1976). It is more precise but more difficult. The Ratio Method is an equally valid procedure for relatively small fields of view, but will suffer somewhat from the large zones used by the sky scanner. In any case, the computer will be set up to provide both computations on each set of airborne measurements.

FLIGHT REQUIREMENTS

It is assumed that the airborne vehicle will traverse a specific, predefined flight pattern during the data acquisition interval, which will establish the basic directional coordinate system. The pattern defined as follows is to be considered the unit pattern for one set of calculations. Repetitions will normally be in integral multiples of the unit pattern. The flight pattern is a simplification of that used in the original C-130 flight program as described in Duntley *et al.* (1976).

The basic features of this experimental flight pattern are outlined as follows:

- a. The vehicle will fly directly into the sun during all data collection intervals. This locates the image of the solar disc in the appropriate sun zone of the scanners diffuser plane, and thus establishes the azimuth of each zone centroid with respect to the sun.
- b. The vehicle will make a minimum altitude pass over an arbitrary terrain landmark, and interrogate the optical transducers while over the mark. (Estimate 15 sec. run.)
- c. The vehicle will climb to its maximum altitude interrogating the nephelometer continuously during the climb. (Estimate top altitude 5000 ft. AGL, climbing at 500 fpm, yielding estimated climb time of 10 minutes.)
- d. The vehicle will make a maximum altitude pass over the initially selected landmark, and interrogate the optical transducers while over the mark. (Estimate 15 sec. run.)

This nominal flight pattern will yield adequate data input for both the ratio and summation methods described in the following paragraphs. It can be repeated and/or altered substantially depending upon the available memory in the on-board computer, and the tape recorder's capacity. The basic data acquired during each flight pattern for subsequent use in all computational procedures is outlined in Fig. 5-3.

RATIO METHOD

The spectral contrast transmittance of the path of sight can be expressed (see Duntley *et al.* 1957) directly as the product of the path transmittance, $T_p(z, \theta)$, and the ratio of the inherent, ${}_bL_o$, and apparent, ${}_bL_r$, background radiances as follows:

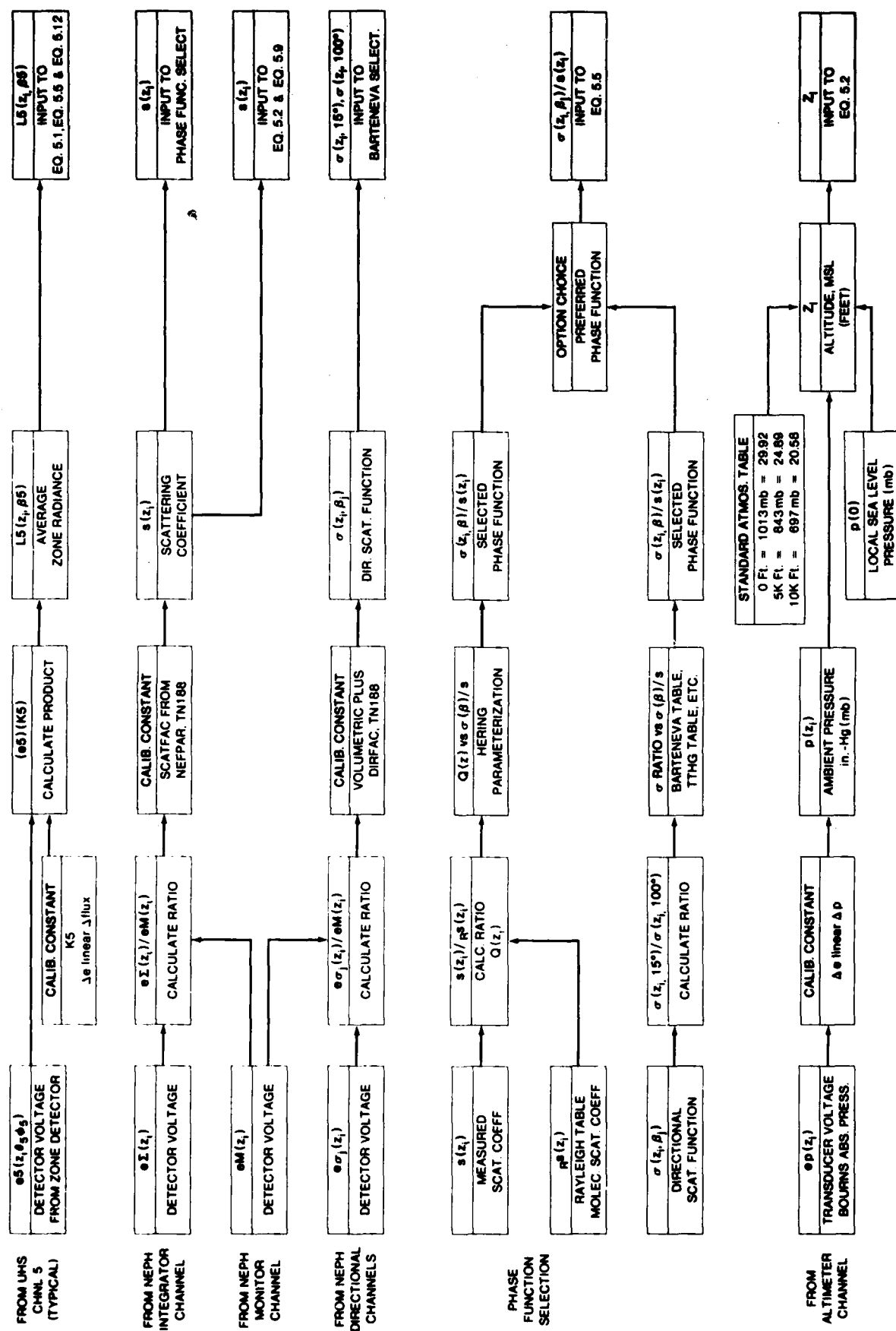


Fig. 5-3. Basic data.

$$C_r(z, \theta, \phi) / C_o(z, \theta, \phi) = T_r(z, \theta) {}_b L_o(z, \theta, \phi) / {}_b L_r(z, \theta, \phi), \quad (5.1)$$

where $C_r = ({}_r L_r - {}_b L_r) / {}_b L_r$, is the apparent target contrast at path length r , $C_o = ({}_r L_o - {}_b L_o) / {}_b L_o$ is the inherent target contrast at altitude z , and ${}_r L_o$ is the inherent target radiance. Thus, the contrast transmittance of a given path does not depend upon intrinsic target characteristics but is a function only of the directional radiance distribution in the atmosphere and the path transmittance. The expression is strictly applicable only for monochromatic radiation but may be applied with good approximation to reasonably broad spectral bands in the visible portion of the spectrum.

The ratio method for computing contrast transmittance is defined by Eq. (5.1) above.

The ratio ${}_b L_o / {}_b L_r$ is determined by the low altitude and high altitude radiances measured by the scanners. There will be one ratio per unit profile for each of the UHS and LHS zones illustrated in Fig. 4-2 and 4-5.

Radiance Transmittance

The radiance transmittance $T_r(z, \theta)$ is obtained directly from the total scattering coefficient $s(z)$ as measured by the nephelometer by means of Eq. (5.2). When there is no significant atmospheric absorption in the passbands of the measurements, e.g., from smoke, dust, or smog, the attenuation coefficient $\alpha(z)$ is equivalent to the total volume scattering coefficient $s(z)$. Therefore,

$$T_r(z, \theta) = \exp \left[- \sum_{i=1}^n \alpha(z_i) \Delta r \right] = \exp \left[- \sum_{i=1}^n s(z_i) \Delta r \right], \quad (5.2)$$

where Δr is the incremental path length. The summations are made using the trapezoidal rule. The measured total volume scattering coefficient data may be extrapolated to ground level when no ground-based measurements are available. The extrapolation assumes that the scattering particles are the same at the near-surface altitudes, but decrease or increase according to the density at each altitude $\rho(z)$. For all paths of sight at zenith angles less than 85 degrees or greater than 95 degrees, Δr equals $\Delta z \sec \theta$ for these altitudes. The $|\Delta z|$ used is 30 meters (98.4 feet). For zenith angles greater than 95 degrees, the radiance transmittance can also be expressed as a function of the vertical radiance transmittance $T_r(z, 180^\circ)$ as follows:

$$T_r(z, \theta) = T_r(z, 180^\circ)^{|\sec \theta|}. \quad (5.3)$$

For upward paths of sight for zenith angles less than 85 degrees, the radiance transmittance can similarly be expressed as a function of the vertical upward transmittance $T_r(z, 0^\circ)$.

The block diagram for computations using the ratio method is illustrated in Fig. 5-4. Note that in this procedure, each zone in the upper and lower hemisphere is assigned a nominal direction vector θ, ϕ , to which the con-

trast transmittance value will be assigned. Thus the size of the zones tends to smear the directionality of the diffuse contribution and some precision problems may ensue.

SUMMATION METHOD

The Summation Method for calculating slant path contrast transmittance follows the traditional computational chain established in the AVIZC130 code and outlined most completely in Duntley *et al.* (1976). The primary short-cut that this new system employs is the approximation of the precision sky scanner integrals by the fisheye zone averages. These average zone radiances are used in conjunction with the normalized directional scattering function as derived from nephelometer data to calculate equilibrium radiance.

Equilibrium Radiance

In the traditional calculations, the equilibrium radiance is computed from the measurements made at each of the altitudes of level flight and then interpolated and extrapolated to obtain values at each 30-meter (98.4 foot) interval z_i . Equilibrium radiance is interpolated rather than path function since the equilibrium radiance is relatively invariant with altitude within the lower troposphere, whereas path function is sensitive to changes in aerosol scattering as well as the lighting distribution. To compute the equilibrium radiance Eq. (5.4) is used, wherein the full angular precision in the measurement of the 4π radiance field is fully utilized.

$$L_q(z, \theta, \phi) = s(z) \frac{\sigma(z, \beta)}{s(z)} + \int_{4\pi} L(z, \theta', \phi') \frac{\sigma(z, \beta')}{s(z)} d\Omega, \quad (5.4)$$

In the Summation Method, the equilibrium radiance is computed in a similar manner, but using Eq. (5.5), which uses average zone radiances in lieu of the integral,

$$L_q(z, \theta, \phi) \approx \sum_{4\pi} {}_s L_1(z, \theta', \phi') \frac{\sigma(z, \beta)}{s(z)} \Delta \Omega + L_2(z, \theta', \phi') \frac{\sigma(z, \beta)}{s(z)} \Delta \Omega + \dots + L_n(z, \theta', \phi') \frac{\sigma(z, \beta)}{s(z)} \Delta \Omega. \quad (5.5)$$

where

${}_s L_1$ is the average radiance measured in the sun zone

L_2 is the average radiance measured in the first sky zone

L_n is the average radiance measured in the last sky zone

$\frac{\sigma(z, \beta)}{s(z)}$ is the normalized phase function as determined from the nephelometer measurements and/or look-up tables using Henyey-Greenstein data

$\Delta \Omega$ is the solid angle observed by each scanner zone.

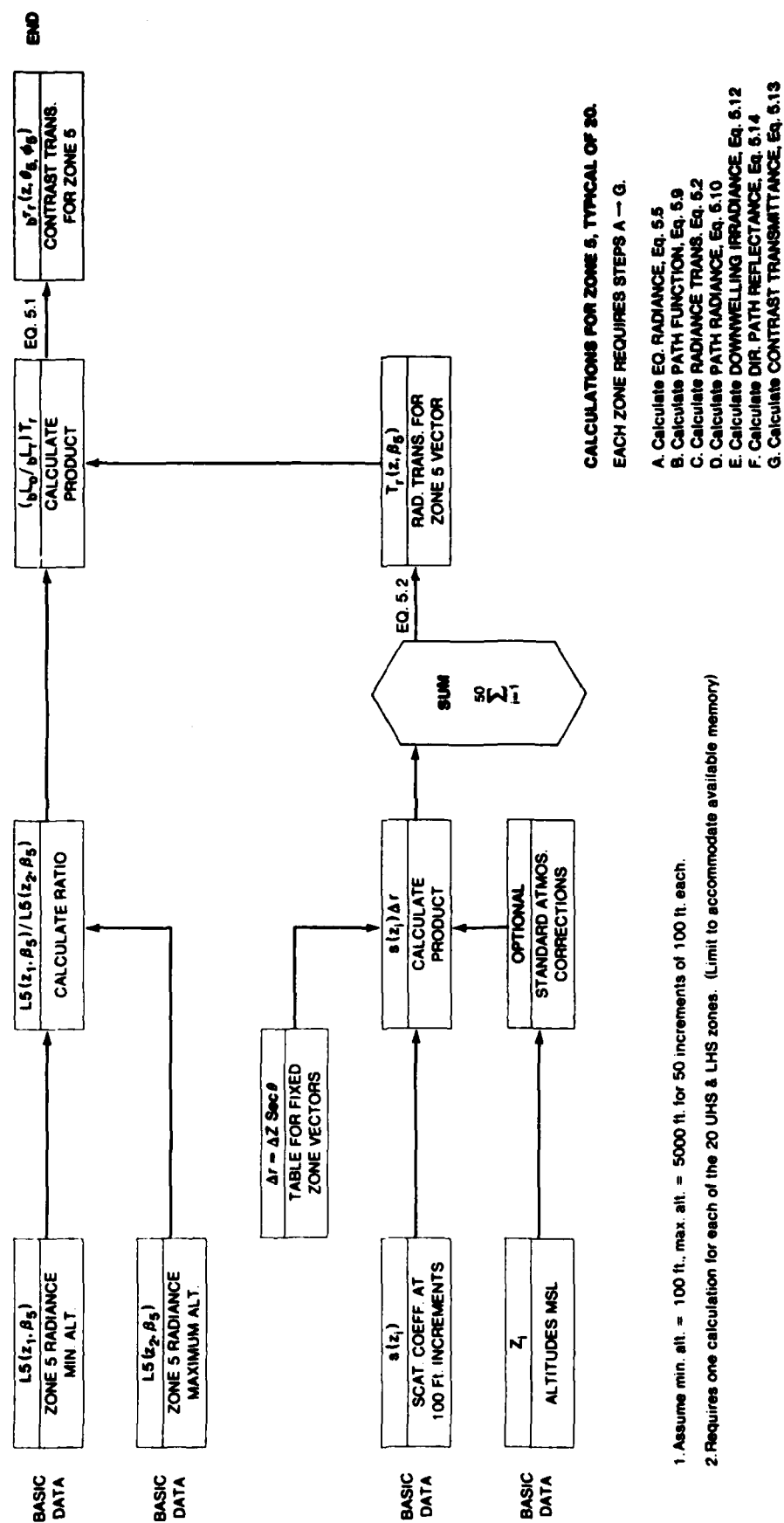


Fig. 5-4. Ratio method.

A correction factor of the form $\left[\sum \frac{\sigma(z, \theta)}{s(z)} \Delta \Omega \right]^{-1}$ should be applied multiplicatively to Eq. (5.5) to compensate somewhat for the loss of directionality induced by using the central β for the entire $\Delta \Omega$ of each zone. The use of this factor decreases the maximum precision error in the summation from nineteen percent to only six percent.

In Eqs. (5.4) and (5.5), β is the angle between the sun and the path of sight, and $L(z, \theta', \phi')$ is the apparent radiance of the sky or ground for direction θ' and ϕ' . The ratio $\sigma(z, \beta')/s(z)$ is the proportional directional volume scattering function at angle β' and altitude z . The β' is the angle between the path of sight at θ, ϕ , and the radiance θ', ϕ' . It is found by

$$\cos \beta' = \sin \theta \sin \phi \sin \theta' \sin \phi' + \sin \theta \cos \phi \sin \theta' \cos \phi' + \cos \theta \cos \theta' \quad (5.6)$$

which may be simplified to

$$\cos \beta' = \sin \theta \sin \theta' \cos(\phi - \phi') + \cos \theta \cos \theta' \quad (5.7)$$

Our initial design should provide for calculation of $L_q(z, \theta, \phi)$ at both maximum and minimum altitude, with intermediate interpolations at $\Delta z = 100$ ft. A value for equilibrium radiance is required for each path of sight for which a contrast transmittance value will be calculated. *i.e.* one for each zone (using the proposed configuration, a total of 20, eleven upward and nine downward). It is the use of a specific value of normalized phase function for each zones designated path of sight (*i.e.* through its optical centroid) that provides the superior directional fidelity inherent in this methods determinations of contrast transmittance.

Path Function

Image-forming light is lost by scattering and absorption in each elementary segment of the path of sight, and contrast-reducing path radiance is generated by the scattering of the ambient light which reaches the segment from all directions. The quantitative description of this scattered component of path-segment radiance involves a quantity called the "path function," $L_p(z, \theta, \phi)$. The "path function" depends upon the directional distribution of the lighting on the segment due to its surroundings. It can be operationally defined in terms of the (limiting) ratio of the path radiance associated with a short path of the path length by the relation

$$L_p(z, \theta, \phi) = \lim(\Delta r \rightarrow 0) L_{\Delta r}^*(z, \theta, \phi) / \Delta r \quad (5.8)$$

In experimental practice, the path length Δr should be sufficiently short so that no change in the ratio can be detected if Δr is made shorter. In this new device, we are assuming that a 100 foot incremental length is adequately short. In lieu of a direct measurement of path function, it may be derived from related quantities. Path function is expressed as a function of the total volume scattering

coefficient and the equilibrium radiance in Eq. (5.9), which is the form to be used in the on-board computation.

$$L_p(z_i, \theta, \phi) = L_q(z_i, \theta, \phi) s(z_i) \quad (5.9)$$

The next step is to compute the path radiance along each desired path of sight.

Path Radiance

Path radiance $L_p^*(z, \theta, \phi)$ for the path of sight θ is the integration or summation of the path function $L_p(z, \theta, \phi)$ weighted by the radiance transmittance $T_r(z, \theta)$. Path length r_i is from the incremental path Δr to the sensor at z :

$$L_p^*(z, \theta, \phi) = \sum_{i=1}^m L_p(z_i, \theta, \phi) T_r(z, \theta) \Delta r \quad (5.10)$$

At this point, one has computed for each of the 20 desired paths of sight, (fewer if memory becomes a problem), both the path radiance $L_p^*(z, \theta, \phi)$ and the radiance transmittance $T_r(z, \theta)$. These, plus the downwelling and upwelling irradiances, are the essential atmospheric properties. The irradiances can be measured with an auxiliary irradiator channel, or calculated from the fisheye scanner data using an equation similar in form to Eqs. (5.4) and (5.5).

Downwelling and Upwelling Irradiance

In the traditional calculations, the downwelling irradiance used to compute the directional path reflectance $R_p^*(z, \theta, \phi)$ and the apparent terrain reflectance is computed from data at the lowest altitude of flight by the equation

$$E(z, d) = \epsilon(z) \cos \theta_s + \int_{\pi} L(z, \theta', \phi') \cos \theta' d\Omega \quad (5.11)$$

where $\epsilon(z)$ is the sun scalar irradiance at altitude z , θ_s is the sun zenith angle, and $L(z, \theta', \phi')$ is the sky radiance at direction θ', ϕ' . However, in the Summation Method, the average zone radiance technique is substituted using Eq. (5.12)

$$E(z, d) = \sum_{\pi} \epsilon L_1(z, \theta_1, \phi_1) \cos \theta_1 \Delta \Omega + L_2(z, \theta_2, \phi_2) \cos \theta_2 \Delta \Omega + \dots + L_{11}(z, \theta_{11}, \phi_{11}) \cos \theta_{11} \Delta \Omega \quad (5.12)$$

The upwelling irradiance $E(z, u)$ is computed using Eq. (5.12) and the zone radiances from the nine lower hemisphere zones. The upwelling irradiance is used to obtain R^* for the upward paths of sight, and in the event one chooses to use the average terrain reflectance as the background reflectance in the contrast transmittance calculation as will be discussed in the following paragraphs. As with Eq. (5.5), there is a correction factor of similar form that should be used with Eq. (5.12). This factor, $[\pi / \sum \cos \theta \Delta \Omega]$ will reduce the anticipated precision error from a maximum of seventeen percent to only ten percent.

With the computations for irradiance completed, one now has all of the atmospheric components necessary to calculate the directional path reflectance $R_r^*(z, \theta, \phi)$ and thence contrast transmittance.

Contrast Transmittance

The concept of directional path reflectance is utilized in Eq. (5.13) to define contrast transmittance in the form proposed for this new in-flight system.

$$T_r(z, \theta, \phi) = [1 + R_r^*(z, \theta, \phi) / {}_bR_o(z, \theta, \phi)]^{-1}, \quad (5.13)$$

where ${}_bR_o(z, \theta, \phi)$ is the directional background reflectance. By definition, the directional path reflectance is

$$R_r^*(z, \theta, \phi) = \pi L_r^*(z, \theta, \phi) / [E(z, d) T_r(z, \theta)]. \quad (5.14)$$

where $E(z, d)$ is the downwelling irradiance. Note that for upward paths of sight, the upwelling irradiance $E(z, u)$ is used in Eq. (5.14). We have chosen to develop the atmospheric data in the form of directional path reflectance since, in this form, it can be easily utilized with the directional reflectance of a variety of backgrounds smaller in extent but different from the heterogeneous background which contributed to the path radiance and downwelling irradiance. In the event that no reliable value for the directional background reflectance ${}_bR_o(z, \theta, \phi)$ is available, then one may choose one of the upper or lower hemisphere zone radiances and compute an approximation using Eq. (5.15).

Background Reflectance

The inherent background reflectance is defined as

$${}_bR_o(z, \theta, \phi) = \pi {}_bL_o(z, \theta, \phi) / E(z, d), \quad (5.15)$$

where $E(z, d)$ is the downwelling irradiance at the target altitude. Again on notes that for upward paths of sight, the upwelling irradiance is used in Eq. (5.15). The inherent background reflectance may be obtained from either (1) a measurement by a ground-based telephotometer, (2) measurements by an airborne telephotometer, or (3) an educated estimate.

Thus, the contrast transmittance along any of the twenty paths of sight defined by the upper and lower hemisphere zones may be determined via Eq. (5.13), and the two reflectance terms defined by Eqs. (5.14) and (5.15). A computational flowchart similar to Fig. 5-4 which outlined the Ratio Method, is shown in Fig. 5-5 for the Summation Method.

6. SYSTEM REVIEW

A simple, yet relatively smart electro-optical system has been devised to do real-time monitoring of the optical state of the atmosphere. The system concept has been built around three solid state, no moving parts, transducer assemblies interfaced with a small dedicated microprocessor that can control the system in either a semi-automatic,

or an operator interactive mode. This concept has resulted in the development of a multiple purpose system, capable of jointly supporting tactical commanders, meteorological forecasters, and researchers involved in studies of multi-spectral atmospheric contrast transmittance. The device, while primarily intended for airborne application within the lower troposphere, is easily adaptable for static ground based applications in the determination of near surface optical properties. Thus, it can be equally useful in providing relatively inexpensive flight data appropriate for the validation of new or improved modelling techniques, as well as providing the means for significantly shortening the necessary predictive window required for the meteorological support of time-critical field operations.

The development status is such that each of the system sub-assemblies has been evaluated in an operational mock-up configuration, and has performed adequately to indicate technical feasibility.

A new compact, multi-channel nephelometer has been developed which retains many of the features of the larger C-130 mounted version reported by Johnson (1981a), but which requires only a few hundred watts of input power, and is less than one meter in length overall. The nephelometer mock-up, operating in pulsed mode has measured the scattering characteristics of clear day room air, as shown in Fig. 3-13, with adequate sensitivity to suggest the capability of measurements approaching $10^{-5} m^{-1}$ i.e. sea level molecular. If the mock-up performances turn out to be reliable at this level, then a follow on effort to assure these performances is an attractive option. Automatic gain control circuitry to inhibit detector saturation and thus permit measurements in highly scattering media, i.e. clouds or fogs, is also an attractive design add-on that seems well within reason, and is recommended for further development.

The staring fisheye scanner has also performed well in its mock-up configuration. The sky and sun zone average radiances as measured under several different meteorological conditions are well placed on the system's flux-voltage curve as illustrated in Fig. 4-6. Thus, the use of this discrete detector system should proceed to full brass board configuration with little difficulty. As discussed in sections four and five however, the influence of the direct solar component upon equilibrium radiance is strong under clear or light haze conditions, and thus continuing analytic studies are recommended to optimize the selection of the sun zone diffuser pattern. In this context, the follow-on development of the scanning array detector system mentioned in Section 3 should be re-evaluated as a second generation device. The non-blooming, time integration characteristics of this type device, coupled with its 256x256 array of individually scannable detectors would provide an efficient, software controlled mechanism for adjusting the sky and sun zones directly without the need for manipulating the diffuser plate, which could be completely eliminated.

The in-flight computer system requirements have been evaluated as discussed in Section 5, and additional circuit mock-ups are in progress. Sub-assembly selections

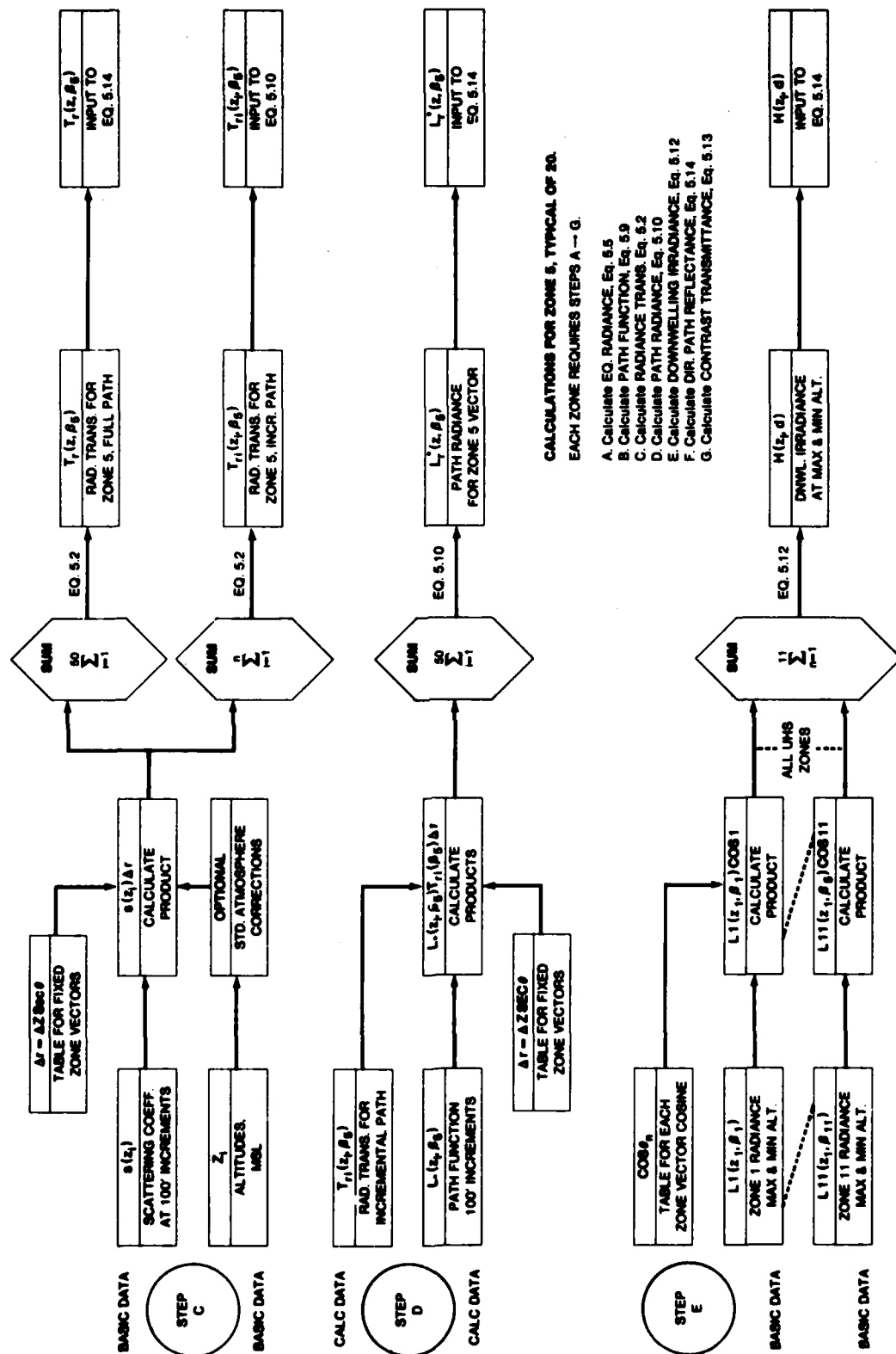
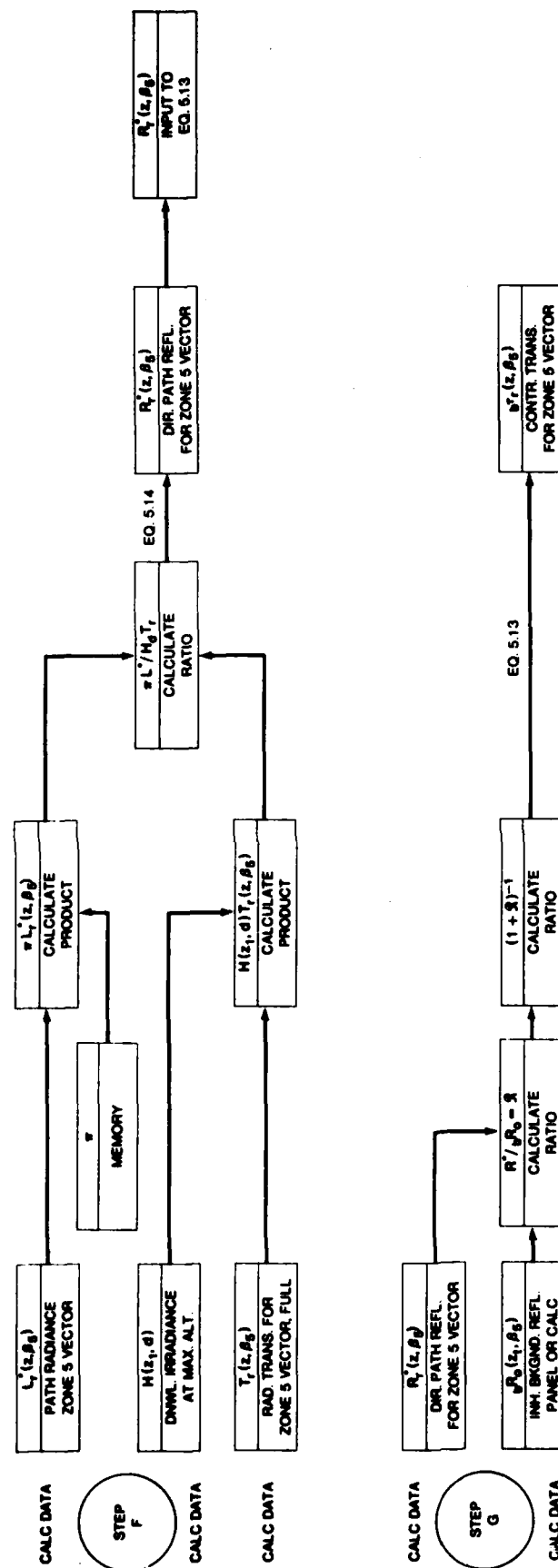


Fig. 5-5b. Summation method.



CALCULATIONS FOR ZONE S, TYPICAL OF 20.
EACH ZONE REQUIRES STEPS A - G.

- A. Calculate EQ. RADIANCE, Eq. 5.5
- B. Calculate PATH FUNCTION, Eq. 5.9
- C. Calculate RADIANCE TRANS, Eq. 5.2
- D. Calculate PATH RADIANCE, Eq. 5.10
- E. Calculate DOWNWELLING IRRADIANCE, Eq. 5.12
- F. Calculate DIR. PATH REFLECTANCE, Eq. 5.14
- G. Calculate CONTRAST TRANSMITTANCE, Eq. 5.13

NOTE:
The angular relationships between the sun direction vector, θ_s, ϕ_s , and the twenty pre-determined path of sight direction vectors, θ_i, ϕ_i , are fixed for the three typical sun elevations defined by the scanner zone plate. Thus the β_i values assigned to Eq. 5.5 are also fixed in three sets of 20 each, one set for each nominal sun elevation, low, medium or high.
 β_1, β_2 , etc is a shorthand notation used to identify each zone's direction vector, and is not necessarily the scattering angle referred to with respect to phase functions.

Fig. 5-5c. Summation method.

have been made based upon the transducer performances illustrated in Sections 3 and 4 in concert with the computational requirements discussed in Section 5. The pulse integration and multiplexing circuitry has been used in the evaluation of the nephelometer performance, and found to be satisfactory. Breadboarding of these circuits within the context of the flow chart illustrated in Fig. 5-1 is underway with the immediate goal of adequate completion to illustrate full system mock-up performances.

7. ACKNOWLEDGEMENTS

The development of this system concept has been built upon the long term experimental program of airborne measurements of optical atmospheric properties conducted by the Visibility Laboratory staff under the sponsorship of the Optical Physics branch of the Air Force Geophysics Laboratory.

The technical design and engineering mock-ups have been provided by Mr. R.L. Ensminger and G.F. Simas of the Visibility Laboratory's electronic design group, and by Mr. T.J. Petzold, the Laboratory's optical design specialist. Ms. J.I. Gordon provided much of the analytic support in developing the techniques for evaluation of the sun and sky zone selections.

8. REFERENCES

- Barteneva, O. D., "Scattering Functions of Light in the Atmospheric Boundary Layer," *Bull. Acad. Sci., U.S.S.R. Geophysics Series*, 1237-1244 (1960).
- Beuttell, R.G., and A.W. Brewer, "Instruments for Measurements of Visual Range", *J. Scient. Instrum.* 26, 357-359 (1949).
- Charlson, R.J., H. Horvath, and P.F. Pueschel, "The Direct Measurement of Atmospheric Light Scattering Coefficient for Studies of Visibility and Pollution", *Atmospheric Environment* 1, 469-478 (1967).
- Crosby, P., and B.W. Koerber, "Scattering of Light in the Lower Atmosphere", *J. Opt. Soc. Am.* 53 358-361 (1963).
- Deirmendjian, D., *Electromagnetic Scattering on Spherical Polydispersions*, (Elsevier, New York, 1969).
- Duntley, S.Q., A.R. Boileau, and R. Preisendorfer, "Image Transmission by the Troposphere I", *J. Opt. Soc. Am.* 47, 499-506 (1957).
- Duntley, S.Q., R.W. Johnson, J.I. Gordon, and A.R. Boileau, "Airborne Measurements of Optical Atmospheric Properties at Night", University of California, San Diego, Scripps Institution of Oceanography, Visibility Laboratory, SIO Ref. 70-7, AFGL-70-0137, NTIS No. AD 870 734 (1970).
- Duntley, S.Q., R.W. Johnson, and J.I. Gordon, "Airborne Measurements of Optical Atmospheric Properties in Northern Germany", University of California, San Diego, Scripps Institution of Oceanography, Visibility Laboratory, SIO Ref. 76-17, AFGL-TR-76-0188, NTIS No. ADA 035 571 (1976).
- Duntley, S.Q., R.W. Johnson, and J.I. Gordon, "Airborne Measurements of Optical Atmospheric Properties, Summary and Review III", University of California, San Diego, Scripps Institution of Oceanography, Visibility Laboratory, SIO Ref. 79-5, AFGL-TR-78-0286, NTIS No. ADA 073 121 (1978).
- Ensor, D.S., and A.P. Waggoner, "Angular Truncation Error in the Integrating Nephelometer", *Atmospheric Environment* 4, 481-487 (1970).
- Fitzgerald, J.W., "Angular Truncation Error of the Integrating Nephelometer in the Fog Droplet Size Range", *J. Appl. Met.* 16, 198-204 (1977).
- Gordon, J.I., "Model for a Clear Atmosphere", *J. Opt. Soc. Am.* 59, 14-18 (1969).
- Hering, W.S., H.S. Muench, and H.A. Brown, "Field Test of a Forward Scatter Visibility Meter", Air Force Cambridge Research Laboratories, Hanscom Field, Bedford, Mass., AFGL-71-0315 (1971).
- Hering, W.S., "An Operational Technique for Estimating Visible Spectrum Contrast Transmittance", University of California, San Diego, Scripps Institution of Oceanography, Visibility Laboratory, SIO Ref. 82-1, AFGL-TR-81-0198 (1981).
- Horvath, H., and K.E. Noll, "The Relationship Between Atmospheric Light Scattering Coefficient and Visibility", *Atmospheric Environment* 3, 543-550 (1969).
- Johnson, R.W., and J.I. Gordon, "Airborne Measurements of Atmospheric Volume Scattering Coefficients in Northern Europe, Summer 1978", University of California, San Diego, Scripps Institution of Oceanography, Visibility Laboratory, SIO Ref. 80-20, AFGL-TR-80-0207, NTIS No. ADA 097 134 (1980).
- Johnson, R.W., "Airborne Measurements of European Sky and Terrain Radiances", University of California, San Diego, Scripps Institution of Oceanography, Visibility Laboratory, SIO Ref. 82-2, AFGL-TR-81-0275 (1981b).
- Johnson, R.W., and B.W. Fitch, "A Review of Measured Atmospheric Optical Properties and Their Contemporary Aerosol Size Distributions", University of California, San Diego, Scripps Institution of Oceanography, Visibility Laboratory, SIO Ref. 82-22, AFGL-TR-82-0049 (1981).
- Johnson, R.W., and W.S. Hering, "An Analysis of Natural Variations in Measured European Sky and Terrain Radiances", University of California, San Diego, Scripps Institution of Oceanography, Visibility Laboratory, SIO Ref. 82-6, AFGL-TR-81-0317 (1981).
- Johnson, R.W., "Daytime Visibility and Nephelometer Measurements Related to its Determination", *Atmospheric Environment*, 15, 10/11, 1835 (1981a).
- Johnson, R.W., and W.S. Hering, "Measurements of Optical Atmospheric Quantities in Europe and Their Application to Modelling Visible Spectrum Contrast Transmittance", in *Proc. of the AGARD 29th Symposium of the Electromagnetic Wave Propagation Panel on Special Topics in Optical Propagation*, AGARD-CP-300, pp. 14-1 to 14-12 (1981).
- Rabinoff, R.A., and B.M. Herman, "Effect of Aerosol Size Distribution on the Accuracy of the Integrating Nephelometer", *J. Appl. Met.* 12, 184-186 (1973).

Sub-Assembly Specification Sheets

- A1: Illumination Industries Inc., Type X75-2002
- A2: EG&G, model FX-201
- A3: EG&G, model FX-132
- A4: EG&G, model HUV-4000B
- A5: EG&G, model HUV-1000B
- A6: Silicon Detector Corp., model SCD-444-42-12-261
- A7: United Detector Technology, model PIN 10AP
- A8: Traid Corp., model 735 Periphoto
- A9: Allied Impex Corp., Soligor Fisheye Adapter
- A10: Smoke Signal Broadcasting, Chieftain Microcomputers
- A11: Memodyne Corporation, Intelligent Cassette Recorders

Note: The selection and use of the components listed above does not imply endorsement or recommendation of the tested products by the Visibility Laboratory or its sponsors to the exclusion of other products that may be suitable.

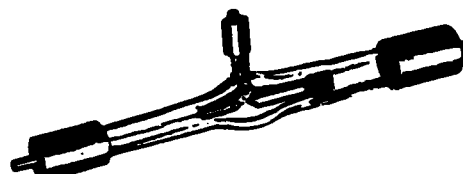
APPENDIX A-1

ILLUMINATION INDUSTRIES, INC.

TECHNICAL DATA



XENON SHORT ARC LAMPS



Operating Characteristics of Xenon Arc Lamps

CHARACTERISTICS	LAMP TYPE					UNITS
	X-35 X-36	X-75 X-76	X-150S X-150L**	X-300	X-500***	
With/Without Starting Electrode	Without With	Without With	Without	Without	Without	
Type of Current	DC	DC	DC	DC	DC	
Lamp Operating Voltage	12±2	14±2	20±3	18 ⁺² ₋₃	20±2	volts
Lamp Operating Current for Above Voltage Range	2.5-3.5	4.6-6.2	6.5-8.8	15-20	14-30	amps
Lamp Rated Power — DC Operation	35	75	150	300	500	watts
Starting Pulse Amplitude (min.)	15 10	15	20	20	30	kilovolts
Arc Size (inches) HT x Width	0.012x0.012	.020x.015	.080x.050	.070x.080	.120x.060	inches
Luminous Flux (lumens)	315	1,125	3,200	6,300	15,000	lumens
Luminous Efficiency	9	15	21	21	30	lumens/watt
Average Brightness	40,000	80,000	30,000	35,000	35,000	candela/cm ²
Average Life	200	300	1,000	1,000	1,200	hours
Operating Position	Vertical Anode Up*	Vertical Anode Up*	Vertical* ±30°	Vertical* ±30°	Vertical* ±30°	
Housing Size — Minimum Side Wall Surface Area	30	60	130	200	400	in. ²
Cooling	Convection	Convection	Convection	Forced Air	Forced Air	
Base Style	Sleeve	Sleeve	Sleeve with Knurled Nut	Sleeve with Knurled Nut	Sleeve	

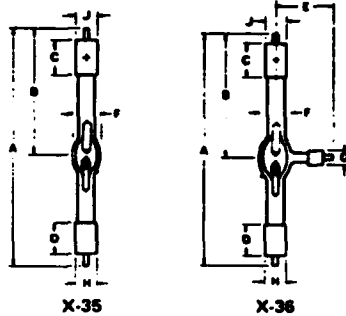
*The X-75 and X-35 are two electrode lamps and the X-36 and X-76 have three electrodes. This third electrode may be used as a starting electrode. These lamps may be operated with the anode (+ terminal) in any position above the horizontal.

**The standard 150L sleeve base has a metric thread of 4mm diameter and 0.7mm pitch. The 150S has a plain sleeve base.

***X-500 Special order only

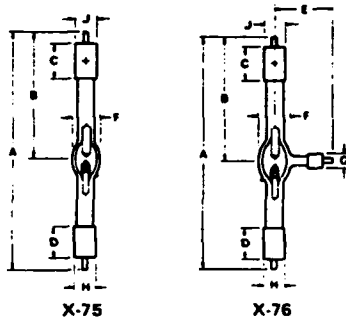
ILLUMINATION INDUSTRIES, INC. • 825 E. EVELYN AVE., SUNNYVALE, CALIFORNIA 94086 • PHONE: 408/245-4111 • TWX: 910-339-9214

PER BRAND PRODUCTS

**35 WATT XENON SHORT ARC LAMPS**

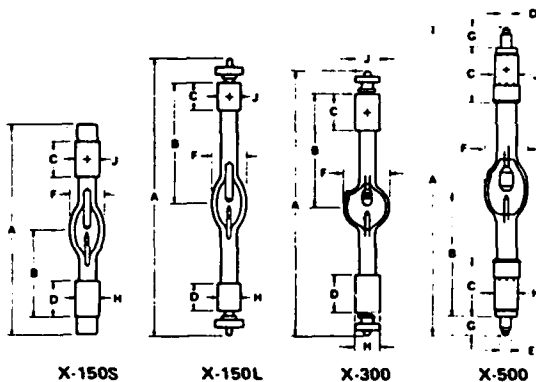
Physical Dimensions (in inches)

LAMP	A	B	C	D	E	F	G	H	J
X-35	3.375	1.562	.450	.450		.375		.295	.295
X-36	3.375	1.562	.450	.450	.750	.375	.185	.295	.295

**75 WATT XENON SHORT ARC LAMPS**

Physical Dimensions (in inches)

LAMP	A	B	C	D	E	F	G	H	J
X-75	3.500	1.700	.500	.450		.500		.295	.350
X-76	3.500	1.700	.500	.450	.750	.500	.185	.295	.350

**150, 300 AND 500 WATT XENON SHORT ARC LAMPS**

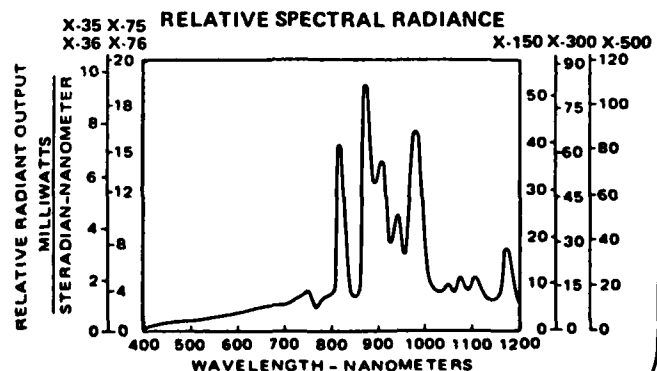
Physical Dimensions (in inches)

LAMP	A	B	C	D	E	F	G	H	J
X-150S	4.500	1.875	.750	.750		.730		.500	.500
X-150L	5.937	2.562	.591	.591		.750		.473	.473
X-300	5.750	2.437	.813	.813		.937		.500	.500
X-500	10.20	3.750	2.00	.312	.390	1.17	1.00	.750	.750

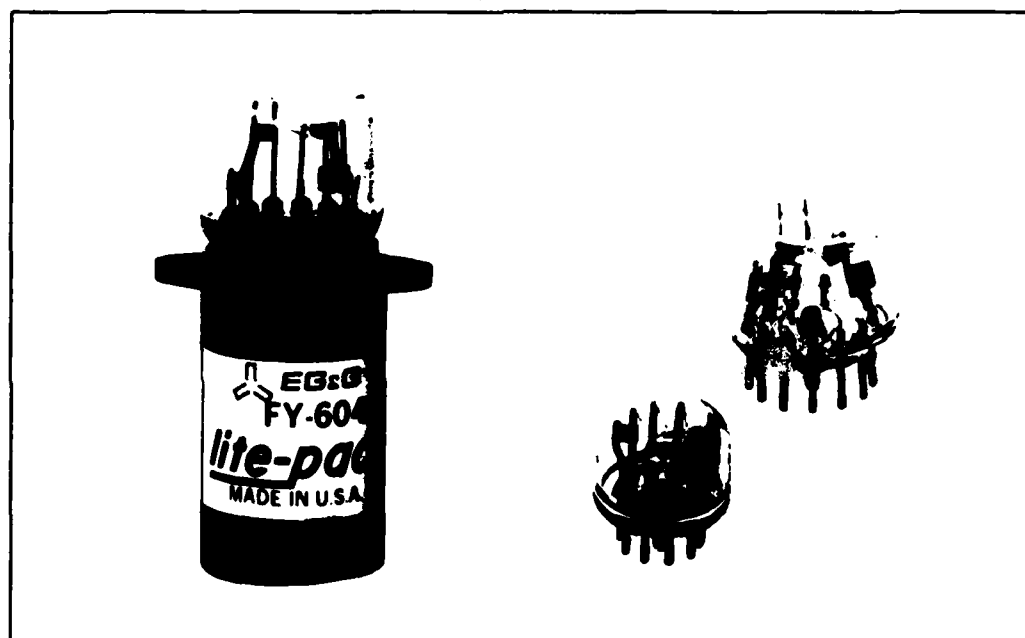
CAUTION:

These lamps are under positive pressure of several atmospheres during non-operating conditions. During operation, the internal pressure will increase considerably and adequate eye protection should be worn when handling them. Before operating the lamps, clean the bulb surface of all foreign matter including fingerprints. For maximum life, the base temperatures should be held to 200°C.

Further information about these lamps or their power supply requirements may be obtained by contacting Illumination Industries, Inc.



High Efficiency Bulb Type Xenon Flashtubes and Lite-Pac[™] Trigger Modules



Tube Description

The high efficiency bulb type xenon flashtubes are a second generation device which produce twice the light output of the standard bulb type flashtube. These lamps are unique devices designed to generate short flash durations of high radiance. Capable of high repetition rates, the bulb type xenon flashtubes have precise arc discharge patterns which are stable and non-wandering. These probe stabilized flashtubes are used in a wide variety of applications where long life is important.

Lite-Pac Description

The EG&G Lite-Pac[®] Trigger Modules provide the high voltage trigger pulses required to operate the bulb type xenon flashtubes. As the "socket" for a bulb type flashtube, the Lite-Pac[®] contains a high voltage trigger transformer and coupling components encapsulated for long life operation. The FY-500 series is used with the 9 pin family of flashtubes and the FY-600 series is used with the 12 pin family. A typical driver circuit is shown on the back page of this data sheet.

Electrical Data

	FX-280	FX-198	FX-199	FX-279	FX-200	FX-201
Arc Discharge Length (inches) (mm)	0.060(1.5)	0.125 (3)	0.315 (8)	0.060(1.5)	0.125 (3)	0.315 (8)
Max. Energy Per Flash (joules) ¹	5	5	5	15	15	15
Max. Average Power (watts) ²	10	10	10	15	15	15
Max. Operating Voltage (Vdc)	1500	1500	1500	1500	1500	1500
Min. Operating Voltage (Vdc) ³	300	300	300	300	300	300
Lite-Pac [®] Type	FY-507	FY-506	FY-505	FY-611	FY-604	FY-602

¹ Joules = $\frac{1}{2} CV^2$.

² Watts = $\frac{1}{2} CV^2 \times \text{repetition rate}$.

³ Using recommended driver circuits (see back page).

Performance Information

FLASH DURATIONS, measured at $\frac{1}{3}$ of peak amplitude, vary from less than a microsecond to 15 microseconds and are dependent upon the discharge capacitor value and any additional discharge circuit impedance.

TIME JITTER is typically less than 200 nanoseconds and light output amplitude variation less than 10 percent.

RECOVERY TIME or the elapsed time between flash and the reapplication of voltage across the tube depends on the energy discharged and the rate of rise of applied voltage. Typically flashtubes are completely recovered after a delay of 150 microseconds, although in many cases the voltage may be reapplied immediately if the initial rate-of-rise of voltage is less than 1 volt per microsecond.

REPETITION RATES in excess of 1000 pps are possible. Discharge circuit design will greatly influence the maximum repetition rate possible.

LIGHT OUTPUT and pulse duration are optimized by keeping the discharge circuit impedance as low as possible. Lite-Pac[®] leads as a part of the discharge loop should be no longer than necessary to minimize circuit impedance.

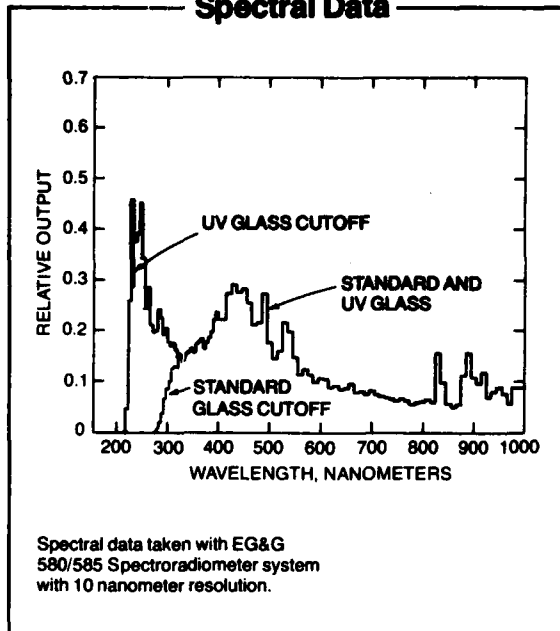
EFFICIENCY can be as high as 20 percent and is dependent upon input energy. Generally, the highest efficiencies are obtained when the input energy is in the 0.1 to 1.0 joule range. Correlated color temperatures are typically blue rich in excess of 15,000° K.



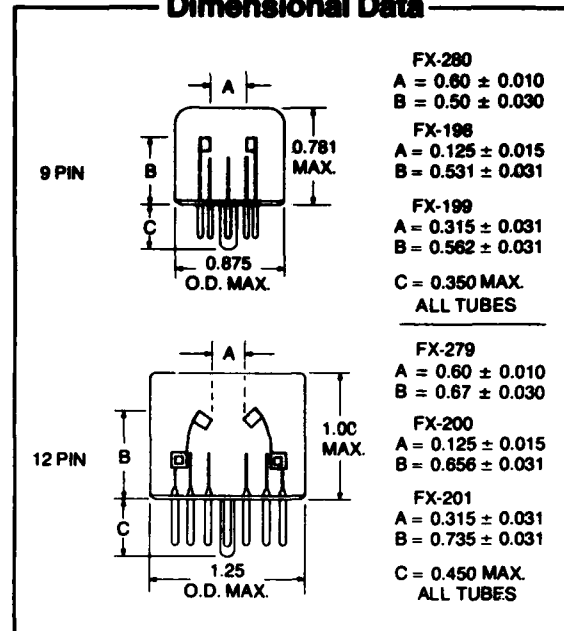
[®] Registered EG&G Trademark

APPENDIX A-2

Spectral Data



Dimensional Data

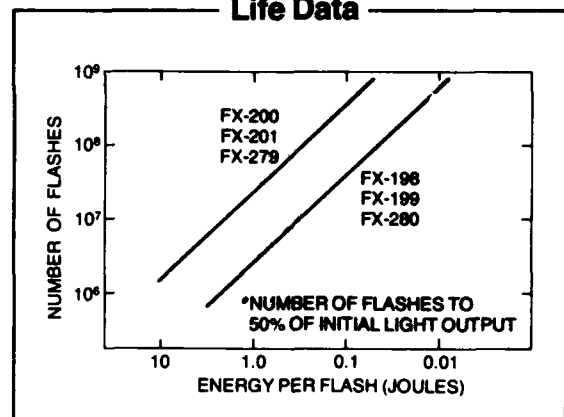


Light Output Distribution

Wavelength Intervals (nanometers)	Percentage	
	Standard Bulb	UV Bulb
200- 300	—	18
300- 400	11	14
400- 500	28	22
500- 600	15	12
600- 700	12	7
700- 800	9	6
800- 900	11	8
900-1000	8	7
1000-1100	6	6

*Standard Bulb (Standard Glass)

Life Data

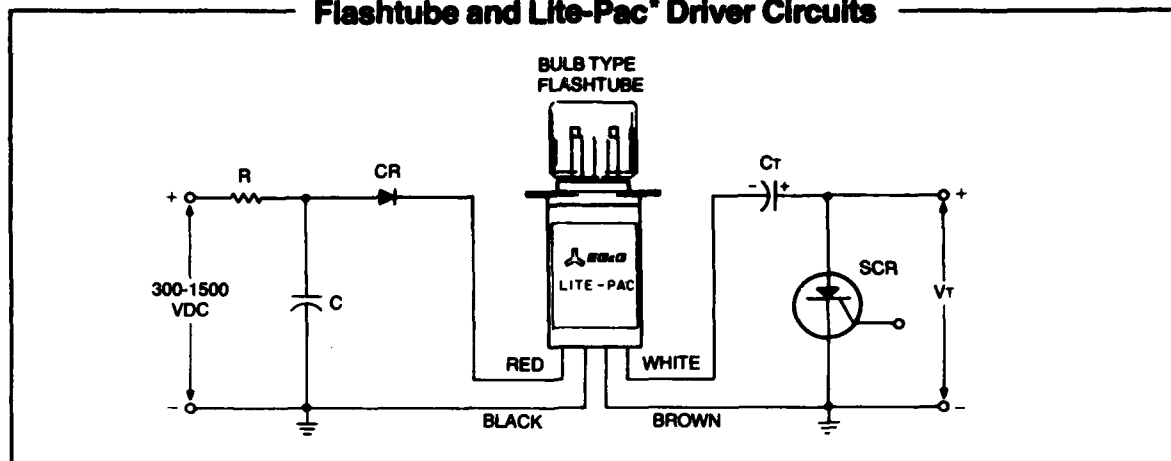


General Information

1. The bulb type flashtube may be purchased with a UV transmitting envelope which will extend the light output into the UV region as shown on the spectral data curve. Add the suffix "U" to the tube type number (FX-198U) to obtain this characteristic.
2. Bulb type flashtubes with light output below 220 nanometers are available upon request.
3. Bulb type flashtubes with arc lengths other than shown between 1.5 and 8.0 millimeters are available upon request.

ELECTRO-OPTICS

Flashtube and Lite-Pac[®] Driver Circuits



Discharge Circuit

- CR = Diode with 3 kilovolt peak inverse voltage, 3 amp rating such as EG&G Stock Number 83-0276 or three diodes in series, each with a 1 kVPIV, 3 amp rating.
- R, C = Values determined by light output, operating characteristics desired and flashtube ratings. R is typically between 10K and 200K ohms, C is determined by energy = $\frac{1}{2} CV^2$.

Trigger Circuit

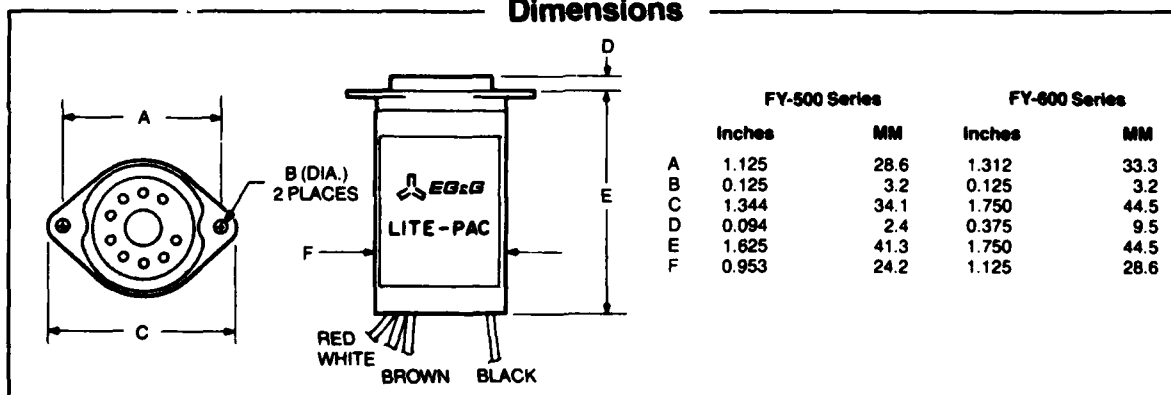
VT
CT
SCR

Low Voltage	High Voltage
50 Vdc	200 Vdc
1.0 mfd	0.1 mfd
RCA 2N4102 or S2400 Series (200 amps/ μ sec, 600 Vdc)	

Notes

- It is suggested that CR be used in the discharge circuit as this diode will enhance operation at lower anode voltages, at higher rep rates and will also improve time jitter characteristics. The user has a choice of either low voltage or high voltage trigger circuit operation. The high voltage trigger circuit generally improves the time jitter characteristics and light output stability.
- Lite-Pac[®] leads are a minimum of 12 inches in length and are stripped and tinned. The anode (red) and cathode (black) leads are AWG 20 U.L. Style 3271 or equivalent. The trigger leads (brown and white) are AWG 22 U.L. Style 3265 or equivalent. Do not bend leads sharply at the exit. Allow a small clearance bend radius.
- The dielectric withstanding voltage between the black and brown leads is 1500 volts maximum.
- Since the discharge impedance of the bulb type flashtube is low, it is suggested the leads between the discharge capacitor and the Lite-Pac[®] be kept as short as possible to optimize light output and to keep the light pulse duration to a minimum.
- Twist together and dress trigger leads separately from red and black leads.

Dimensions

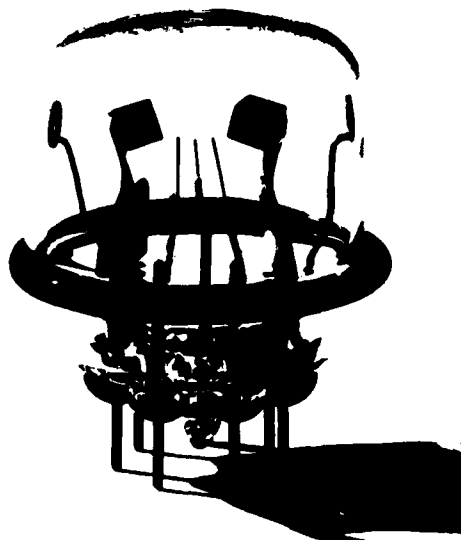


35 CONGRESS STREET SALEM, MASS. 01970
TEL: (617) 745-3200 TWX: 710-347-6741

Printed in U.S.A. 4/81



FX-132 BULB TYPE XENON FLASHTUBE



The FX-132 is the largest design in a series of stable arc, bulb-type flashtubes manufactured exclusively by EG&G. These tubes are fabricated on multi-pin presses and are conveniently inserted into a standard 7-pin, E7-2 socket thus assuring proper alignment.

The FX-132 is designed to have the high radiance of the smaller bulb-type tubes (Ref. Data Sheet No. F1005D-3) and, at the same time, exhibit the high intensity and high average power usually only achieved with linear flashtubes (Ref. Data Sheet No. F1002C-2). These features make the FX-132 an optimal source for high throughput optical condensing systems having entrance pupils ranging from 1 to 15 mm in diameter, such as Fresnel lens systems and Fiber-optic bundles.

FEATURES

- LONG LIFE – 10^9 FLASHES
- HIGH ENERGY – UP TO 200 JOULES/FLASH
- HIGH AVERAGE POWER – UP TO 100 WATTS
- SPATIALLY STABLE ARC
- LOW VOLTAGE OPERATION

APPLICATIONS

- MICROFICHE EXPOSURE
- MICROFICHE REPRODUCTION
- HIGH ENERGY STROBOSCOPES
- NONIMPACT PRINTING
- PHOTOMASK PRODUCTION
- VISUAL BEACONS
- COMPUTER PRINTER
- PHOTORESIST EXPOSURE

The lamp is uniquely suitable for applications such as the production of hard 8-1/2" by 11" copy from microfilm. In addition, the short pulse duration of the flash allows a stroboscopic exposure which will form a stationary non-blurring image on a moving platen.

The high average power capability of the FX-132 makes it uniquely suited for applications involving moderate discharge energies at fast repetition rates. These applications include high intensity projecting stroboscopes, step and repeat photomask production and non-impact printing.

MAXIMUM RATINGS

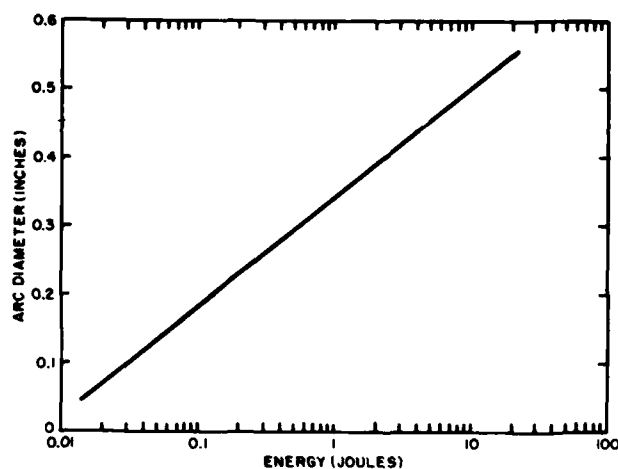
Maximum Energy Per Flash (Joules)	200
Maximum Long-Term Average Power (Watts)	100
Maximum Repetition Rate (pps)	500
Minimum Operating Voltage (Vdc)	200
Maximum Operating Voltage (Vdc)	1500
Trigger Voltage	10KV [†]

[†]10KV (min) peak amplitude pulse, with 1.5 μ s rise time and 1.5 μ s pulse width. Use EG&G TR-1647 Trigger Transformer or EG&G FY-7 Lite Pac.*

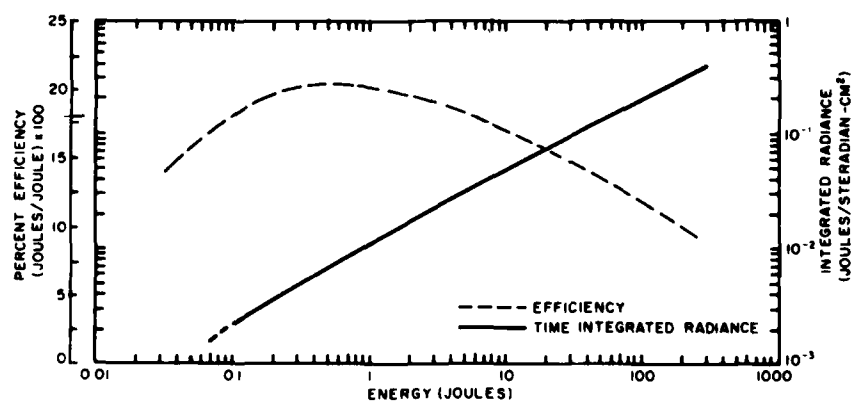
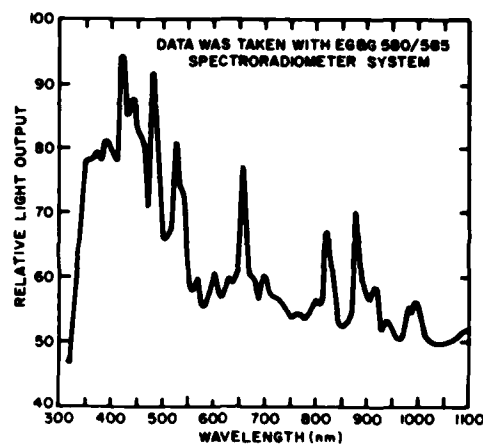
TYPICAL OPERATING CONDITIONS

	A	B	C
Energy Input (Joules)	0.01	5	80
Voltage (Vdc)	650	1000	200
Capacitance (μ s)	0.047	10	4000
Peak Current (a)	100	2400	6000
Pulse Duration at 1/3 Peak (μ s)	1	10	330
Repetition Rate (pps)	420	25	1
Life (Number of Flashes)	2×10^9	1×10^8	2×10^6

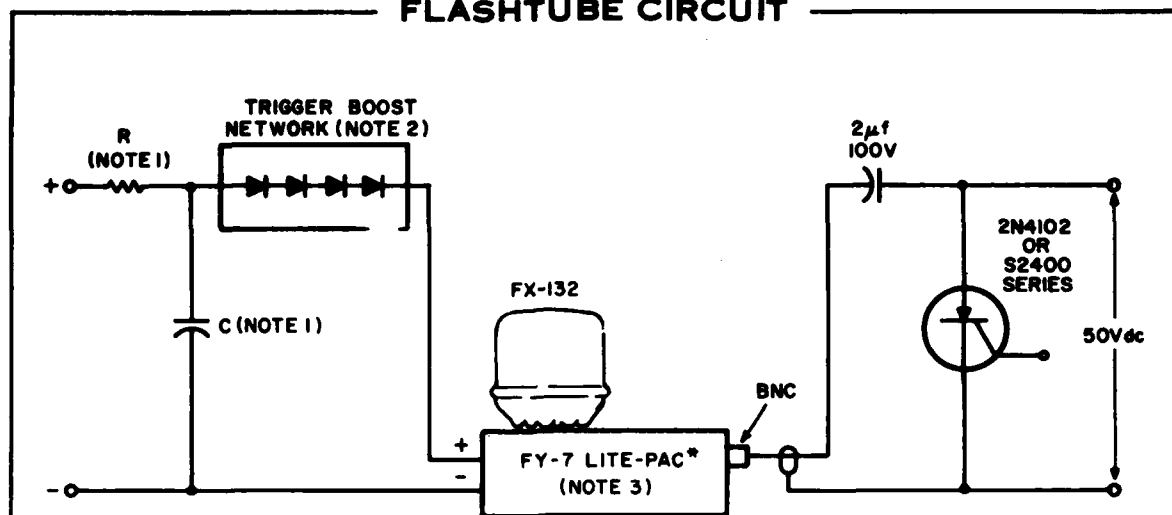
ARC DIAMETER VS. INPUT ENERGY



SPECTRAL DATA



FLASHTUBE CIRCUIT



NOTES

1. Charging resistor, R, is typically between 10K and 100K ohms. An inductor may be used with R to limit the charging time of the voltage applied to the FX-132. Inductor values may be between 0.5 to 10 hy. Light output and maximum energy input are determined by: $\text{Joules} = 1/2 C V^2$.
2. The trigger boost network consists of a four junction diode assembly (Electronic Devices, Inc., P/N 5869). The trigger boost network is recommended if the flashtube is to be operated at voltages below 750 Vdc. A single trigger boost network at a flash rate of 1 pps has the following operating limits:

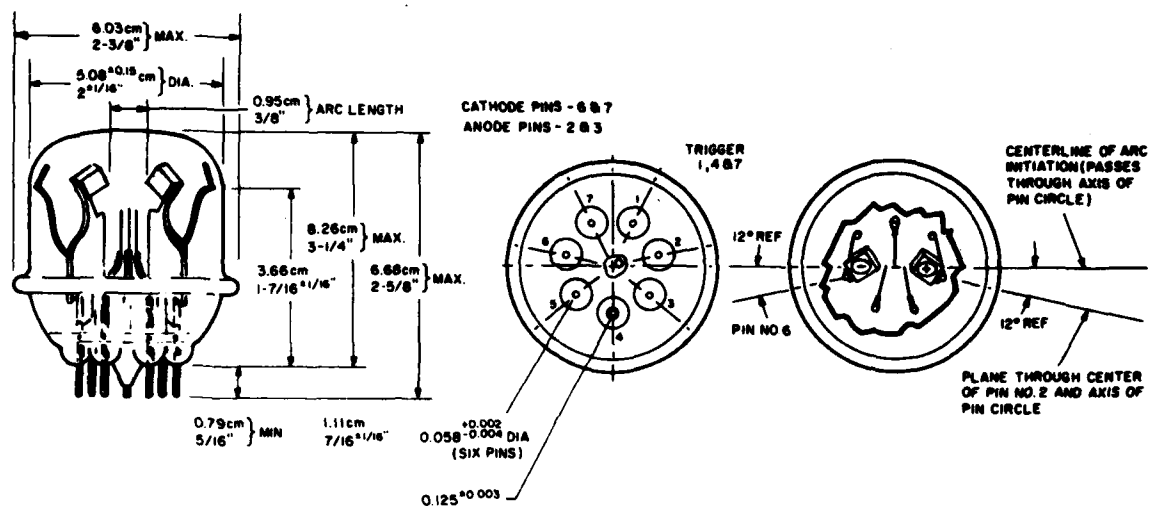
PEAK CURRENT MAX. (a)	PULSE WIDTH 1/3 PEAK (μs)
2000	1-50
1500	50-200
1100	200-500
600	500-1000

Maximum current may be increased by the use of additional networks connected in parallel. Pulse to pulse time jitter is minimized by use of the trigger boost network.

3. The FY-7 LITE-PAC* consists of a ceramic tube socket, trigger transformer, and other components necessary to reliably trigger the FX-132.

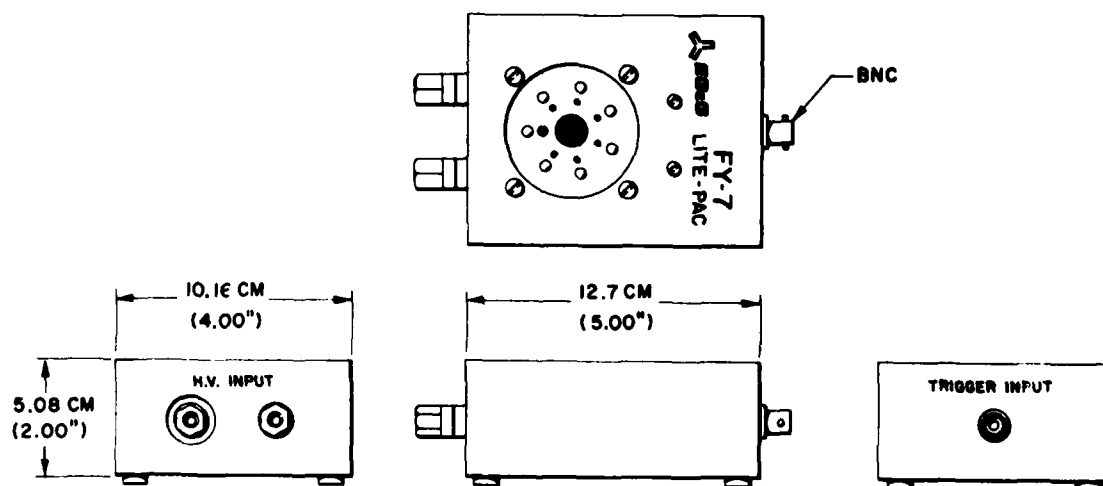
MECHANICAL DATA

FX-132 FLASHTUBE



SOCKET: E. F. JOHNSON - NO 122-247-200
 7 PIN SEPTAR

FY-7 LITE-PAC*



* Registered EG&G Trade Mark

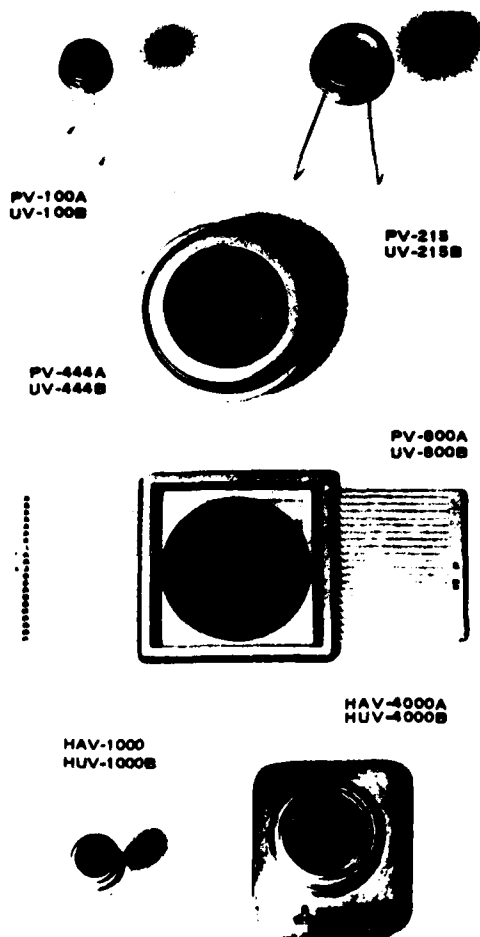


35 CONGRESS STREET SALEM, MASS. 01970
 TEL: (617) 745-3200 TWX: 710-347-6741

Printed in U.S.A. 4/81



SILICON "PHOTOVOLTAIC" DETECTORS AND DETECTOR/AMPLIFIER COMBINATIONS



APPLICATIONS

- ANALYTICAL INSTRUMENTS FOR UV-VISIBLE-IR
 - SPECTROPHOTOMETERS
 - PHOTOMETERS-RADIOMETERS-SPECTRORADIOMETERS
 - DENSITOMETERS
- PROCESS CONTROL AND INSTRUMENTATION
 - UV RADIATION MONITOR
 - FLAME AND EXHAUST MONITOR
 - OPTICAL PYROMETER
 - POINT-OF-SALE LABEL READER
 - EVENT COUNTER
 - OPTICAL ENCODER
 - FLAW DETECTOR
- MEDICAL DIAGNOSTIC INSTRUMENTS
 - SERUM PROTEIN DETERMINATION
 - HEMOGLOBIN TEST

FEATURES

- PLANAR DIFFUSED, OXIDE PASSIVATED STRUCTURE
- WIDE SPECTRAL RANGE - 200 TO 1150 NANOMETERS
- PEAK RESPONSIVITY: 0.65 AMPERE/WATT @ 950 NM
- UV RESPONSIVITY: 150 MILLIAMPS/WATT @ 280 NM
- FLAT NOISE SPECTRUM TO DC
- NOISE CURRENT - 1×10^{-14} TO 7×10^{-14} AMPERE/Hz^{1/2}
DEPENDENT ON ACTIVE AREA SIZE
- LINEARITY OVER WIDE DYNAMIC RANGE
- TEMPERATURE COEFFICIENT OF RESPONSIVITY
 - $\leq 0.05\%/^{\circ}\text{C}$ @ 900 nm
 - $\leq 0.18\%/^{\circ}\text{C}$ @ 200 nm
- SPECTRAL STABILITY - NO HYSTERESIS OR MEMORY EFFECTS

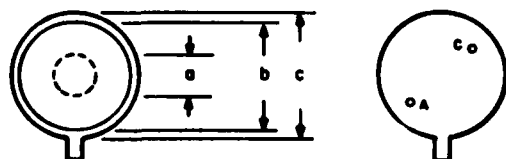
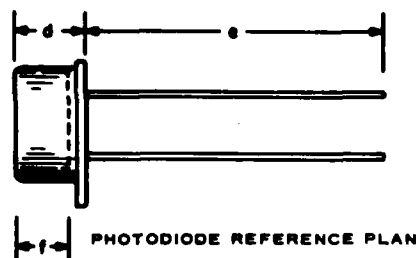
OPERATING DATA & SPECIFICATIONS*

SILICON PHOTOVOLTAIC PHOTODIODES (PV & UV SERIES)

CHARACTERISTIC	PV SERIES				UV SERIES						UNITS AND CONDITIONS
	PV-040	PV-100A	PV-215	PV-444A	UV-040B	UV-100B	UV-215B	UV-250B	UV-444B	UV-500B	
ACTIVE AREA	0.81	5.1	22.6	180	0.81	5.1	22.6	21	180	314	mm ²
SPECTRAL RANGE	380 - 1100				380 - 1100						nm
RESPONSIVITY AT λ_1	0.47	0.47	0.47	0.47	0.46	0.46	0.46	0.46	0.46	0.46	amps/watt at 900 nm
RESPONSIVITY AT λ_2	0.05	0.05	0.05	0.05	0.15	0.15	0.15	0.15	0.15	0.15	amps/watt at 200 nm
RESPONSIVITY AT λ_3	0	0	0	0	0.18	0.18	0.18	0.18	0.18	0.18	amps/watt at 200 nm
CAPACITANCE	25	150	700	2000	25	150	700	600	2000	1000	picofarads
SHUNT RESISTANCE	> 500	> 100	> 50	> 10	> 500	> 100	> 50	> 75	> 10	> 5	megohms
NOISE CURRENT	6	15	20	40	6	15	20	18	40	60	10 ⁻¹⁵ amperes/Hz ^{1/2} at 10 Hz
NOISE EQUIVALENT POWER	1	3.2	4.3	9.0	1	2.5	3.3	3.0	6.7	10	10 ⁻¹⁴ watts/Hz ^{1/2} at 900 nm
NOISE EQUIVALENT POWER	—	—	—	—	3	7	10	9	22	30	10 ⁻¹⁴ watts/Hz ^{1/2} at 200 nm
TEMP. COEFFICIENT OF:											
RESPONSIVITY AT λ_1	+0.05				+0.05						percent/°C at 900 nm
RESPONSIVITY AT λ_2	—				-0.10						percent/°C at 200 nm
RESPONSIVITY AT λ_3	—				-0.18						percent/°C at 200 nm
SHUNT RESISTANCE	-20.0				-20.0						percent/°C
RESPONSE LINEARITY	< 1.0				< 1.0						percent over 6 decades
SURFACE UNIFORMITY	< 1.0%				< 1.0%						with 0.13 mm spot scan
PACKAGE STYLE	TO-5	TO-5	TO-8	TO-36	TO-5	TO-5	TO-8	TO-5	TO-36	DIP	See mechanical.

*NOTES See Application Note D3011 for definitive analysis of silicon photovoltaic detectors and detector/amplifier combinations.

MECHANICAL - PV & UV SERIES

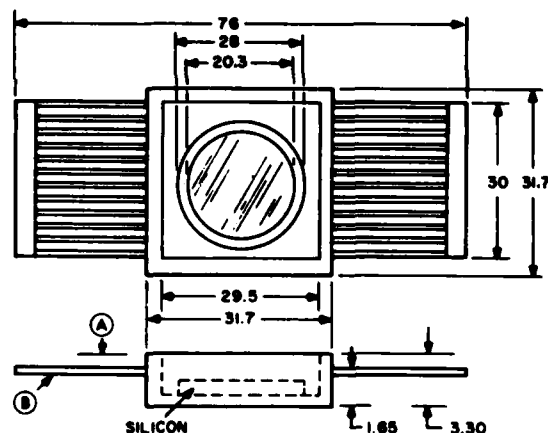


NOTE: NO TAB QN PV-444A & UV-444B
ALL DIMENSIONS IN MILLIMETERS

DIMENSION (mm)	PV-040 UV-040B	PV-100A UV-100B	PV-215 UV-215B	PV-444A UV-444B	UV-500B
a	1.0	2.54	5.46	11.28	7.0
b	4.6	8.4	12.3	27.7	8.4
c	5.2	9.2	14.0	31.8	9.2
d	4.0	4.2	5.1	7.37	4.0
e	> 20.0	> 20.0	> 20.0	> 12.7	> 20.0
f	3.45	2.3	3.45	5.4	2.3
Pin Circle Radius	1.3	2.5	3.78	9.5	2.8
Window Thickness	0.9	1.3	1.3	1.6	1.0
Window Diameter	3.50	6.1	10.7	21.0	7.7
Lead Diameter	0.45	0.45	0.45	1.02	0.45

Gold plated Kovar leads, base and cap.
Window - Corning 7052 glass for PV Series.
Quartz for UV Series.

MECHANICAL - UV-500B



Gold plated Kovar case and leads.

- (A) DISTANCE FROM TOP SURFACE TO TOP OF SILICON = 2.7
- (B) TAB THICKNESS 0.254

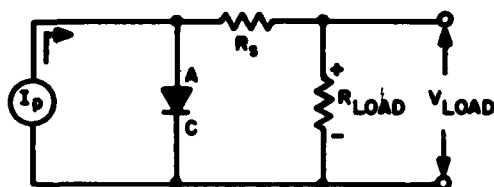
NOTE: ALL DIMENSIONS IN MILLIMETERS!

SPECIAL PHOTODIODE CONFIGURATIONS

EG&G REGULARLY PROVIDES CUSTOMIZED PHOTODIODES AND PACKAGING INCLUDING PHOTODIODE/AMPLIFIER CONFIGURATIONS FOR OEM, R&D, SPACE AND MILITARY APPLICATIONS.

APPENDIX A-4
APPENDIX A-5

OPERATING CIRCUIT (PV, UV SERIES)



LINEARITY EQUATION (PV, UV SERIES)

$$I_{PM} = \left[\frac{25 \times 10^{-3}}{R_S + R_L} \right] \ln \left[\frac{(P)(R_{SH})}{R_S + R_L} \right]$$

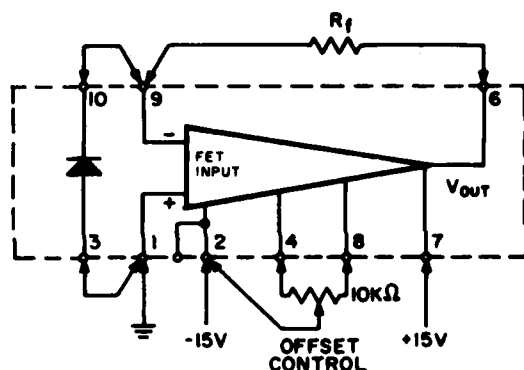
Where:

I_{PM} = Maximum Photocurrent to maintain desired Percent Linearity

P = Percent Linearity desired ÷ 100%

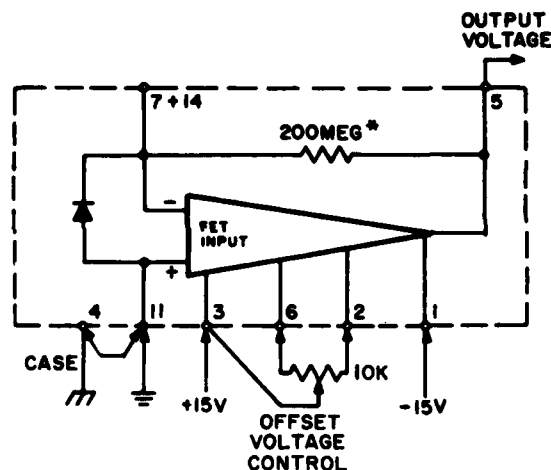
R_S = Series Resistance

OPERATING CIRCUIT - HAV-1000 & HUV-1000B



NOTE: CASE AT -15V POTENTIAL

ELECTRICAL WIRING DIAGRAM - HAV-1000A
HAV-4000A & HUV-4000B



* OTHER VALUES OF R_f CAN BE OBTAINED BY REQUEST.

NOTE: IT MAY BE NECESSARY TO SHUNT R_f WITH $\approx 1pF$ TO REDUCE GAIN PEAKING.

All Data and Specifications Subject to Change Without Notice.



35 CONGRESS STREET SALEM, MASS. 01970
TEL: (617) 745-3200 TWX: 710-347-6741

Printed in U.S.A. 5/80



SILICON DETECTOR CORPORATION, 1355 Rancho Conejo Blvd., Newbury Park, CA 91320, Phone: 805/499-6732, Telex: 916/336-1543

GENERAL PURPOSE DETECTORS



GENERAL DESCRIPTION

SDC's General Purpose Detectors exemplify the current state-of-the-art in hi-rel planar technology and are offered in an extensive assortment of sizes. Red/IR, Blue and UV spectral options are available and each unit can be supplied with the detector isolated from its hermetic metal package. These devices are optimized for use with either of two basic circuit interfaces as described below.

The PHOTOVOLTAIC GROUP of General Purpose Detectors delivers unexcelled performance in low to medium frequency applications. The design of this group specifically optimizes signal-to-noise ratio and signal linearity when driving transimpedance preamplifiers (current-to-voltage amplifiers). Although no bias is usually applied to detectors in this circuit configuration, reverse bias may be used to improve frequency response and large signal linearity with extremely small resultant dark currents.

The PHOTOCONDUCTIVE GROUP is intended for high frequency applications. These detectors are normally reverse biased and have small junction capacitance. Low dark currents result in superior signal-to-noise characteristics and small d.c. offsets. Reverse biases of over 100 volts may be applied to most detectors of this group. A Photoconductive Detector can be used to drive a transimpedance amplifier or can be wired in series with a load resistor to drive a voltage amplifier in very high frequency applications.

APPLICATIONS

- Nephelometers and Turbidimeters
- Densitometers
- Photometers and Radiometers
- Colorimeters and Glossimeters
- Optical Communications and Facsimile Systems
- Laser Detection and Alignment
- High Frequency Isolators and Encoders

CHARACTERISTICS

- High Responsivity - .55A/W at Peak
- Extremely Low Dark Current -
100nA/cm²@50 Volts
- Very High Dynamic Junction Impedance -
1000M Ω (SD-041-11-11)
- No 1/f Noise - Photovoltaic Mode
- Excellent Output Linearity -
More than 11 Decades
- High Frequency Response -

OPERATING SPECIFICATIONS (23°C) PHOTOVOLTAIC GROUP - ULTRA-LOW NOISE / MEDIUM FREQUENCY DETECTORS

MODEL NUMBER	SPECTRAL ENHANCEMENT	ACTIVE SURFACE		TYP. (1) RESPONSE AT SPECTRAL PEAK (A/W)	MIN (2) DYNAMIC RESISTANCE (MΩ)	TYP. JUNCTION CAPACITANCE -C _j		TYP. DARK CURRENT (nA)	TYP. RESPONSE TIME (10% - 90%)		TYP. NEP Spectral Peak 0 Vols 1 MHz (W/√Hz)	MAX OR LINEAR OUTPUT CURRENT - I _o (mA)
		Area (mm ²)	Dimensions (in)			0 Vols (pF)	5 Vols (pF)		0 Vols (ns)	5 Vols (ns)		
SD-041-11-11-011 (ISOLATED) -211	RED/IR	0.85	0.40 x .033	50	500	85	39	.13	9	4.1	7.3 x 10 ⁻¹⁵	.085
SD-041-12-12-011 (ISOLATED) -211	BLUE	0.85	0.40 x .033	50	500	85	39	.13	18	8	7.3 x 10 ⁻¹⁵	.082
SD-076-11-11-011 (ISOLATED) -211	RED/IR	2.91	1.05 x .043	50	200	290	132	.45	16	7.3	1.2 x 10 ⁻¹⁴	.30
SD-076-12-12-011 (ISOLATED) -211	BLUE	2.91	1.05 x .043	50	200	290	132	.45	46	21	1.2 x 10 ⁻¹⁴	.27
SD-100-11-11-021 (ISOLATED) -221	RED/IR	5.1	1.00 (DIA)	50	100	510	232	.75	23	10	1.7 x 10 ⁻¹⁴	.50
SD-100-12-12-021 (ISOLATED) -221	BLUE	5.1	1.00 (DIA)	50	100	510	232	.75	75	34	1.7 x 10 ⁻¹⁴	.42
SD-172-11-11-021 (ISOLATED) -221	RED/IR	15.0	1.85 x 1.25	50	70	1,500	682	2	56	25	1.9 x 10 ⁻¹⁴	1.5
SD-172-12-12-021 (ISOLATED) -221	BLUE	15.0	1.85 x 1.25	50	70	1,500	682	2	207	94	1.9 x 10 ⁻¹⁴	.94
SD-200-11-11-041 (ISOLATED) -241	RED/IR	20.3	2.00 (DIA)	50	50	2,030	923	3	73	33	2.3 x 10 ⁻¹⁴	2.0
SD-200-12-12-041 (ISOLATED) -241	BLUE	20.3	2.00 (DIA)	50	50	2,030	923	3	280	128	2.3 x 10 ⁻¹⁴	1.1
SD-200-13-13-042 (ISOLATED) -242	UV	20.3	2.00 (DIA)	50	50	2,030	923	3	280	128	2.3 x 10 ⁻¹⁴	1.1
SD-290-11-11-041 (ISOLATED) -241	RED/IR	42.6	3.00 x .220	50	20	4,260	1,936	7	147	87	3.6 x 10 ⁻¹⁴	4.2
SD-290-12-12-041 (ISOLATED) -241	BLUE	42.6	3.00 x .220	50	20	4,260	1,936	3 @ 1 V	475	216	3.6 x 10 ⁻¹⁴	1.5
SD-290-13-13-042 (ISOLATED) -242	UV	42.6	3.00 x .220	50	20	4,260	1,936	3 @ 1 V	475	216	3.6 x 10 ⁻¹⁴	1.5
SD-444-11-11-171 (ISOLATED) -251	RED/IR	100	4.44 (DIA)	50	10	10,000	4,545	15	336	153	5.1 x 10 ⁻¹⁴	10
SD-444-12-12-171 (ISOLATED) -251	BLUE	100	4.44 (DIA)	50	10	10,000	4,545	7 @ 1 V	1100	510	5.1 x 10 ⁻¹⁴	2.0
SD-444-13-13-172 (ISOLATED) -252	UV	100	4.44 (DIA)	50	10	10,000	4,545	7 @ 1 V	1100	510	5.1 x 10 ⁻¹⁴	2.0

(1) See Page 5 for complete spectral response.

(2) Typical values of Dynamic Resistance are 4x the minimum values shown here. Selection can be performed.

(3) This denotes the level above which the output current deviates more than 10 percent from the ideal linear relationship extrapolated from the low light level region. The short circuit current saturates at about 10x this value.

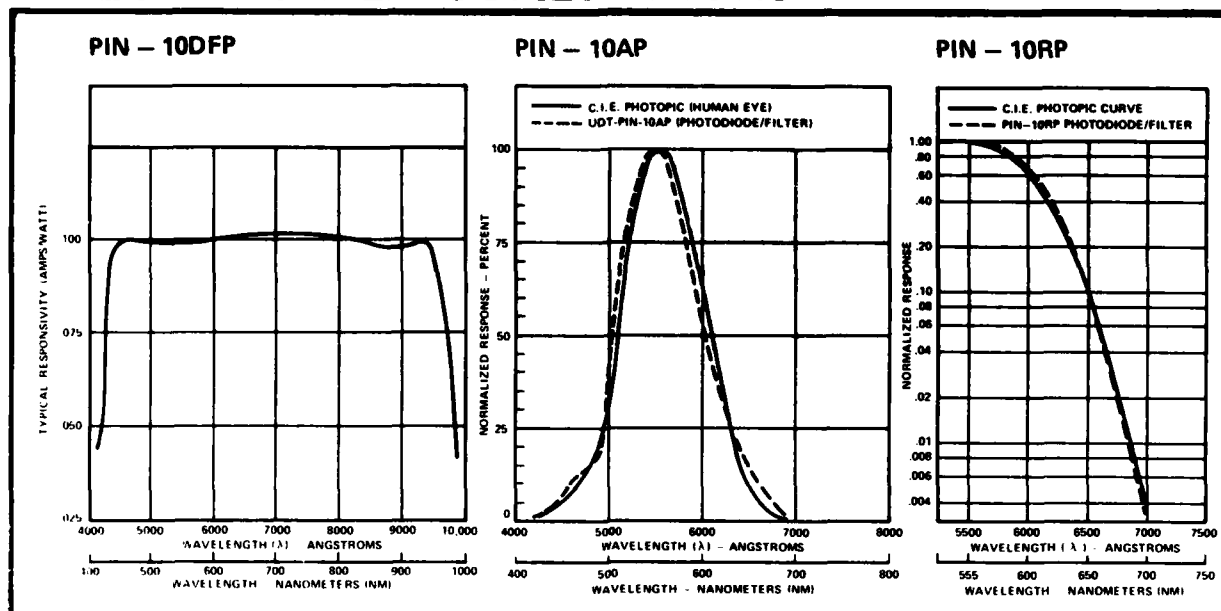
UNITED DETECTOR



TECHNOLOGY INC.

DATA SHEET 9F006

DETECTOR/FILTER COMBINATIONS




THESE DETECTOR/FILTER COMBINATIONS combine PIN silicon photodiode and a multiple element colored glass subtractive filter. With the glass filter element mounted in front of the detector, the spectral response curves shown above are produced. The glass subtractive filter is computer designed to correct the detector spectral response to the desired spectral response. This is accomplished by cementing together as many as five separately polished colored glass types and then individually mating this filter to a spectrally selected photodiode. Since UDT is a volume manufacturer of PIN photodiodes, the spectral selection of photodiodes from production runs is possible. All three of the combinations, PIN-10DFP, PIN-10AP, and PIN-10RP, are mounted in identical housings, shown in the photograph (Lower Right). The detector has a BNC output.

THE PIN-10DFP (DETECTOR/FILTER COMBINATION) produces a flat spectral response from 450 nanometers to 950 nanometers. This is the spectral response required for radiometric measurements, and is the response exhibited by thermopiles. The advantages of the PIN-10DFP over thermopiles are stability and sensitivity. The PIN-10DFP is a thousand times more sensitive than a thermopile, and ten times more stable than a thermopile. The PIN-10DFP can be calibrated by UDT (traceable to NBS) in terms of microamps out per microwatts of light into the PIN-10DFP. The PIN-10DFP is supplied uncalibrated unless otherwise ordered.

THE PIN-10AP (DETECTOR/FILTER COMBINATION) produces a spectral response that duplicates the human eye (C.I.E. standard photopic curve). This is the spectral response required for photopic measurements. The unit can be calibrated by UDT in terms of microamps out per ft. candle incident. The PIN-10AP is supplied uncalibrated unless otherwise ordered.

THE PIN-10RP (DETECTOR/FILTER COMBINATION) produces a spectral response that duplicates the C.I.E. photopic curve in the red region, from 5800Å to 7200Å. By concentrating the filter design on this region only, an extremely close match has been achieved. The deviation between the PIN-10RP spectral response and the C.I.E. curve is less than 5%. This close match is especially useful for visible LED measurements in photopic units. A correct value for LED photopic output is obtained independent of LED peak wavelength. The PIN-10RP can be calibrated by UDT in terms of microamps out per ft. candle. The PIN-10RP is supplied uncalibrated unless otherwise ordered.

UNIQUE CHARACTERISTICS	<ul style="list-style-type: none"> • Spectral matching to $\pm 5\%$ (PIN - 10RP) • Linear output: 10^{-11} watts to 10^{-3} watts • Frequency Response: 10^{-5} ft. candles to 10^3 ft. candles • Active Areas: 1cm^2 	
APPLICATIONS INCLUDE	<ul style="list-style-type: none"> • Photometers • Spectroradiometers • Laser power meters • LED calibrators • Thermopile replacement 	

PIN - 10DFP PIN - 10AP PIN - 10RP

UNITED DETECTOR TECHNOLOGY INC.

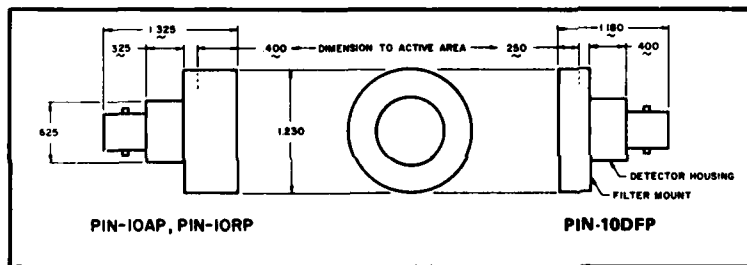
2644 30TH STREET, SANTA MONICA, CA 90405 • TELEPHONE (213) 450-8585 • TELEX 65-2413

APPENDIX A-7

DETECTOR/FILTER COMBINATIONS ELECTRO·OPTICAL CHARACTERISTICS (TYPICAL)

	PIN-10DFP	PIN-10AP	PIN-10RP	UNITS
Responsivity:	.1	.4	.4	$\mu\text{A}/\mu\text{W}$ mA/L
Capacitance	10	10	10	nF @ 0 bias
Dark Current @ 3V (typ.)	—	1.0	1.0	μA
Rise Time:	1.0	1.0	1.0	μs @ 0 bias
Active Area:	1	1	1	cm^2
Spectral Match:	$\pm 7\%$ (point by point)	$\pm 2\%$ (area)	$\pm 5\%$ (point by point)	
Source Impedance	1.0	1.0	1.0	M Ω (min.)
Source Resistance	—	5M Ω	5M Ω	@ 3V
NEP	1×10^{-11}	1×10^{-11}	1×10^{-11}	W/ $\sqrt{\text{Hz}}$ @ 850 nm

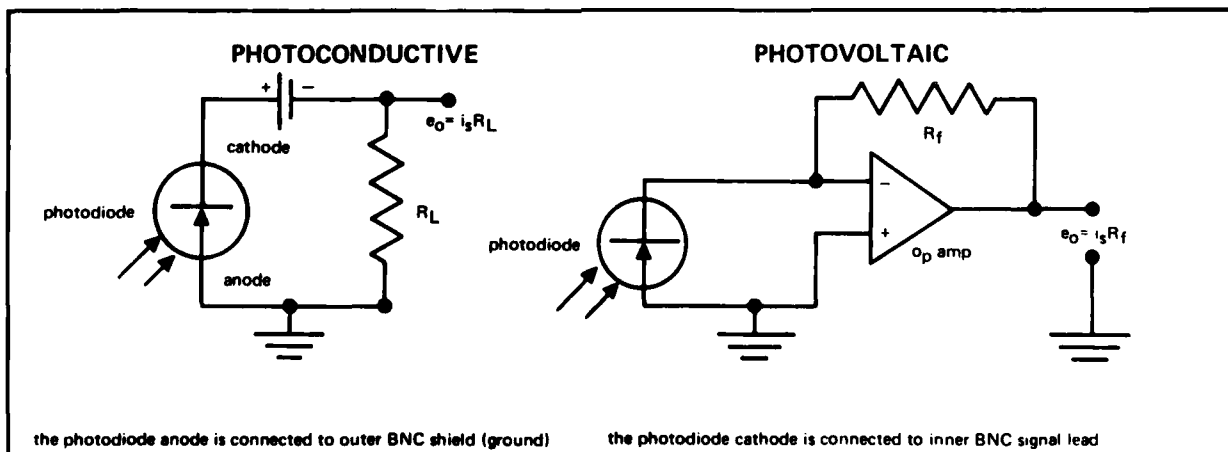
MECHANICAL DETAILS



** this is the maximum deviation point by point from 570 to 730 nanometers.

NOTE: PIN-10DFP, PIN-10AP and PIN-10RP have been optimized to photovoltaic operation.

TYPICAL HOOKUPS



UNITED DETECTOR TECHNOLOGY INC.

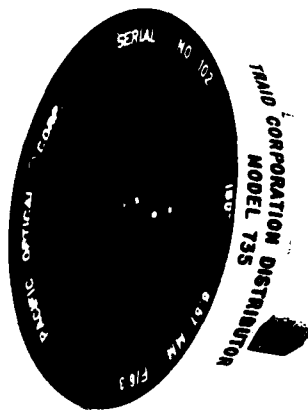
2644 30TH STREET, SANTA MONICA, CA 90405 • TELEPHONE (213) 450-8585 • TELEX 65-2413

PRODUCT PROFILE NO. 25-A

735 Periphoto

180° LENS FOR 35mm CAMERAS

TRAID CORPORATION • BOX 648 • 17136 VENTURA BOULEVARD • ENCINO, CALIFORNIA • ST. 8-2210 OR TR. 3-3373



The compact Traid 735 Periphoto Lens, shown above in actual size, provides hemispherical coverage — a full 180°

FEATURES

- 180° Field of View
- Miniaturized
- Limited Distortion
- High Resolution
- Speed of f/6.3
- Eyemo Mount
- Reasonably Priced

The most exciting product to be offered in some time is the Traid 735 wide angle lens. With a 180° field of view and extremely high resolution, this unusually small lens opens up many new areas for 35mm camera users.

Designed and manufactured for Traid by Pacific Optical Company for use in scoring systems — and for which it is ideally suited — the 735 can prove invaluable in many other situations as well.

For example: If the 735 were installed flush with the wall in a room of any size, it would cover the whole area like a paint job and wall-to-wall carpeting! The possibilities here for security or surveillance use are limit-

less; or imagine taking pictures of an entire football field without moving the camera or lens from the sideline; or set up your camera and 735 lens on the ground and get a full picture of the sky — horizon-to-horizon — the study of cloud formations made easy! Installed on a drone the coverage would prove incomparable in determining if the missile or rocket, coming from above, below, either side, head-on and from any angle, was a hit or a miss — or how close.

Probably one of the main applications outside of scoring systems and study of the sky will be where conditions are such that the camera and lens must be extremely close to the subject being photographed.

Rental Plan

This equipment is also available on a rental basis. In addition, there are seventy-five other Traid products which may be rented. The rental rate is computed from the indicated and advertised selling price for each product as follows: Daily rate 2%; weekly rate 6%;

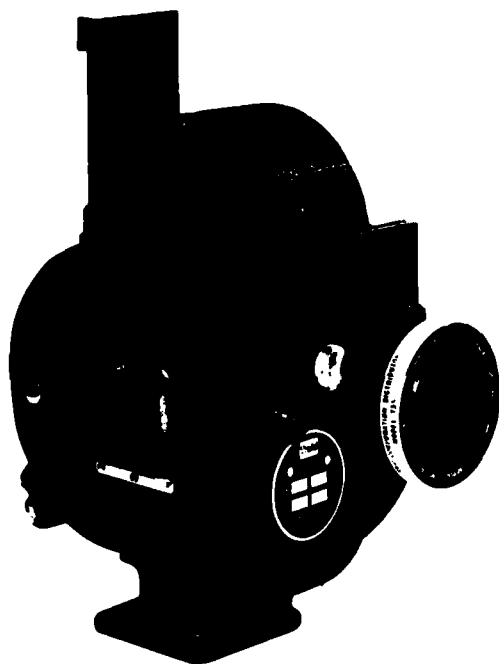
monthly rate 18%. On one-year lease 6% per month; on two-year lease 5% per month; on three-year lease 4% per month. Special long term rates will be quoted on request. Rates are quoted F.O.B. Encino and sales tax is applicable under the same terms and conditions that apply to purchases.

APPENDIX A-8

Shown is a blow-up of an actual 35mm frame shot with the Traid 735.

Camera: Traid 75A Fototracker
 Camera Speed: 20 Frames per Second
 Shutter Opening: 40°
 Film: Background X
 Exposure: 1/180th Second
 Filter: #2 Yellow

Shot was taken straight up — from atop our building. Note trees, buildings, telephone wires, etc. on periphery. Sun was directly in camera view.



Pictured is the 735 lens mounted on that reliable stand-by, the Traid 75A Fototracker. Ideal for airborne instrumentation, this versatile package offers the combination of 35mm format, wide angle coverage, variable shutter and speeds of 20, 40, 60 and 80 frames per second. Write us for detailed specifications on the 75A.

SPECIFICATIONS

Equivalent Focal Length 6.51mm
 • Rugged Eyemo Mount
 Relative Aperture f/6.3, Fixed
 Flange Focus Distance 1.500"
 180° Field of View
 Resolution 80 Lines Per MM on Axis
 Color Corrected for Daylight Kodachrome
 Fixed Focus, 60" to Infinity
 Five Element Reverse Type Telephoto
 67% Distortion at 75°, 23% at 45°
 Round Image, .720" Diameter
 Magnesium Fluoride Coating
 Finish: Black Anodize, Clear Anodize and
 White Enamel
 Length 1 1/8"
 Weight 5 1/2 Ounces
 Metal Lens Cap
 Rubber Rear Cap
 Price ~~985.00~~

*Other mounts on special order

985.00
 902.00

NOTE: Overlay Grids available from Traid

FOR FURTHER
 INFORMATION CONTACT:
 TRAIT CORPORATION

Bell & Howell Special Representative
 17136 Ventura Blvd.
 Encino, California

LITHO IN U.S.A.

10/60

REV	CHANGE	BY	DATE		TRAID 735
<p>SPECIFICATIONS</p> <ol style="list-style-type: none"> 1. INCLUDED ANGLE, 180° 2. MOUNT, EYEMO TYPE (WITHOUT KEY) 3. FIXED FOCUS AT INFINITY 4. ROUND IMAGE, .720 DIA. 5. RELATIVE APERTURE, f6.3 (NO IRIS) 6. COATED MAGNESIUM FLOURIDE 7. FILTERS, NONE 8. 3 FIDUCIAL MARKS IN HORIZONTAL PLANE (UPON REQUEST) 					
<p>UNLESS OTHERWISE SPECIFIED</p> <p>FRACTIONAL DIM. TO UNFINISHED SURFACE ± 1/32 FRACTIONAL DIM. TO FINISHED SURFACE ± .010 THREE PLACE (1000) DECIMAL DIM ± .005</p> <p>ANGULAR DIM ± .1°</p> <p>DIMENSIONS ON SAME CENTER LINE TO BE CONCENTRIC WITHIN .003 ± .0003 TIR BREAK SHARP CORNERS .005 ± .45° SURFACE FINISH 83V</p>					
<p>DR 5-6-60 <i>TR</i> APP</p> <p>SCALE: FULL</p>					
<p>NO REQ NEXT ASSEMBLY MODEL</p>					
<p>DO NOT SCALE THIS DRAWING</p>					
<p>180 DEGREE LENS</p>					
<p>CORPORATION ENCINO, CALIF.</p>					
<p>TRAID 735</p>					

APPENDIX A-9

OPERATING INSTRUCTIONS FOR THE SOLIGOR FISH-EYE CONVERSION LENS

The Soligor Conversion Fish-Eye lens can be used successfully with just about any camera from 8mm movie to 8x10" view. In conjunction with normal focal length lenses, the Auxiliary Fish-Eye produces the typical circular Fish-Eye format with 180° coverage. The afocal auxiliary design of the Soligor Fish-Eye has many distinct and unique advantages over "prime" Fish-Eye lenses. Among them:

- * An almost universal adaptability to a wide variety of cameras and prime lenses.
- * The ability to function with various focal length lenses, yielding, in each particular combination, a resultant focal length of .15X the prime focal length. Example: 50mm focal length is converted to 7.5mm, 135mm is converted to 20.25mm and so on.
- * The normal camera viewing system is used, so that with SLR cameras, the mirror need not be locked up, out of the way, and focusing and composing is done normally on the groundglass in the usual manner.
- * In conjunction with the focusing mount of the prime lens, objects as close as 1/2" from the front of the Fish-Eye can be brought into sharp focus.

SUITABILITY.

The Soligor Fish-Eye lens is suitable for virtually all types of cameras including 8mm, Super 8mm and 16mm, as well as 35mm movie cameras; T.V. cameras; subminiature cameras; half size and regular size 35mm rangefinder and single lens reflex cameras; 2-1/4x2-1/4", 4x5", 5x7", 8x10" view and press cameras.

The Soligor Fish-Eye lens is not recommended for use with wide angle lenses (resulting diameter of circular image too small), for lenses longer than 200mm (resulting speed too slow), some zoom lenses (both diameter of circular image and image quality may be unsatisfactory), prime lenses into which Fish-Eye cannot be screwed or bayoneted (slip-on fittings are not suitable), lenses with a greatly recessed front element (may cause vignetting due to increased distance between prime and auxiliary lens).

MOUNTING THE AUXILIARY FISH-EYE TO THE CAMERA LENS.

The Soligor Auxiliary Fish-Eye is equipped with a thread at the rear. Mounting rings of various diameters are available to fit most lenses. Also a Series VI or VII mounting ring is available. This permits mounting the lens to the vast majority of camera lenses in conjunction with standard Series VI or VII adapter rings.

Lenses requiring a Series VIII adapter ring should be fitted with a standard Series VIII to VII Step-down ring. Lenses requiring Series V adapters require a standard Series V to VI Step-up ring.

Simply screw the Fish-Eye lens with the appropriate mounting ring into the camera lens.

Avoid mounting the Fish-Eye with slip-on or set screw adapters, since these tend to be precarious and shift the attachment off the optical axis.

Orienting The Fish-Eye.

If the aperture scale of the Fish-Eye is not centered in the upright position, loosen the set-screw in the base ring of the Fish-Eye, rotate the lens to the desired position and retighten the set-screw.

SETTING THE FOCAL LENGTH SCALE.

Rotate the focal length scale so that the focal length of the prime (camera) lens is set opposite the red dot reference mark. Setting this focal length scale shifts the diaphragm scale, indicating the "f" stops available with that particular focal length combination. Intermediate settings of the focal length scale may be used where required.

VIEWING AND COMPOSING.

On SLR and other cameras with groundglass viewing screens, viewing is direct. With non-groundglass cameras, the approximate field coverage can be estimated.

On twin lens reflex cameras, the Fish-Eye can be shifted from the top lens for viewing and focusing to the lower lens for actual shooting.

It is difficult to visualize the extreme angle of coverage of the Fish-Eye, even when using a reflex viewing system. The usual position of tripod legs, your hat, or even your own feet may show in the Fish-Eye picture unless you take special care to avoid this.

Focusing.

While the Fish-Eye has no focusing mount of its own, with SLR and view cameras the focusing mount of the prime lens is effective in varying focus to objects from infinity to only 1/2" from the lens. With the prime lens set to infinity, the depth of field of the Fish-Eye extends from about 3 feet to infinity. At smaller openings, depth of field at the infinity setting may extend to as close as 1-1/2 feet.

Operating the Diaphragm.

Always set the diaphragm of the camera lens to its maximum aperture (wide open). Rotate the diaphragm control ring of the Fish-Eye to the desired "f" stop - the "f" stop shown on the Fish-Eye diaphragm scale is accurate for that focal length setting, and no further compensation is required. For optimum definition, an aperture setting of 2 or 3 stops below the maximum opening is recommended.

Exposure.

Exposure is determined in the usual manner, depending on the opening at which the diaphragm of the Fish-Eye is set. On cameras on which the Fish-Eye covers all or part of the built-in electric eye, the exposure mechanism must be operated manually. When measuring exposure by means of a separate meter, it is important to keep in mind that the average meter covers an angle considerably narrower than that covered by the Fish-Eye, and that the subject may include areas of greatly varying brightness which should be measured separately, with such exposure selected to best record the most significant part of the subject within the total field.

On cameras with through-the-lens metering system, care should be taken that the meter reading area is within the picture field. Meters that integrate the entire groundglass image will give a false reading unless the Fish-Eye is used with 135 mm or longer lenses to yield an image covering the entire film format.

When the Fish-Eye is used with shorter than 135mm focal length lenses on 35 mm through-the-lens meter reading cameras, a separate exposure meter should be used to establish correct exposure.

Care Of The Fish-Eye Lens.

The extreme curvature and exposed position of the front element requires special care in handling and storing to avoid touching and damaging the glass surface. Keep the special cap on the Fish-Eye at all times, except when actually shooting. Brush gently to remove dust and, if necessary, wipe the lens with as light a touch as possible.

Exclusive Quality Import
ALLIED IMPEX CORPORATION
300 PARK AVENUE SOUTH
New York, N. Y. 10010
Chicago • Dallas • Los Angeles

1R5C/368

CHIEFTAIN MICROCOMPUTERS



Chieftain series microcomputers are among the most powerful, yet inexpensive on the market today. While Chieftain microcomputers are considered "low-cost," quality has not been sacrificed in any respect.

For example, each Chieftain microcomputer contains gold-plated connectors throughout to assure long, reliable service. Each board in a Chieftain computer is Endurance-Certified*, then tested (at 2.2 MHz). After your computer is assembled, it is **again** Endurance-Certified, and tested as a complete system. Each disk drive is fully tested both before and after installation in your computer.

Along with these powerful, high-quality microcomputers, **Smoke Signal Broadcasting** also offers a complete line of both hardware and software products to support the Chieftain series. BASIC, Compiler BASIC, FORTRAN, COBOL, PASCAL, Macro-Assemblers, Text Editors and Text Processors, and business application software are just part of what **Smoke Signal Broadcasting** can provide to expand the capabilities of your Chieftain microcomputer.

SPECIFICATIONS

Each standard Chieftain microcomputer contains:

Memory

32k (32,768) bytes of Static RAM standard
(1M bytes addressable)
1k bytes of RAM Scratch pad
2k monitor in EPROM
5 EPROM slots for 20k of 2532 or 10k of 2716

Controller

DCB-4A Double Density Controller

CPU

2 MHz 6800 or
2 MHz 6809

Chassis

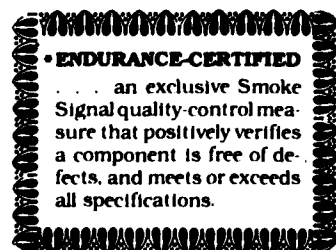
Motherboard: SS-50
Nine Main Slots
Eight I/O Slots
Power Supply: 8V, 16V;
up to 150 watts total output

Software

DOS68 or
DOS69

Enclosure

Simulated Leather
Optional:
Metal Enclosure Rack-Mountable



SPECIFICATIONS — Continued on next page

SS-50/SS-50C BOARDS

MEMORY BOARDS

Each Memory Board from Smoke Signal Broadcasting consists of static RAM. Each has been Endurance-Certified, then fully tested at 2.2 MHz. All memory cards can be addressed to occupy a block of memory starting on any 4k byte boundary in a 1M byte memory space. This 1M byte memory space is organized as sixteen 64k memory pages. The user can disable any 4k block of memory on any Memory Board, allowing other devices to occupy the disabled memory block.

SPECIFICATIONS

	Storage	Input Volts	Typical Input Current	Size	Approximate Shipping Weight
M-16-X	16,384 bytes	7.5 min., 10 max.	1.1 A	22.9 x 14.0 cm (9 x 5.5-in)	0.9 kg (2 lbs)
M-32-X	24,576 bytes	7.5 min., 10 max.	1.5 A	22.9 x 14.0 cm (9 x 5.5-in)	0.9 kg (2 lbs)
M-32-X	32,768 bytes	7.5 min., 10 max.	1.9 A	22.9 x 14.0 cm (9 x 5.5-in)	0.9 kg (2 lbs)

CPU BOARDS

CPU Boards by Smoke Signal Broadcasting are truly single-board computers. The features listed below provide the user with more power and flexibility than found on much more expensive CPU Boards. Each SCB-68 and SCB-69 CPU Board is Endurance-Certified*, then fully tested. All CPU Boards contain:

- A 2 MHz 68B00 or 68B09
- 1k bytes of scratch pad RAM
- 20k bytes of EPROM sockets (20k of 2532 or 10k of 2516)
- Provision for AMD 9511/9512 floating point processor
- FPLA for independent addressing of on-board devices
- Twenty address lines for addressing up to 1M bytes of memory
- SS-50 and SS-50C compatibility

In addition, the SCB-68 has provision for an optional on-board serial port with programmable baud rates to 38k, programmable interrupts, break character generation/detection; two user-defined output lines; and programmable word length and stop bits.

The SCB-69 comes standard with a real-time clock with battery back-up (up to six weeks); interrupt timing down to 10ms; maskable interrupt output with eight possible signals; latches for alarm-type function; counters for month, day-of-month, day-of-week, hours, minutes, seconds and .1, .01 and .001 seconds.

SPECIFICATIONS

	CPU	Input Volts	Typical Input Current	Size	Approximate Shipping Weight
SCB-68	68B00	7.5 min., 10 max.	0.7 A	22.9 x 14.0 cm (9 x 5.5-in)	.9 kg (2 lbs)
SCB-69	68B09	7.5 min., 10 max.	0.9 A	22.9 x 14.0 cm (9 x 5.5-in)	.9 kg (2 lbs)

VIDEO BOARD

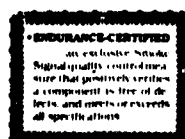
The Smoke Signal Broadcasting VDB-1 Video Display Board provides the user with a convenient means of displaying information on a standard B/W video monitor. The VDB-1 is fully assembled, Endurance-Certified, then tested. It contains all the necessary logic (hardware and software) for controlling the display. The board comes standard with a character set of 96 ASCII and 32 graphic characters. The user can install his own set of up to 256 characters in EPROM.

Additional standard features include:

- 1k EPROM for software drivers
- Reduced intensity or inverted video
- 80 x 24 (1920 characters) display
- Programmable display rate equivalent to 100 to 50k baud
- Protected fields
- Addressable cursor
- 128 bytes of scratch pad RAM
- 2k video display RAM accessible by the CPU as standard RAM memory

SPECIFICATIONS

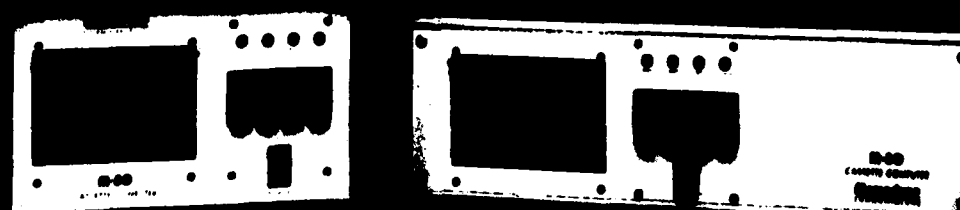
	Output Signal	Input Volts	Typical Input Current	Size	Approximate Shipping Weight
VDB-1	Composite Video (1V p-p into 50 ohms)	7.5 min., 10 max.	0.9A	22.9 x 14.0 cm (9 x 5.5-in)	.9 kg (2 lbs)



BOARDS — Continued on next page

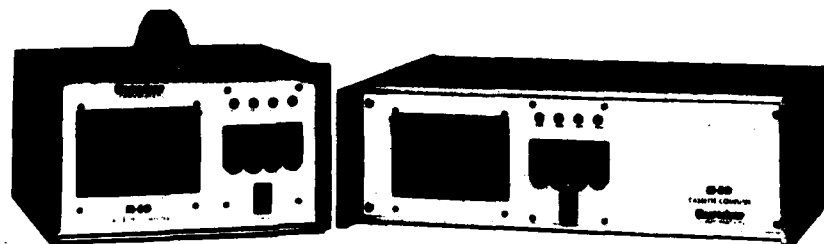
Memodyne

INTELLIGENT DIGITAL CASSETTE RECORDING SYSTEMS



- Off-line data reduction and nonvolatile storage
- RS232C compatible computer storage peripheral
- Real time process control system
- Portable mobile data gathering
- Airborne recording computer
- Automatic systems testing

INTELLIGENT DIGITAL CASSETTE RECORDING SYSTEMS



FEATURES:

Digital Cassette Recorder

- Reel driven, capstanless mechanism for gentle tape handling
- Rugged — designed to provide superior immunity to hostile environments
- High speed: Handles continuous data streams (Reads, writes, transmits and receives) at rates up to 9600 Baud
- Data Storage Capacity: Two tracks accessible on line, each capable of storing 238,000 bytes, formatted, on a standard cassette
- **ANSI/ECMA-34 compatible** in both encoding and formatting (Includes preamble, postamble, C.R.C., and up to 256 data characters per block) Writes and recognizes ANSI/ECMA tape marks
- **Texas Instruments (TI.) compatible:** Reads and writes cassettes compatible with Model 700 series terminals
- **MEMODYNE CNRZ encoding compatible:** Versions available to read all CNRZ- encoded tapes written on Memodyne incremental recorders
- **N.C.R. compatible:** Reads blocks sizes up to 511 bytes
- Auto error detection and retry capability
- 2.4576 MHz system clock
- 1K byte RAM, 2K optional
- 4K bytes of PROM
- Full 64K Z-80™ address space accessible via MEMOBUS™
- Accessory cards available for memory expansion within the M80 module: Model 406 8K static RAM board and Model 407 4K to 16K U.V.-EPROM board
- Four channel Integrating A/D Converter Card, Model 408, 12 bits plus sign

Front Panel Keypad

- Front panel keypad allows control of the M80 without a separate terminal and leaves serial ports completely open.
- M80 will accept and process keypad commands and user-generated RS232C data alternatively
- Two-level operation allows for simple control of recorder, while implementing the full M80 command repertoire
- Reliable bounce-free Hall-effect switches
- LED status indicators
- Internal selector switches for baud rate and serial communication format

Computer

- Memodyne interrupt-driven firmware controls recorder and communication functions transparently in user programs

SPECIFICATIONS:

Recording Media: Philips Certified Digital Cassette, 300 feet, ANSI/ECMA compatible

Recording Head: Read-While-Write, dual track

Recording Density: 800 bits per inch

Input/Output: RS232C and TTY current loop

Data Transfer Rates: 110, 150, 300, 600, 1200, 2400, 4800, and 9600 baud

Data Capacity: 250,000 bytes per track for total of 500,000 bytes — formatted

Data Format: Phase encoded or CNRZ

Block Size: Selectable up to 256 bytes per block

Interrecord Gap Length: 1.0 inches, nominal

Tape speeds: 19.2 inches per second — Read and Write; 100 inches per second — search and rewind

System Clock Rate: 2.4576 MHz

Error Rate: Soft errors, 1 in 10^7 retrieved
Hard errors are cassette dependent

Commands: Tape On, Tape Off, X On, X Off, Rewind, Load Forward, Set Erase, Write File Gap, Transmit Status, Set Baud Rate, Set Block Size, Select Track, Execute User Program

Power Requirements: 115 VAC $\pm 10\%$ 50-60 Hz, 220 VAC optional.
Power consumption:
Peak 80 watts max
Average 50 watts

Operating Temperature: 0°C to +50°C

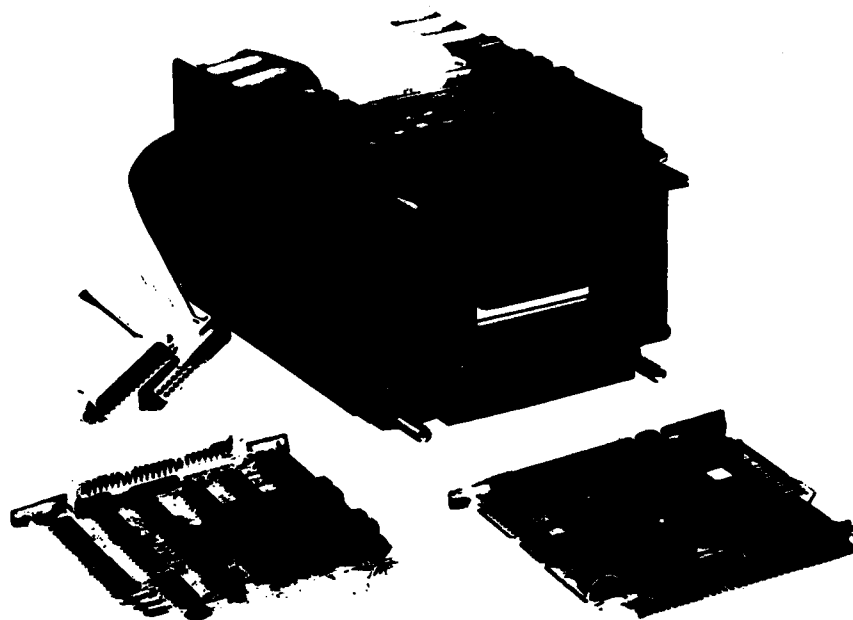
Storage Temperature: -35°C to +70°C

Relative Humidity: 20 to 80%, no condensation

MECHANICAL DIMENSIONS

Size: in 2000 case H 6 $\frac{1}{4}$ " x W 10 $\frac{1}{2}$ " x D 12"
in 3000 case H 5 $\frac{1}{4}$ " x W 17" x D 15"

Weight: in 2000 case 16.1 lbs
in 3000 case 18.6 lbs



MODEL M80 SHOWN WITH
MODEL 403 INTERFACE
CARD AND MODEL 402 CPU CARD

GENERAL DESCRIPTION:

The M80/2000FPC and M80/3000FPC Systems combine a patented high-speed digital cassette recorder with a general purpose Z-80 based computer to perform a wide variety of tasks. The systems can operate as intelligent digital cassette recorders handling continuous data streams at rates up to 9600 baud, as stand-alone computers with a full 64K-byte, Z-80 memory capacity residing on an M80 Spare Card or, by combining the two preceding functions, as intelligent recording peripherals.

They may be used as straightforward laboratory computing recording instruments under local control, or remote, slaved peripherals in distributed processing applications. The systems have full-duplex modem and terminal RS-232C and TTY current-loop serial I/O ports for easy interfacing. For maximum utility, the M80 recorder and communication functions operate under interrupt-driven control, enabling the systems to perform background tasks in support of the host computer or other peripherals on the bus. These tasks include transducer linearization routines, front-end data reduction and execution of external user programs.

The Models M80/2000FPC and M80/3000FPC consist of the following: The M80 transport and electronics module, a Model 411 control keypad, a triple-output linear power supply, all necessary power and signal cables, and either the 2000 style (portable) case or the 3000 style (rack mountable) case.

Modularity of the M80 system is made possible by the use of standard 50-pin and 60-pin ribbon cable and matching edge connectors. The 411 control keypad is connected via 60-pin ribbon cable to the M80 module bus extension. The M80's serial interface 403 card provides for RS232C compatible interfacing, brought out to the rear panel by a 50-pin ribbon cable with a pin-and-socket type connector on the 403 card, and two standard 25 pin connectors mounted on the rear panel, one for terminal type devices, and one for modem-type devices.

The M80 system structure is illustrated in the "M80 Functional Block Diagram".

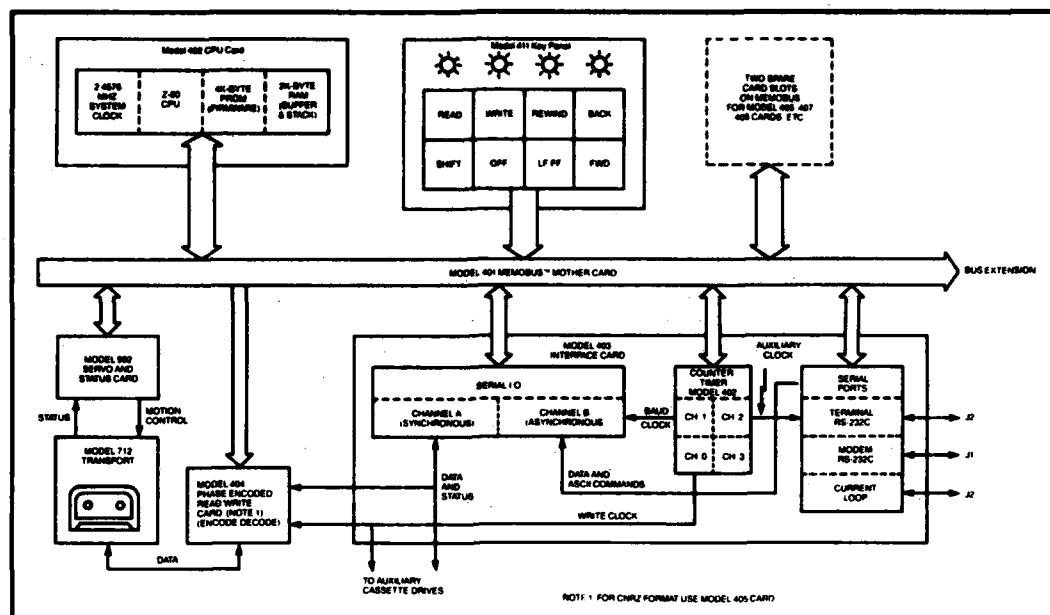
FRONT PANEL KEYPAD CONTROL

Eight keys and four light emitting diode (LED) indicators all serving multiple functions, constitute the front panel control. The Model 411 keypad generates a unique vectored interrupt for each keystroke, interfacing with the M80 firmware, which is augmented to implement control operations. The multi-function key-

pad provides a total of 28 keystrokes, four of which select either RECORDER MODE or COMMAND MODE operation. The remaining 24 keystrokes initiate assorted system functions, depending on the mode of operation. See Table 1.

KEY NAME	RECORDER MODE		COMMAND MODE	
	NO SHIFT	SHIFT	NO SHIFT	SHIFT
BACK	FILE REVERSE OR BLOCK REVERSE	SYSTEM RESET	1	
REWIND	REWIND	CLEAR COMMAND BUFFER	2	REVIEW KEY SEQUENCE
WRITE	TAPE-ON (RECEIVE AND WRITE)	FINISH WRITING OR WRITE FILE GAP	4	
READ	X-ON (READ AND TRANSMIT)	CLEAR DATA BUFFER	8	
OFF	X-OFF, TAPE-OFF, AND HALT HIGH SPEED OPERATION		CLEAR (PREPARE FOR NEW COMMAND CODE)	RECORDER MODE
LF/FF	LOAD FORWARD OR FAST FORWARD	ERASE	EXECUTE	
FWD	FILE FORWARD OR BLOCK FORWARD	COMMAND MODE	ENTER DATA	

KEYSTROKE FUNCTION CHART
TABLE 1

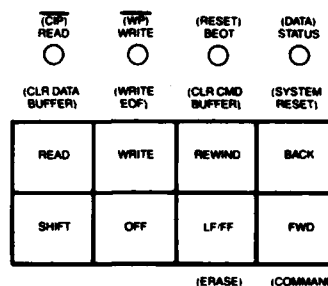


M80 FUNCTIONAL BLOCK DIAGRAM

RECORDER MODE

The M80 powers up in the recorder mode, which gives the user direct control of tape motion and action. The keypad and indicator functions for the recorder control mode are illustrated in the first two columns of Table 1, and in Figure 1. Note that if the SHIFT key is held down, the other keys assume those functions represented in parentheses. (Figure 1)

Tape motion and Read and Write operations are most easily controlled in the RECORDER mode.



(ERASE) (COMMAND MODE)
Names of key functions invoked when the SHIFT key is held and of secondary representations by indicators are shown in parentheses

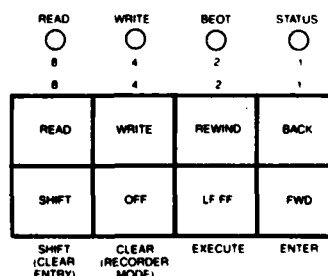
FIGURE 1

RECORDER MODE KEY-PANEL DIAGRAM

COMMAND MODE

A SHIFT-FORWARD keystroke enters the M80 system into the COMMAND MODE, which gives the user control of the computer itself and its related functions. The top row of keys become the hex-coded data or parameter keys 8, 4, 2 and 1, with the LED above each key indicating DATA STATUS; thus the READ, WRITE, REWIND and BACK keys of Fig. 2 enter in 8, 4, 2 and 1, respectively, and the LED above each key lights to indicate the ON state of its assigned bit.

The bottom row of keys assume those functions written under the keypad diagram in Fig. 2. The SHIFT key is used only for two functions in conjunction with other keys; these and all other keyboard functions are illustrated in the last two columns of Table 1.



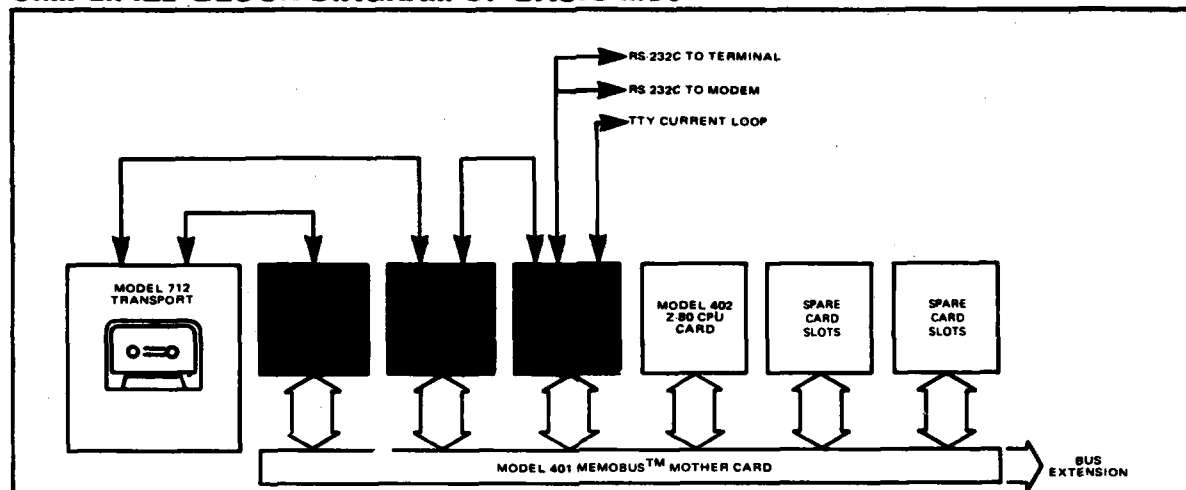
SHIFT (CLEAR ENTRY) CLEAR (RECORDER MODE) EXECUTE ENTER

The legends shown on the keys and just above the indicators in this diagram appear on the actual key-panel but do not correspond to functions in the COMMAND MODE. Names of key functions invoked when the SHIFT key is held are shown in parentheses

FIGURE 2

COMMAND MODE KEY-PANEL DIAGRAM

SIMPLIFIED BLOCK DIAGRAM OF BASIC M80



ORDERING INFORMATION:

When ordering an M80, we ask that you complete a questionnaire which details the firmware-selectable operation parameters; e.g. baud rate, block size, parity, etc. Although these parameters are all selectable via the keypad, it makes sense to have most of your requirements satisfied by custom firmware which Memodyne will prepare from your questionnaire. Separate forms are used for CNRZ and Phase-encoded formats.

Model M80/2000FPC

Cassette Computer System in 2000 Portable Case

Model M80/3000FPC

Cassette Computer System in 3000 Desk Top Case

Add suffix "R" for rack mounting

NOTE 1. For either model add suffix "E" for 220V AC operation (EG: M80/3000FPCRE)

Note 2. Phase encoding or CNRZ should be specified on Questionnaire

CAS-2H

Certified Digital Cassette
Recommended cassette
is 300' long, has BEOT
holes

Bulk Eraser

Model 360

OTHER ACCESSORIES AND OPTIONS

With such a versatile recording system many accessories and/or optional cards, etc. are available. Here is a brief list. If interested please notify our nearest representative or consult with the factory.

Firmware listing - Cassette or paper

Firmware PROM Set

Source Program on Disk

Test tape - Phase Encoded

Test tape - CNRZ

Model 403 Card Modified for Transparent operations

Model 404 Phase Encoded Card

Model 405 CNRZ Card

Model 406 8K Static RAM Card

Model 407 4K to 16K U.V. EPROM Card

Model 408 4 channel, 12 Bit plus sign
A/D Converter Card

Model 351 Rack Mounting ears for 3000 Case

CORPORATION

220 Reservoir Street

Needham Hgts., MA 02194

Tel. (617) 444-7000 Telex 92-2537



M80/FPC 20K812

APPENDIX B

Sample Calculations for N_q Using Simplified Skies

J.I. Gordon

A key part of the calculation to obtain R^* is the calculation of equilibrium radiance. The exact expression for the equilibrium radiance $L_q(z, \theta, \phi)$ is

$$L_q(z, \theta, \phi) = \epsilon_s(z) \frac{\sigma(z, \beta)}{s(z)} + \int_{\Omega} L(z, \theta', \phi') \frac{\sigma(z, \beta')}{s(z)} d\Omega, \quad (1)$$

where the path of sight zenith angle and azimuth are θ and ϕ respectively, z is the altitude, the sun scalar irradiance is $\epsilon_s(z)$, the proportional volume scattering function at altitude z is $\sigma(z, \beta)/s(z)$, and the sky and terrain radiance is $L(z, \theta', \phi')$ at zenith angle θ' and azimuth ϕ' . The angle β is the scattering angle between the path of sight and the sun zenith angle θ_s . Since the sky and path of sight azimuths are relative to the sun, $\phi_s = 0$, and the angle β is found from

$$\cos \beta = \sin \theta \cos \phi \sin \theta_s + \cos \theta \cos \theta_s. \quad (2)$$

The angle between the path of sight and the sky or terrain vector at θ', ϕ' is

$$\cos \beta' = \sin \theta \cos \phi \sin \theta' \cos \phi' + \sin \theta \sin \phi \sin \theta' \sin \phi' + \cos \theta \cos \theta'. \quad (3)$$

This monograph will evaluate various approximations for the equilibrium radiance. Twenty two combinations of the path of sight θ, ϕ were assumed for the evaluation, $\theta = 0, 75, 80, 85, 95, 100, 180$ and $\phi = 0, 90, 180$ & 270 . These were the same combinations used for the HAVENVIEW II report, Duntley *et al.* (1976).

COMPLEX SKY

The sky scanner data are taken with a 5° field of view and data are tabulated for each $\Delta\theta = 5^\circ$ and $\Delta\phi = 6^\circ$. However, Program AVIZC130 which computes $L_q(z, \theta, \phi)$ uses $\Delta\theta = 5^\circ$, but averages the radiances for $\Delta\phi = 12^\circ$ at the horizon and for $\Delta\phi = 180^\circ$ at $\theta = 2.5^\circ$. The true angle in the $\Delta\phi$ dimension is actually equal to $\sin \theta \Delta\phi$. In the integration grid $\sin \theta \Delta\phi$ ranges from 7.9° to 13° . The integration grid specifications are summarized in Table 1 for the upper hemisphere. The lower hemisphere grid is directly analogous.

For evaluating equilibrium radiance in AVIZC130, Eq. (1) is rewritten as

$$L_q(z, \theta, \phi) = \epsilon_s(z) \frac{\sigma(z, \beta)}{s(z)} + \sum_1^{782} L(z, \theta', \phi') \frac{\sigma(z, \beta')}{s(z)} \Delta\Omega. \quad (4)$$

We will assume that evaluation of Eq. (4) using the entire scanner array as input is a reasonable representation of the exact integral in Eq. (1).

Table 1. Sky grid used for integration in program AVIZ-C130.

Zenith Angle θ	$\Delta\phi$	Number of Radiances Averaged	$\sin \theta \Delta\phi$	No. of Points in Integration
2.5	180	30	7.9	2
7.5	90	15	11.7	4
12.5	60	10	13.0	6
17.5	30	5	9.0	12
22.5	30	5	11.5	12
27.5	24	4	11.1	15
32.5	18	3	9.7	20
37.5	18	3	11.0	20
42.5	12	2	8.1	30
47.5	12	2	8.8	30
52.5	12	2	9.5	30
57.5	12	2	10.1	30
62.5	12	2	10.6	30
67.5	12	2	11.1	30
72.5	12	2	11.4	30
77.5	12	2	11.7	30
82.5	12	2	11.9	30
87.5	12	2	12.0	30

$\Sigma = 391$

For the sample calculations we selected a flight which had already been used for computations of path radiance and fully reported in the HAVENVIEW II report. Flight C-289 was a low altitude flight on 14 June 1973. There were clouds but the sun was unobscured. The unobscured space-to-ground vertical beam transmittance was 0.664 for the pseudo-photopic Filter 4. The flight track was in northern Germany over cultivated farmlands interspersed with dark patches of dense woods.

A modification to Program AVIZC130 was made subsequent to the HAVENVIEW II report. This modification changed the method of selection of the proportional volume scattering function $\sigma(z, \beta)/s(z)$. Therefore a new run of AVIZC130 was made for C-289 for Filter 4 only. The resultant equilibrium radiances for the altitude 1192m are summarized in Table 2.

SCALAR IRRADIANCE APPROXIMATION

The simplest approximation the the equilibrium radiance is a function of the scalar sun, sky and upwelling irradiances [Eq. (21), Gordon (1969)],

$$L_q(z, \theta, \phi) = \epsilon_s(z) \frac{\sigma(z, \beta)}{s} + \frac{d\epsilon(z, d) + \epsilon(z, u)}{4\pi}. \quad (5)$$

The $d\epsilon(z, d)$ is the sky scalar irradiance (downwelling, diffuse) and $\epsilon(z, u)$ is the upwelling scalar irradiance.

Equilibrium radiances were hand calculated for flight C-289 Filter 4 altitude 1192m using Eq. (5). The ratios of the equilibrium radiance using the scalar irradiance approximation to the equilibrium radiance from the complex sky Eq. (4), are tabulated in Table 2.

There is no difference in the results from Eq. (5) for $\phi = 90$ and 270° or -90° since the only azimuth dependency is in the sun component (1st term in Eq. (5)). The difference in the equilibrium radiance ratios for $\pm 90^\circ$ is due to the non-symmetrical aspects of the C-289 complex

Table 2. Equilibrium radiance and ratios for C-289 filter 4 altitude 1192m.

Azimuth		Equilibrium Radiance ($w/\Omega m^2 \mu m$) using Complex Sky Grid							
ϕ	$\theta=0$	75	80	85	95	100	180		
0	3.11E2	4.04E2	3.42E2	2.90E2	2.24E2	1.93E2	9.89E1		
90		1.37E2	1.32E2	1.26E2	1.17E2	1.13E2			
90		1.49E2	1.42E2	1.36E2	1.23E2	1.18E2			
180		1.16E2	1.18E2	1.19E2	1.22E2	1.23E2			
		Equilibrium Radiance Ratio Using Scalar Irradiance Equation							
ϕ	$\theta=0$	75	80	85	95	100	180	Total Range	
0	.94	.84	.83	.84	.87	.91	1.37	.83 - 1.37	
90		1.01	1.02	1.05	1.09	1.12			
90		.93	.95	.97	1.04	1.07			
180		1.07	1.07	1.08	1.08	1.10			
		Equilibrium Radiance Ratio Using Constant Sky Grid							
ϕ	$\theta=0$	75	80	85	95	100	180	Total Range	
0	1.03	.87	.86	.85	.85	.87	1.08	.85 - 1.19	
90		1.10	1.08	1.08	1.05	1.04			
90		1.01	1.01	1.00	1.00	1.00			
180		1.19	1.14	1.11	1.05	.93			
		Equilibrium Radiance Ratio Using Banded Sky Grid							
ϕ	$\theta=0$	75	80	85	95	100	180	Total Range	
0	1.00	.88	.87	.87	.88	.89	1.00	.87 - 1.22	
90		1.12	1.11	1.12	1.09	1.08			
90		1.03	1.04	1.04	1.04	1.03			
180		1.22	1.18	1.15	1.08	1.07			
		Equilibrium Radiance Ratio Using Simple Sky Grid							
ϕ	$\theta=0$	75	80	85	95	100	180	Total Range	
0	1.03	.97	.96	.96	.94	.95	.97	.94 - 1.03	
90		.98	.97	.97	.94	.94			
90		1.01	1.01	1.01	.99	.98			
180		1.03	1.00	1.00	.97	.97			

sky and the differences in the complex sky values of equilibrium radiance (top of Table 2).

The scalar irradiances used for evaluating Eq. (5) are listed in Table 4 for convenient reference.

CONSTANT SKY

An input scanner tape was developed in which an average sky radiance was used for the upper hemisphere (UHS) and an average terrain radiance was used for the lower hemisphere (LHS). These values are also tabulated in Table 4. This tape was used as input to AVIZC130. The resultant equilibrium radiances for 1192m altitude were divided by the values for the complex sky. These ratios are tabulated in Table 2, labeled constant sky grid ratios. This grid reduced the ratio for the straight downward case in comparison to the ratio from scalar irradiance equation but increased the ratios for a few cases.

Using a constant sky radiance and a constant terrain radiance in Eq. (4) effectively changes the equation as follows,

$$L_q(z, \theta, \phi) = \epsilon(z) \frac{\sigma(z, \beta)}{s(z)} + d L(z) \sum_1^{391} \Delta \Omega + L_u(z) \sum_1^{391} \frac{\sigma(z, \beta')}{s(z)} \Delta \Omega \quad (6)$$

where β' is defined by Eq. (3). In scalar irradiance terms

$$L_q(z, \theta, \phi) = \epsilon(z) \frac{\sigma(z, \beta)}{s(z)} + \frac{d \epsilon(z, d)}{2\pi} \sum_1^{391} \frac{\sigma(z, \beta')}{s(z)} \Delta \Omega + \frac{\epsilon(z, u)}{2\pi} \sum_1^{391} \frac{\sigma(z, \beta')}{s(z)} \Delta \Omega \quad (7)$$

Since

$$\int_{4\pi} \frac{\sigma(z, \beta')}{s(z)} d\Omega = 1,$$

the sum of the two

$$\sum_1^{391} \frac{\sigma(z, \beta')}{s(z)} \Delta \Omega$$

terms also equals 1. However, except for path of sight $\theta=90^\circ$, the weighting factor for $d \epsilon(z, d)$ does not equal the weighting factor for $\epsilon(z, u)$, i.e.:

$$\sum_1^{391} \frac{\sigma(z, \beta')}{s(z)} \Delta \Omega \neq .5$$

APPENDIX B

Table 3. Flight C-289 filter 4 radiances at 1192m for the sample grid.

θ	ϕ	Radiance ($w/\Omega m^2 \mu m$)		
		Average	Center	Center/Average
30	0	2.95E2	3.75E2	1.27
	90	1.01E2	4.01E1	.40
	- 90	9.66E1	3.74E1	.39
	180	5.39E1	2.39E1	.44
75	0	2.02E2	1.87E2	.93
	90	9.63E1	1.19E2	1.24
	- 90	1.38E2	1.06E2	.77
	180	9.59E1	8.36E1	.87
105	0	5.93E1	3.94E1	.66
	90	4.37E1	2.72E1	.62
	- 90	5.00E1	3.54E1	.71
	180	5.48E1	5.46E1	1.00
150	0	2.23E1	2.25E1	1.01
	90	2.95E1	3.49E1	1.18
	- 90	2.52E1	3.18E1	1.26
	180	3.04E1	5.39E1	1.77

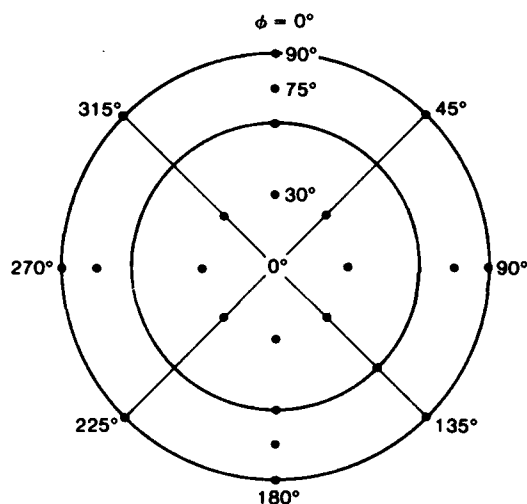


Fig. B-1. This simple sky grid has 8 elements for the sky and 8 for the terrain with 4 zenith angle cuts and 4 azimuth cuts, just about the simplest one could devise. Computed average radiances for each element of this grid for the 1192m altitude sky and terrain from C-289 filter 4 are given in Table 4.

except for $\theta=90^\circ$. Equation (5) assumes the weighting factors for the $\epsilon(z,u)$ and $\epsilon(z,d)$ to be equal no matter what the path of sight is.

BANDED SKY

A second special input scanner tape was developed using average radiances for each $\Delta\theta=15^\circ$ and $\Delta\phi=360^\circ$. These radiances again, are tabulated in Table 4. This tape was also run through Program AVIZC130. The resultant equilibrium radiances were again divided by the values for the complex sky and these ratios tabulated in Table 2 herein. The straight upward and downward cases are excellent but the lack of azimuthal variation in the sky grid affects the values near the horizon.

Table 4. Irradiance and radiance specifications for various approximations for C-289 filter 4.

Label			Scalar Irradiance $w/m^2 \mu m$	
			$z=258$	$z=1192$
Scalar Irradiance	Sun	$\epsilon_s(z)$	1.11E3	1.21E3
	Sky	$\epsilon_s(z,d)$	7.26E2	8.77E2
	Upwelling	$\epsilon(z,u)$	1.95E2	2.52E2
Constant Sky	Zenith Angle	θ	Average Radiance $w/\Omega m^2 \mu m$	
			$z=258$	$z=1192$
			0	1.16E2
		180	3.10E1	4.01E1
Banded Sky	Zenith Angle	θ	Average Radiance $w/\Omega m^2 \mu m$	
			$z=258$	$z=1192$
			7.5	5.19E1
			22.5	5.38E1
			37.5	1.38E2
			52.5	1.04E2
			67.5	1.20E2
			82.5	1.36E2
			97.5	4.16E1
			112.5	2.46E1
			127.5	3.06E1
			142.5	2.67E1
			157.5	2.91E1
			172.5	2.64E1
Simple Grid	Zenith Angle	Azimuth	Average Radiance $w/\Omega m^2 \mu m$	
			$z=1192$	
			θ	ϕ
			30	0
				90
				180
				270
			75	0
				90
				180
				270
			105	0
				90
				180
				270
			150	0
				90
				180
				270

SIMPLE GRID

Wishing to test the effect of a very simple grid which gave a few cuts in azimuth as well as in zenith angle for the 4π sphere. I kept the $d\Omega$ constant for the grid so $\Delta\Omega = 4\pi/16 = \pi/4$ and $\theta = 30, 75, 105$, and 150° , $\phi = 0, 90, 180, 270$. The grid is illustrated in Fig. B-1. I averaged the sky and terrain radiances for 1192m altitude for each portion of the grid and these values are tabulated in Table 4. (Note that this grid is simpler than the grid illustrated in Fig. 4-2 and was chosen for computational simplicity.)

The equation for computing equilibrium radiance using this simple grid is

$$L_q(z, \theta, \phi) = \epsilon(z) \frac{\sigma(z, \beta)}{s(z)} + \sum_{i=1}^{16} L(z, \theta', \phi') \frac{\sigma(z, \beta')}{s(z)} \Delta \Omega \frac{1}{\sum_{i=1}^{16} \frac{\sigma(z, \beta')}{s(z)} \Delta \Omega} \quad (8)$$

The portion of the second term

$$\frac{1}{\sum_{i=1}^{16} \frac{\sigma(z, \beta')}{s(z)} \Delta \Omega}$$

is a corrective factor. The correct weighting factor is

$$\int_{2\pi} \frac{\sigma(z, \beta')}{s(z)} d\Omega = 1$$

whereas for the simple grid

$$\sum_{i=1}^{16} \frac{\sigma(z, \beta')}{s(z)} \Delta \Omega \neq 1,$$

in fact these values varied between 1.16 to 1.19, a considerable error if not compensated for.

I calculated the equilibrium radiances using a hand calculator and then divided by the values for the complex

sky. The resultant ratios are tabulated in Table 2. The ratios are surprisingly good. In 16 of the 22 cases the ratios indicate L_q values $\pm 3\%$ of the complex values, essentially within our accuracy limit. The remaining 6 are $\pm 6\%$, which is still quite acceptable.

It should be emphasized that in all the approximations, the total input flux was held essentially constant by using average radiances for each integration element. This happens to be particularly important for C-289 which was a partly cloudy sky, completely unsymmetrical, etc. To illustrate this importance I have tabulated for the simple grid the average radiance and the radiance at the central θ, ϕ in Table 3, along with the ratio of the center to the average radiance. I have deliberately put ± 90 together in the table to emphasize the non-symmetrical aspect of the radiances. For the 30° and 150° radiances 180 points were averaged for each element in the grid. For the 75° and 105° elements, 90 radiances were averaged.

SUMMARY

The equilibrium radiance calculation can be made quickly with the scalar irradiance equation Eq. (5) but with limited accuracy. Most of the examples were $\pm 10\%$ (16 out of 22) but the nadir look error was 37%.

The integration with the simple grid of 16 equal points, Eq. (6) works surprisingly well, all within $\pm 6\%$. It is fairly fast calculation even by hand because there are so few points.

APPENDIX C

GLOSSARY AND NOTATION

The notation used in reports and journal articles produced by the Visibility Laboratory staff follows, in general, the rules set forth in pages 499 and 500, Duntley *et al.* (1957). These rules are:

Each optical property is indicated by a basic (parent) symbol.

A presubscript may be used with the parent symbol as an identifier, *e.g.*, *b* indicates background while *t* denotes an object, *i.e.* target.

A postsubscript may be used to indicate the length of a path of sight, *e.g.*, *r* denotes an apparent property as measured at the end of a path of sight of length *r*, while *o* denotes an inherent property based on the hypothetical concept of a photometer located at zero distance from an object, *i.e.* target.

A postsuperscript* or postsubscript*, is employed as a mnemonic symbol signifying that the radiometric quantity has been generated by the scattering of ambient light reaching the path from all directions.

The parenthetical attachments to the parent symbol denote altitude and direction. The letter *z* indicates altitude in general; *z_t* is used to specify the altitude of a target. The direction of a path of sight is specified by the zenith angle θ and the azimuth ϕ . In the case of irradiances, the downwelling irradiance is designated by *d*, the upwelling by *u*.

The radiometric symbols used herein now correspond to the OSA recommendations in Section 1 of the Handbook of Optics, McGraw-Hill Book Co., Driscoll and Vaughn (1978). Prior to June 1980, the symbol used for radiance *L* was *N*, for irradiance *E* was *H*, and for attenuation length was *L*.

Symbol	Units	Quantity
$A(z)$	none	Albedo at altitude <i>z</i> , defined $A(z) = E(z,u)/E(z,d)$
$a(z)$	m^{-1}	Absorption coefficient
$C_o(z, \theta, \phi)$	none	Inherent contrast determined for a path of sight of zero length at the altitude of the object <i>z_t</i> in the direction of zenith angle θ and azimuth ϕ .
$C_r(z, \theta, \phi)$	none	Apparent contrast as determined at altitude <i>z</i> from the end of path of sight of length <i>r</i> in the direction of zenith angle θ and azimuth ϕ .
$D(z)$	none	Radiance distribution function $D(z) = \int_{\pi} L(z, \theta', \phi') \sec \theta' d\Omega' / \pi(z)$
$D(\lambda)$	none	Limb darkening factor relating the average sun radiance and the center sun radiance $D(\lambda) = \int_s \bar{L}_o / \int_s L_o$
E_λ	W/m^2	Spectral irradiance (formerly symbol <i>H</i>) defined as $E_\lambda = \int_{\pi} L_\lambda(z, \theta, \phi) \cos \theta d\Omega$

Symbol	Units	Quantity
E	$W/m^2 \mu m$	broad band sensor irradiance, defined as $E = \int_0^\infty E_\lambda \bar{S}_\lambda \bar{T}_\lambda d\lambda / \int_0^\infty \bar{S}_\lambda \bar{T}_\lambda d\lambda$
$E(z, d)$	W/m^2	Irradiance produced by downwelling flux as determined on a horizontal flat plate at altitude <i>z</i> (formerly <i>H(z, d)</i>). In this report <i>d</i> is used in place of the minus sign in the notation (<i>H(z, -)</i>) which appears in Duntley (1969). This property may be defined by the equation $E(z, d) = \int_{2\pi} L(z, \theta', \phi') \cos \theta' d\Omega'$
$E(z, u)$	W/m^2	Irradiance produced by the upwelling flux as determined on a horizontal flat plane at altitude <i>z</i> (formerly <i>H(z, u)</i>). Here <i>u</i> is substituted for the plus sign formerly used in the notation (<i>H(z, +)</i>).
$g(z)$	none	Asymmetry factor $g(z) = \frac{1}{2} \int_{-1}^1 P(z, \beta) \cos \beta d(\cos \beta)$
$H(z)$	<i>m</i>	Scale height at altitude <i>z</i> , the height of a homogeneous atmosphere having the density of the layer at altitude <i>z</i> .
L_λ	$W/sr m^2$	Spectral radiance (former symbol <i>N</i>)
L	$W/sr m^2 \mu m$	Broad band sensor radiance is defined as $L = \int_0^\infty L_\lambda \bar{S}_\lambda \bar{T}_\lambda d\lambda / \int_0^\infty \bar{S}_\lambda \bar{T}_\lambda d\lambda$
$L_o(z, \theta, \phi)$	$W/sr m^2$	Inherent radiance based on the hypothetical concept of a photometer located at zero distance from an object at altitude <i>z</i> in the direction specified by zenith angle θ and azimuth ϕ .
$L_r(z, \theta, \phi)$	$W/sr m^2$	Apparent radiance as determined at altitude <i>z</i> , from the end of a path of sight of length <i>r</i> at zenith angle θ and azimuth ϕ . This property may be defined by $L_r(z, \theta, \phi) = L_o(z, \theta, \phi) T_r(z, \theta) + L_r^*(z, \theta, \phi)$
$L(\lambda, T)$	$W/sr m^2$	Black body radiance at wavelength λ and temperature <i>T</i>
$L_q(z, \theta, \phi)$	$W/sr m^2$	Equilibrium radiance at altitude <i>z</i> with the direction of the path of sight specified by zenith angle θ and azimuth ϕ . This property is a point function of position and direction.
$L_s(z, \theta, \phi)$	$W/sr m^2$	Path function at altitude <i>z</i> with the direction of the path of sight specified by zenith angle θ and azimuth ϕ . This property is defined by the equation $L_s(z, \theta, \phi) = \int_{\pi} \sigma(z, \beta') L(z, \theta', \phi') d\Omega'$
$L_r^*(z, \theta, \phi)$	$W/sr m^2$	Path radiance as determined at altitude <i>z</i> at the end of a path of sight of length <i>r</i> in the direction of zenith angle θ and azimuth ϕ .
$L_\infty^*(z, \theta, \phi)$	$W/sr m^2$	Sky radiance at altitude <i>z</i> , zenith angle θ and azimuth ϕ . Also the path radiance for the path of sight of length ∞ from out of the atmosphere to altitude <i>z</i> .

APPENDIX C

Symbol	Units	Quantity	Symbol	Units	Quantity
$s L_{\infty}(z, \theta_s, \phi)$	$W/sr m^2$	Apparent radiance of the center of the solar disk as determined from the end of a path of sight of length ∞ from out of the atmosphere to altitude z at the zenith angle of the sun θ_s .	β	deg	Symbol for scattering angle of flux from a light source. It is equal to the angle between the line from the source to any unit scattering volume and the path of a ray scattered off this direct line.
$m_{\infty}(z, \theta)$	kg/m^2	Absolute air mass at angle θ $m_{\infty}(z, \theta) = \int_z^{\infty} \rho(z) dz$.	Δ	none	Symbol to indicate incremental quantity and used with r and z to indicate small, discrete increments in path length r and altitude z .
$m_{\infty}(z, \theta)/m_{\infty}(z, 0)$	none	Relative optical air mass	$\epsilon(z)$	W/m^2	Scalar irradiance. This may be defined as the radiant flux arriving at a point, from all directions about that point, at altitude z (Tyler and Preisendorfer (1962)). $\epsilon(z) = \int_{4\pi} L(z, \theta', \phi') d\Omega'$.
$m(\theta_s)$	none	Relative optical airmass at zenith angle of the sun, shorthand for $m_{\infty}(z, \theta_s)/m_{\infty}(z, 0)$.	$\rho^e(z)$	W/m^2	Diffuse scalar irradiance $\rho^e(z) = \epsilon(z) - s \epsilon(z)$.
$n(z)$	none	Refractive index	$s \epsilon(z)$	W/m^2	Sun scalar irradiance at altitude z $s \epsilon(z) = s \epsilon(\infty) T_{\infty}(z, \theta_s)$.
$P(z, \beta)$	sr^{-1}	Normalized phase function for single scattering. $P(z, \beta) = r(z, \beta)/s(z)$	ζ	m	Radius of the earth.
$Q(z)$	none	Optical scattering mixing ratio at altitude z . This quantity is defined as the ratio of the total volume scattering coefficient at altitude z , to the molecular (or Rayleigh) volume scattering coefficient at the same altitude z . $Q(z) = s(z)/R s(z)$	θ	deg	Symbol for zenith angle. This symbol is usually used as one of two coordinates to specify the direction of a path of sight.
r	m	Path length, for paths of sight at zenith angles 0 to 70 degrees. $r = sec \theta \Delta z$	θ'	deg	Symbol for zenith angle usually used as one of two coordinates to specify the direction of a discrete portion of the sky.
$s(z)$	m^{-1}	Total volume scattering coefficient as determined at altitude z . This property may be defined by the equations $s(z) = \int_{4\pi} r(z, \beta) d\Omega = R s(z) + M s(z)$ In the absence of atmospheric absorption, the total volume scattering coefficient is numerically equal to the attenuation coefficient.	θ_s	deg	Zenith angle of the sun.
$M^s(z)$	m^{-1}	Volume scattering coefficient for Mie i.e. aerosol, scattering at altitude z .	λ	nm	Symbol for wavelength.
$R^s(z)$	m^{-1}	Volume scattering coefficient for Rayleigh i.e. molecular scattering at altitude z .	$\rho(z)$	kg/m^3	Density at altitude z .
$T(z)$	$^{\circ}K$	Absolute temperature at altitude z .	$r(z, \beta)$	$m^{-1} sr^{-1}$	Symbol for volume scattering function. Parenthetical symbols are z to designate altitude and β to designate the scattering angle from a source.
$T_r(z, \theta)$	none	Radiance transmittance as determined at altitude z for a path of sight of length r at zenith angle θ (formerly referred to as "beam" transmittance). This property is independent of azimuth in atmospheres having horizontal uniformity. It is always the same for the designated path of sight or its reciprocal.	$\tau(z)$	none	Optical depth $\tau(z) = \int_z^{\infty} \alpha(z) dz$
$c T_r(z, \theta, \phi)$		Contrast transmittance $c T_r(z, \theta, \phi) = C_o(z, \theta, \phi)/C_r(z, \theta, \phi)$	ϕ	deg	Symbol for azimuth. The azimuth is the angle in the horizontal plane of the observer between a fixed point and the path of sight. The fixed point may be for example, true North, the bearing of the sun, or the bearing of the moon. This symbol is usually used as one of two coordinates to specify the direction of a path of sight.
$T_{\infty}(z, \theta)$	none	Radiance transmittance for the path of sight at zenith angle θ from out of the atmosphere to the altitude z .	ϕ'	deg	This symbol for azimuth is usually used as one of two coordinates to specify the direction of a discrete portion of the sky.
$\omega(z)$	none	Single scattering albedo $\omega(z) = s(z)/\alpha(z)$	ψ	deg	Angular solar radius at true earth-to-sun distance.
z	m	Altitude, usually used as above ground level.	$\bar{\psi}$	deg	Angular solar radius at mean solar distance.
z_t	m	Altitude of any applicable target.	Ω	sr	Symbol for solid angle. For a hemisphere: $\Omega = 2\pi$ steradians; For a sphere: $\Omega = 4\pi$ steradians.
$\alpha(z)$	m^{-1}	Volume attenuation coefficient as determined at altitude z . $\alpha(z) = a(z) + s(z)$.			

APPENDIX D

VISIBILITY LABORATORY CONTRACTS AND RELATED PUBLICATIONS

Previous Related Contracts:

F19628-73-C-0013, F19628-76-C-0004

PUBLICATIONS:

- Duntley, S.Q., R.W. Johnson, J.I. Gordon, and A.R. Boileau (1970), "Airborne Measurements of Optical Atmospheric Properties at Night", University of California at San Diego, Scripps Institution of Oceanography, Visibility Laboratory, SIO Ref. 70-7, AFCRL-70-0137, NTIS No. AD 870 734.
- Duntley, S.Q., R.W. Johnson, and J.I. Gordon (1972a), "Airborne Measurements of Optical Atmospheric Properties in Southern Germany", University of California at San Diego, Scripps Institution of Oceanography, Visibility Laboratory, SIO Ref. 72-64, AFCRL-72-0255, NTIS No. AD 747 490.
- Duntley, S.Q., R.W. Johnson, and J.I. Gordon (1972b), "Airborne and Ground-Based Measurements of Optical Atmospheric Properties in Central New Mexico", University of California at San Diego, Scripps Institution of Oceanography, Visibility Laboratory, SIO Ref. 72-71, AFCRL-72-0461, NTIS No. AD 751 936.
- Duntley, S.Q., R.W. Johnson, and J.I. Gordon (1972c), "Airborne Measurements of Optical Atmospheric Properties, Summary and Review", University of California at San Diego, Scripps Institution of Oceanography, Visibility Laboratory, SIO Ref. 72-82, AFCRL-72-0593, NTIS No. AD 754 898.
- Duntley, S.Q., R.W. Johnson, and J.I. Gordon (1973), "Airborne Measurements of Optical Atmospheric Properties in Southern Illinois", University of California at San Diego, Scripps Institution of Oceanography, Visibility Laboratory, SIO Ref. 73-24, AFCRL-TR-73-0422, NTIS No. AD 774 597.
- Duntley, S.Q., R.W. Johnson, and J.I. Gordon (1974), "Airborne and Ground-Based Measurements of Optical Atmospheric Properties in Southern Illinois", University of California at San Diego, Scripps Institution of Oceanography, Visibility Laboratory, SIO Ref. 74-25, AFCRL-TR-74-0298, NTIS No. ADA 013 164.
- Duntley, S.Q., R.W. Johnson, and J.I. Gordon (1975), "Airborne Measurements of Optical Atmospheric Properties in Western Washington", University of California at San Diego, Scripps Institution of Oceanography, Visibility Laboratory, SIO Ref. 75-24, AFCRL-TR-75-0414, NTIS No. ADA 026 036.
- Duntley, S.Q., R.W. Johnson, and J.I. Gordon (1975), "Airborne Measurements of Optical Atmospheric Properties, Summary and Review II", University of California at San Diego, Scripps Institution of Oceanography, Visibility Laboratory, SIO Ref. 75-26, AFCRL-TR-75-0457, NTIS No. ADA 022 675.
- Duntley, S.Q., R.W. Johnson, and J.I. Gordon (1976), "Airborne Measurements of Optical Atmospheric Properties in Northern Germany", University of California at San Diego, Scripps Institution of Oceanography, Visibility Laboratory, SIO Ref. 76-17, AFGL-TR-76-0188, NTIS No. ADA 035 571.
- Duntley, S.Q., R.W. Johnson, and J.I. Gordon (1977), "Airborne Measurements of Atmospheric Volume Scattering Coefficients in Northern Europe, Spring 1976", University of California at San Diego, Scripps Institution of Oceanography, Visibility Laboratory, SIO Ref. 77-8, AFGL-TR-77-0078, NTIS No. ADA 046 290.
- Duntley, S.Q., R.W. Johnson, and J.I. Gordon (1978a), "Airborne Measurements of Atmospheric Volume Scattering Coefficients in Northern Europe, Fall 1976", University of California at San Diego, Scripps Institution of Oceanography, Visibility Laboratory, SIO Ref. 78-3, AFGL-TR-77-0239, NTIS No. ADA 057 144.
- Duntley, S.Q., R.W. Johnson, and J.I. Gordon (1978b), "Airborne Measurements of Atmospheric Volume Scattering Coefficients in Northern Europe, Summer 1977", University of California at San Diego, Scripps Institution of Oceanography, Visibility Laboratory, SIO Ref. 78-28, AFGL-TR-78-0168, NTIS No. ADA 068 611.
- Duntley, S.Q., R.W. Johnson, and J.I. Gordon (1978c), "Airborne Measurements of Optical Atmospheric Properties, Summary and Review III", University of California at San Diego, Scripps Institution of Oceanography, Visibility Laboratory, SIO Ref. 79-5, AFGL-TR-78-0286, NTIS No. ADA 073 121.
- Fitch, B.W., T.S. Cress (1981), "Measurements of Aerosol Size Distribution in the Lower Troposphere over Northern Europe", *J. Appl. Met.*, 20, no. 10, 1119-1128, also issued as University of California at San Diego, Scripps Institution of Oceanography, Visibility Laboratory, SIO Ref. 81-18, AFGL-TR-80-0192, NTIS No. ADA 104 272.
- Gordon, J.I., J.L. Harris, Sr., and S.Q. Duntley (1973), "Measuring Earth-to-Space Contrast Transmittance from Ground Stations", *Appl. Opt.*, 12, 1317-1324.
- Gordon, J.I., C.F. Edgerton, and S.Q. Duntley (1975), "Signal-Light Nomogram", *J. Opt. Soc. Am.* 65, 111-118.
- Gordon, J.I. (1969), "Model for a Clear Atmosphere", *J. Opt. Soc. Am.* 59, 14-18.
- Gordon, J.I., (1979), "Daytime Visibility, A Conceptual Review", University of California at San Diego, Scripps Institution of Oceanography, Visibility Laboratory, SIO Ref. 80-1, AFGL-TR-79-0257, NTIS No. ADA 085 451.
- Hering, W.S. (1981a), "An Operational Technique for Estimating Visible Spectrum Contrast Transmittance", University of California at San Diego, Scripps Institution of Oceanography, Visibility Laboratory, SIO Ref. 82-1 AFGL-TR-81-0198.

- Hering, W.S. (1981b), "Assessment of Operational Techniques for Estimating Visible Spectrum Contrast Transmittance", *Proc. of the 25th Annual SPIE Symposium on Atmospheric Effects on System Performance*, vol. 205, pp. 119-125.
- Johnson, R.W., and J.I. Gordon (1979), "Airborne Measurements of Atmospheric Volume Scattering Coefficients in Northern Europe, Winter 1978", University of California at San Diego, Scripps Institution of Oceanography, Visibility Laboratory, SIO Ref. 79-25, AFGL-TR-79-0159, NTIS No. ADA 082 044.
- Johnson, R.W., W.S. Hering, J.I. Gordon, B.W. Fitch, and J.S. Shields (1979), "Preliminary Analysis & Modeling Based Upon Project OPAQUE Profile and Surface Data", University of California at San Diego, Scripps Institution of Oceanography, Visibility Laboratory, SIO Ref. 80-5, AFGL-TR-79-0285, NTIS No. ADB 085 451L.
- Johnson, R.W. (1979), "Airborne Measurements of European Atmospheric Scattering Coefficients", *Proc. of SPIE Symp. on Atmospheric Effects on Radiative Transfer*, vol. 195, pp. 31-38.
- Johnson, R.W. and J.I. Gordon (1980), "Airborne Measurements of Atmospheric Volume Scattering Coefficients in Northern Europe, Summer 1978", University of California at San Diego, Scripps Institution of Oceanography, Visibility Laboratory, SIO Ref. 80-20, AFGL-TR-80-0207, NTIS No. ADA 097 134.
- Johnson, R.W. and W.S. Hering (1981a), "Measurements of Optical Atmospheric Quantities in Europe and Their Application to Modelling Visible Spectrum Contrast Transmittance", *Proc. of the AGARD 29th Symposium of the Electromagnetic Wave Propagation Panel on Special Topics in Optical Propagation*, vol. AGARD-CP-300, pp. 14-1 to 14-12.
- Johnson, R.W. and W.S. Hering (1981b), "An Analysis of Natural Variations in Measured European Sky and Terrain Radiances", University of California, San Diego, Scripps Institution of Oceanography, Visibility Laboratory, SIO Ref. 82-6, AFGL-TR-81-0317.
- Johnson, R.W. (1981a), "Winter and Summer Measurements of European Very Low Altitude Volume Scattering Coefficients", University of California, San Diego, Scripps Institution of Oceanography, SIO Ref. 81-26, AFGL-TR-81-0154, NTIS NO. ADA 106 363.
- Johnson, R.W. (1981b), "Spring and Fall Measurements of European Very Low Altitude Volume Scattering Coefficients", University of California at San Diego, Scripps Institution of Oceanography, Visibility Laboratory, SIO Ref. 81-33, AFGL-TR-81-0237, NTIS No. ADA 108 879.
- Johnson, R.W. (1981c), "Daytime Visibility and Nephelometer Measurements Related to its Determination", *Atmospheric Environment*, 15, no. 10/11, 1835-1845.
- Johnson, R.W. (1981d), "Airborne Measurements of European Sky and Terrain Radiances", University of California, San Diego, Scripps Institution of Oceanography, Visibility Laboratory, SIO Ref. 82-2, AFGL-TR-81-0275.
- Johnson, R.W., and B.W. Fitch (1981), "A Review of Measured Atmospheric Optical Properties and Their Contemporary Aerosol Size Distributions", University of California at San Diego, Scripps Institution of Oceanography, Visibility Laboratory, SIO Ref. 82-22, AFGL-TR-82-0049.
- Shields, J.S. (1981), "An Analysis of Infrared and Visible Atmospheric Extinction Coefficient Measurements in Europe", University of California, San Diego, Scripps Institution of Oceanography, Visibility Laboratory, SIO Ref. 82-4, AFGL-TR-81-0251.